Development of hyperspectral coherent Raman scattering microscopy system using high-speed tunable picosecond laser and its application for intracellular lipid imaging

HARSONO CAHYADI

SEPTEMBER 2013

Development of hyperspectral coherent Raman scattering microscopy system using high-speed tunable picosecond laser and its application for intracellular lipid imaging

A dissertation submitted to
THE GRADUATE SCHOOL OF ENGINEERING SCIENCE
OSAKA UNIVERSITY
in partial fulfillment of the requirements for the degree of
DOCTOR OF PHILOSOPHY IN ENGINEERING

BY

HARSONO CAHYADI

SEPTEMBER 2013

Abstract

A hyperspectral coherent anti-Stokes Raman scattering (CARS) and stimulated Raman scattering (SRS) microscopy systems were developed to visualize biomolecular dynamics without any staining. In order to realize the system, a new laser system was developed as a high-speed tunable laser. The synchronization system that utilized two types of timing jitter detection systems was employed. By applying the laser system to multi-focus CARS microscopy system, a new fast spectral CARS microscopy system was established. An acquisition rate of 10 ms/image, faster than video rate (~33 ms/image) was demonstrated. The recovery of synchronization during the wavelength scanning was maintained within 20 ms/wavelength change. The system allowed the fast switching imaging between two Raman shifts that were significantly separated. The spectral imaging capability of spectral CARS microscopy was represented by a series of CARS images due to the scanning of high-speed tunable laser from 875.0 to 905.0 nm which corresponded to the Raman shift of 2663.21 cm^{-1} to 3049.41 cm^{-1}. For a 100 ms exposure time, the imaging process requires 120 ms/image to cover the wavelength change, laser resynchronization after the wavelength change, and image acquisition. Using the spectral SRS microscopy, the demonstration of wide region provided by the AOTF laser was performed from 2100 cm^{-1} to 3200 cm^{-1}. Both spectral CRS microscopy systems were applied to observe deuterated and non-deuterated lipids alternately by switching the wavelength of AOTF laser to 833 nm and 888 nm. Observation of untreated and treated adipocytes with deuterated lipid using spectral CARS microscopy revealed that naturally the deuterated structure did not appear intracellularly so that the signal at 2100 cm^{-1} indicated that the uptaken of the exogenous lipid which had deuterated structure. Further

study revealed that medim- and long-chain fatty acid might follow different metabolic pathways. In fibroblasts observation, the accumulation of lipid likely described the abnormality in lipid storage due to certain diseases. In this case, the fibroblasts were obtained from a patient with indication of triglyceride deposit cardiomyovasculopathy (TGCV). TGCV is a new phenotype of heart disease which is indicated by a massive accumulation of triglyceride (TG) in the coronary arterial wall and cardiomyocytes, though its concentration in blood plasma is found at normal level. As it was observed in the observation of adipocytes, there was a dissimilarity of metabolic pathways of different lipids. This result might suggest the possibility of drug development for TGCV and other lipid-related diseases.

Contents

Introduction

Detection and observation of biomolecules properties and dynamics become important concern in biomedical studies. In practice, every single parts of organism, which may range from subcellular to functional organic level or even the whole-body of organism, can be easily understood as complex composition and interaction of biomolecules [1, 2]. This complexity contributes to both structural and functional purposes which finally determines the type of the cell, tissue, organ, system, and yet the organism. As the smallest functional structure of organism, a cell provides essential properties of organism, including the basic biomolecule metabolism and dynamics [1, 2]. One may enhance his/her understanding to consider a cell as the container with specific environmental setup for biomolecules reactions, so that it is possible to study the real biomolecules reactions [3]. Observation of intracellular metabolism can be used as an approach to provide a model of biological system and function. Therefore, cellular study is an important issue in biomedical researches and developments.

The typical sizes of eukaryotic cells range from 10 – 100 μm so that it is required a microscopic technique to observe the cells. Various microscopic techniques have been developed and improved to satisfy this need. Bright field optical microscopy (such as differential interference contrast (DIC) and phase contrast) [4, 5], electron microscopy [6], and atomic force microscopy [7] gave significant contributions for studying cellular functions and structures. However, it is also necessary to provide the properties of biomolecule which determine the unique function of cell as mentioned earlier. Fluorescence microscopy has been well-known as a powerful tool for observation and analysis in biomedical studies for decades. It has been revealed significant results by introducing suitable staining agents that definitely

attach to specific molecule or chemical compound. Unfortunately, the introduction of fluorophores usually perturbed the cell function/structure and the fluorophore usually suffers from photobleacing [8].

Raman spectroscopy offers a solution for label-free observation of biomolecule due to it molecular vibrations which highly depend on its structure. Raman spectroscopy allows a non-destructive and non-invasive method for biological applications with high chemical selectivity [9, 10]. Unfortunately, conventional Raman spectroscopy cannot satisfy the need of real-time imaging in biological events, because of its low signal efficiency due to the extremely small cross section.

Coherent Raman scattering (CRS), which includes coherent anti-Stokes Raman scattering (CARS) and stimulated Raman scattering (SRS), refers to the nonlinear Raman process. CRS microscopy supersedes spontaneous Raman microscopy which lacks of fast imaging capability. Therefore, CRS microscopy is a powerful tool for label-free biological imaging with high selectivity since it directly senses the molecular vibrations. Furthermore, the fast imaging capability is advantageous for the intracellular observation of biomolecular dynamics. CRS microscopy usually employs two laser sources with slightly different frequencies to excite a specific molecular vibration. Hence, laser sources with high peak power and narrow spectral bandwidth are required to enable the occurrence of nonlinear Raman process and to distinguish the molecular vibration.

CRS microscopy is suitable for lipids observation because lipid has unique features in Raman spectra. Lipid mainly consists of CH bond of which vibrational frequency inhabits specific region in Raman spectrum with significantly strong signal level. The observation of intracellular lipid dynamics can probably tell us more information about lipid functions and metabolism. Particularly, lipid can also be used as an indicator of certain diseases. In this case,

study of intracellular lipid dynamics may support the development of treatments for the diseases.

The purpose of present study is to develop new microscopy systems based on nonlinear Raman for the application of biomolecular study such as intracellular lipid dynamics. A new laser system was constructed to provide sufficient laser source for development of spectral CRS microscopy system. The capability of the developed system was demonstrated for the observation of lipid droplets in adipocytes (fat storing cells). Spectral imaging and fast switching capabilities are also shown.

Outline of this dissertation is as follows:

In the chapter 1, the review on CRS microscopy is presented. The review covers the principles of CRS process which particularly focuses on CARS and SRS, the general setup of and the laser requirement for CRS microscopy, and also some applications of CRS microscopy.

In the chapter 2, the construction of a high-speed tunable picosecond mode-locked laser is elaborated. A tunable laser source is required for realization of spectral CRS microscopy system. Therefore, a narrow spectral bandwidth and a high peak power are the main features needed. Additionally, the stable power during the tuning should also be considered. The development of pulse synchronization system is also essential for minimizing the timing jitter between the two excitation pulses. The pulse synchronization system employs two types of timing jitter detection: an electric phase detector and a balance cross-correlator. The high-speed tunable picosecond laser is based on a picosecond Ti:sapphire mode-locked laser which is equipped with an acousto optic tunable filter (AOTF) for the rapid wavelength tuning. A piezoelectric actuator driving the end mirror and galvano motors driving a pair of parallel plates were introduced into the laser cavity to compensate for the repetition frequency change during the wavelength scanning of AOTF laser. For stabler synchronization, an autogain

amplifier is placed after each of photodetector in the electronic phase detector system, while a polarizing beam splitter and half wave plates were inserted into optical path of balanced cross-correlator.

In chapter 3, the development of fast spectral CARS microscopy using the high-speed tunable picosecond laser is described. To realize the fast spectral CARS microscopy system, the developed AOTF laser system is integrated into multi-focus CARS microscopy. A new control system and the principle of microlens array scanner are briefly explained. This system demonstrates the capability of rapid imaging at rates of 10 ms/image, faster than video rates (~33 nm/image). The AOTF laser is tuned from 875 nm to 905 nm for spectral CARS imaging from 2663.21 to 3049.41 cm^{-1}. For observation of deuterated and non-deuterated lipids, the AOTF laser is switch to 833 and 888 nm to generate CARS signal at 2100 and 2850 cm^{-1}, respectively.

In chapter 4, the development of spectral SRS microscopy is described. The optical setup of spectral CARS microscopy and spectral SRS microscopy share a very similar arrangement. The principle of electro optic modulator (EOM) and lock-in amplifier are briefly introduced. The EOM and the lock-in amplifier are required to extract the small SRS signal (SRL or SRG). To minimize the noise that enters the lock-in amplifier, a home-made detector system is developed by integrating electronic filter and preamplifier. The reconstructed spectra from spectral SRS microscopy is very similar to that of spectral CARS microscopy. The superiority of SRS microscopy to CARS microscopy in term of non-resonant background is shown. The switching imaging at vibrational frequency of carbon-deuterium (CD) and carbon-hydrogen (CH) bonds of treated adipocytes with deuterated stearic acid is also achieved.

In chapter 5, the results of spectral CRS microscopy application for intracellular lipid imaging are discussed. The confirmation of lipid uptake can be concluded. A remarkable

wide tuning range can also be resolved by the value of 1000 cm^{-1}. The observation of lipid uptake from two types of lipid reveals the possible existence of their different metabolic pathways. It is also demonstrated the significant accumulation of lipid by the fibroblasts which may relate to the indication of lipid storage disorder. On the other hand, the results also show that certain lipid was less accumulated so that it has a potential for treatment of lipid-related disease.

Finally, the conclusion and the perspective of the study are given at the end.

Chapter 1
Review on CRS microscopy

1.1 Principle of CRS microscopy

1.1.1 Nonlinear optical processes

The nonlinear optical process occurs as the consequence of the modification of optical properties of the material illuminated by sufficiently intense optical field **E** which induces polarization **P**. The polarization **P** is then express as a power series of the incident field **E** [11, 12]:

$$\mathbf{P} = \chi^{(1)}\,\mathbf{E} + \chi^{(2)}\,\mathbf{E}\,\mathbf{E} + \chi^{(3)}\,\mathbf{E}\,\mathbf{E}\,\mathbf{E} + \cdots . \tag{1.1}$$

The $\chi^{(n)}$ is known as a n-th order optical susceptibility tensor. The first term denotes the linear interaction that is manifested as one-photon process, such as one-photon absorption. The nonlinear phenomena relate to the rest of the terms and are manifested in various nonlinear optical processes. One of third order nonlinear processes is known as coherent Raman scattering (CRS) that particularly associates to coherent anti-Stokes Raman scattering (CARS) and stimulated Raman scattering (SRS).

In general case, the formulation of polarization $\mathbf{P}^{(3)}$ induced by third order nonlinear optical process can be written as [11, 12]

$$\mathbf{P}^{(3)} = \chi^{(3)}\,\mathbf{E}\,\mathbf{E}\,\mathbf{E} . \tag{1.2}$$

The incident field **E** consists of linear combination of frequency components [11, 12]:

$$\mathbf{E}(t, \mathbf{r}) = \sum \left[\hat{\mathbf{E}}_n \exp[-i\,(\omega_n\, t - 2\pi\, \mathbf{k}_n \cdot \mathbf{r})]\right], \tag{1.3}$$

where $\hat{\mathbf{E}}_n$ is the amplitudes, ω_n is the angular frequency components and $\mathbf{k}_n$ is the wave vector of the incident lights. Thus, Eq. 1.1 can be rewritten using simpler notation in the following equation [11, 12]:

$$\mathbf{P}^{(3)}(t,r) = \sum \left[\mathbf{P}^{(3)}(\omega_n, \mathbf{k}_n) \cdot \exp[-i\ (\omega_n\ t - 2\pi\ \mathbf{k}_n \cdot \mathbf{r})]\right]. \quad (1.4)$$

1.1.2 CARS process

Two incident laser beams with different frequencies ($\omega_1 > \omega_2$) are used for excitation of a specific molecular vibration (Ω) by its beating frequency:

$$\Omega = \omega_1 - \omega_2. \quad (1.5)$$

Both beam at the beating frequency Ω is then mixed with ω_1 beam to coherently generate an anti-Stokes shifted radiation and it is known as CARS (Fig. 1.1a) [13-15]. Frequency of the anti-Stokes shifted radiation is given by [11]

$$\omega_{CARS} = \omega_1 - \omega_2 + \omega_1 = 2\omega_1 - \omega_2. \quad (1.6)$$

Because the frequency difference of the incident beams can only excite a specific Raman active molecular vibration, the generated CARS radiation is also associated to a certain Raman shift of the molecular vibration. Therefore, scanning of the frequency difference is required to reconstruct the CARS spectra.

By assuming that the third order nonlinear susceptibility $\chi^{(3)}$ is uniform in the specimen, the nonlinear polarization induced by $\chi^{(3)}$ in CARS process can be defined as [11, 16, 17]

$$\begin{aligned}\mathbf{P}^{(3)}_{CARS}(t,\mathbf{r}) &= \sum \left[\mathbf{P}^{(3)}(\omega_{CARS}, \mathbf{k}_{CARS})\ \exp[-i\ (\omega_{CARS}\ t - 2\pi\ \mathbf{k}_{CARS} \cdot \mathbf{r})]\right] \\ &= D\ \chi^{(3)}\ \mathbf{E}_1(t,\mathbf{r})\ \mathbf{E}_1(t,\mathbf{r})\ \mathbf{E}_2^*(t,\mathbf{r}) \\ &= D\ \chi^{(3)}\ \hat{\mathbf{E}}_1\ \hat{\mathbf{E}}_1\ \hat{\mathbf{E}}_2^*\ \exp[-i\ \{(2\omega_1 - \omega_2)\ t - 2\pi\ (2\mathbf{k}_1 - \mathbf{k}_2) \cdot \mathbf{r}\}], \end{aligned} \quad (1.7)$$

where *D* denotes the number of permutation of the susceptibility tensor. The wave vector of the CARS polarization should fulfill the condition of constructive interference which is known as the phase matching condition (Fig1.1b) given by

$$\mathbf{k}_{CARS} = 2\mathbf{k}_1 - \mathbf{k}_2. \tag{1.8}$$

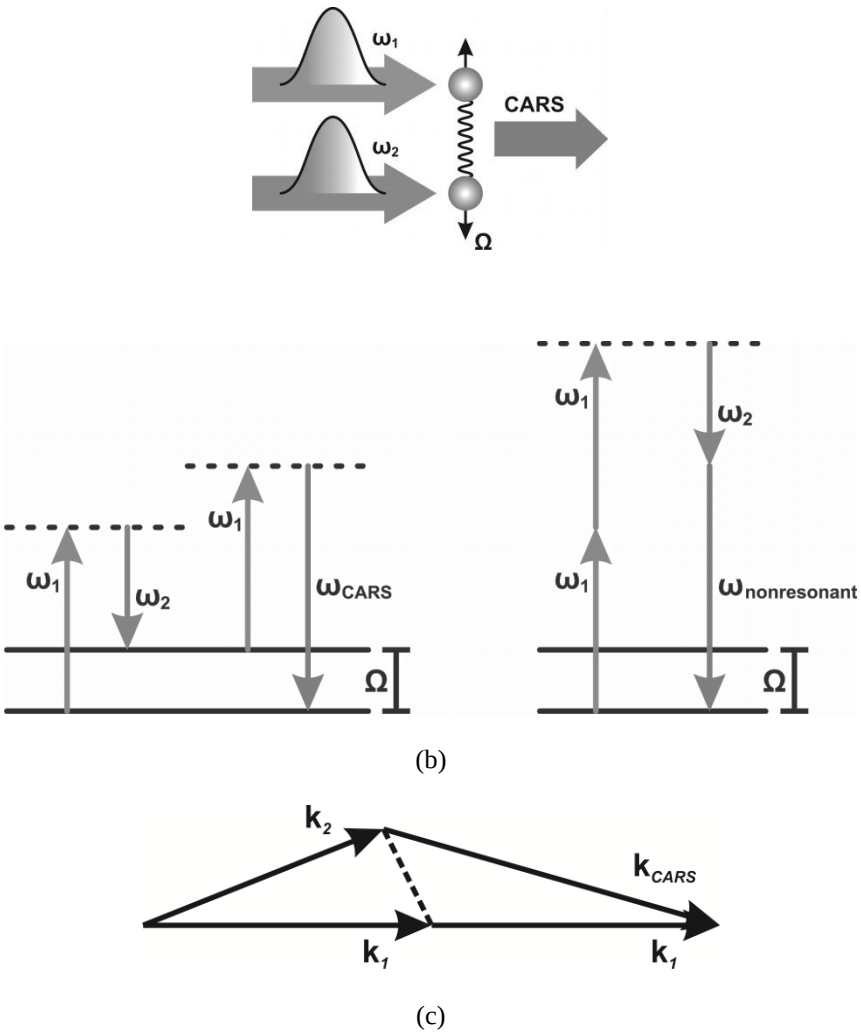

Figure 1.1. CARS process: (a) generation of CARS emission, (b) energy diagram of resonant and nonresonant processes, and (c) phase matching condition.

In CARS, the presence of different color beams induces a mismatch phase between them so that it hinders the effective generation of CARS signal. The setup of conventional CARS spectroscopy avoids the collinear geometry. Consequently, it was considered that to

obtain a satisfying high-spatial resolution under a perfect phase matching condition in CARS microscopy was difficult. However, Hashimoto *et al.* showed that tightly focused incident beams with a high NA objective lens could overcome the difficulty of the strict phase matching condition [18]. The focusing provides the existence of many pairs of $\mathbf{k}_1$ and $\mathbf{k}_2$. In recent application, the CARS images are obtained from the scanning of the tightly focused beams.

1.1.3 SRS process

Stimulated Raman scattering (SRS) process also employs two color laser beams ($\omega_1 > \omega_2$) for excitation of a specific molecular vibration (Ω) by its beating frequency. When the stimulated Raman process occurs, there will be an energy transfer from high frequency pulse ω_1 to low frequency pulse ω_2 (Fig. 1.2a) [19-21]. Consequently, ω_1 pulses experience energy loss (stimulated Raman loss/SRL) while ω_2 pulses experience energy gain (stimulated Raman gain/SRG). In case of SRL process, the beams at the beating frequency Ω is mixed with ω_2 and the signal is detected from ω_1 (Fig. 1.2a). Since the detected signal is very weak, an intensity modulation and a lock-in detection method are applied [20]. Frequency of detected signal is given by [11]:

$$\omega_{SRS} = \omega_1 = \omega_1 + \omega_2 - \omega_2. \tag{1.9}$$

By assuming that the third order nonlinear susceptibility $\chi^{(3)}$ is uniform in the specimen, the nonlinear polarization induced by $\chi^{(3)}$ in SRS process can be defined as [11, 22, 23]:

$$\begin{aligned}\mathbf{P}_{SRS}^{(3)}(t,\mathbf{r}) &= \sum\left[\mathbf{P}^{(3)}(\omega_{SRS},\mathbf{k}_{SRS})\exp[-i(\omega_{SRS}\,t - 2\pi\,\mathbf{k}_{SRS}\cdot\mathbf{r})]\right] \\ &= D\,\chi^{(3)}\,\mathbf{E}_1(t,\mathbf{r})\,\mathbf{E}_2(t,\mathbf{r})\,\mathbf{E}_2^*(t,\mathbf{r}) \\ &= D\,\chi^{(3)}\,\hat{\mathbf{E}}_1\,\hat{\mathbf{E}}_2\,\hat{\mathbf{E}}_2^*\exp[-i(\omega_1\,t - 2\pi\,\mathbf{k}_1\cdot\mathbf{r})].\end{aligned} \tag{1.10}$$

From Eq.1.10, one can easily understand that the phase matching condition is automatically satisfied in SRS process since it depends only on the vector of the detected beam (Fig. 1.2b).

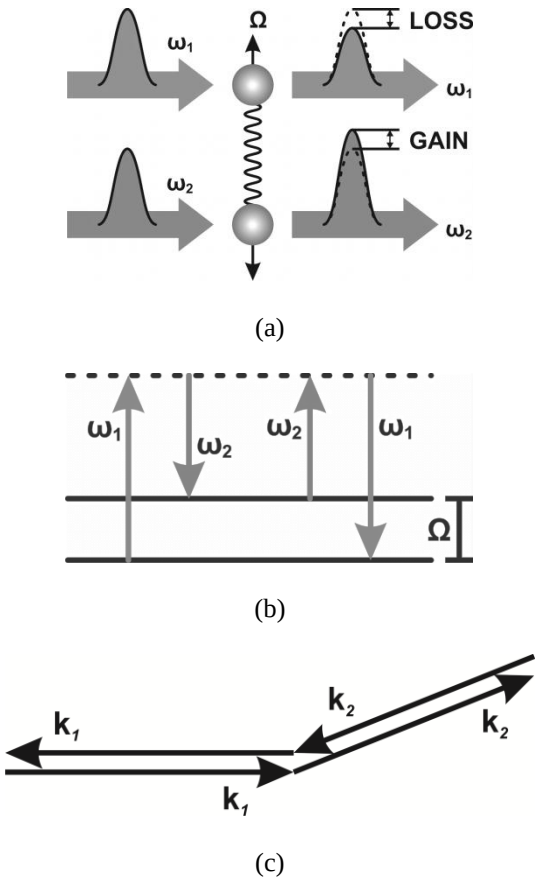

Figure 1.2. SRS process: (a) energy transfer in SRS process, (b) energy diagram of SRS process, and (c) phase matching condition.

1.1.4 Third order nonlinear susceptibility

Here, the general formulation of polarization **P** in Eq. 1.2 is recalled as the power series from excitation fields E for third order nonlinear contribution at ω_4 [11, 12, 16, 17, 22, 23]:

$$\mathbf{P}^{(3)}(\omega_4) = \chi^{(3)}(\omega_4{:}\,\omega_1, \omega_2, \omega_3)\ \mathbf{E}(\omega_1)\ \mathbf{E}(\omega_2)\ \mathbf{E}(\omega_3), \qquad (1.11)$$

where $\chi^{(3)}(\omega_4{:}\ \omega_1,\ \omega_2,\ \omega_3)$ is the third order nonlinear susceptibility and $\mathbf{E}(\omega_1)$, $\mathbf{E}(\omega_2)$, and $\mathbf{E}(\omega_3)$ are the electric field of excitation beams at three distinct frequencies ω_1, ω_2, and ω_3. All CRS processes employ at least two color laser sources (ω_p, ω_s) of which the frequency

difference can be tuned to match with certain molecular vibration Ω. The contributions of both molecular vibration $\chi_r^{(3)}$ and electronic response $\chi_{nr}^{(3)}$ commonly occur during excitation process and are contained in $\chi^{(3)}$ [22]:

$$\chi^{(3)} = \chi_r^{(3)} + \chi_{nr}^{(3)} = \frac{A}{\Omega-(\omega_p-\omega_S)-i\,\Gamma} + \chi_{nr}^{(3)}, \tag{1.12}$$

where *A* is a variable related to specific spontaneous Raman scattering cross section and Γ is the spectral width of the molecular vibration. It can be assumed that the wavelengths of the beams are far from electric transition, thus value of $\chi_{nr}^{(3)}$ is treated as a real constant due to the electronic response of specimen independent from the frequencies of incident fields; whereas $\chi_r^{(3)}$ has real and imaginary components that induce the phase shift of nonlinear polarization with respect to the incident fields. In particular, the polarizations induced by CARS and SRS processes are given by [22]

$$\mathbf{P}^{(3)}(\omega_{CARS}) = \chi^{(3)}\big(\omega_{as}\colon \omega_p, -\omega_s, \omega_p\big)\,\mathbf{E}\big(\omega_p\big)\,\mathbf{E}(-\omega_s)\,\mathbf{E}\big(\omega_p\big), \tag{1.13a}$$

$$\mathbf{P}^{(3)}(\omega_{SRL}) = \chi^{(3)}\big(-\omega_p\colon \omega_p, -\omega_s, \omega_s\big)\,\mathbf{E}\big(\omega_p\big)\,\mathbf{E}(-\omega_s)\,\mathbf{E}(\omega_s). \tag{1.13b}$$

CARS signal can be spectrally isolated from other waves, in this case from the incident beams. Therefore, the detected intensity is proportional to the square of the amplitude signal and the polarization given by [11, 12, 16, 17, 22, 23]

$$I_{signal} = \frac{n(\omega_{CARS})\cdot c}{8\pi}\cdot|E_{CARS}|^2 \propto \left|\mathbf{P}^{(3)}(\omega_{CARS})\right|^2 \propto \left|\chi^{(3)}(\omega_{CARS})\right|^2. \tag{1.14}$$

It clearly suggested that CARS signal suffers from non-resonant background $\chi_{nr}^{(3)}$. Consequently, the obtained spectral shape is often severely distorted.

Optical heterodyne detection can be used for suppressing the non-resonant background by providing local oscillator to measure the real and imaginary part of the nonlinear susceptibility [11, 12, 16, 17, 22, 23].

$$\begin{aligned} I_{signal} &= \frac{n(\omega_d)\cdot c}{8\pi}\cdot|E_d + E_{LO}|^2 \\ &\propto |E_d|^2 + |E_{LO}|^2 + 2\,\mathrm{Re}[E_d]\,\mathrm{Re}[E_{LO}] + 2\,\mathrm{Im}[E_d]\,\mathrm{Im}[E_{LO}] \end{aligned} \tag{1.15}$$

where E_d and E_{LO} are the fields of detected signal and local oscillator, ω_d is the frequency of detected signal, and ω_p and ω_s are frequency of incident lasers. In CARS microscopy, the introduction of the third beam is needed for this heterodyne detection at the same wavelength as ω_{CARS}. On the other hand, SRS microscopy does not required the third beam because the SRS occurs at the same frequencies of excitation beams. The frequency and polarization of the new emission generated in SRS process are identical to the excitation beams. When $|E_d| \ll |E_{LO}|$, the contribution of $|E_d|^2$ is negligible in Eq. 1.15 and $\mathrm{Im}[E_{LO}] = 0$, so that Eq. 1.15 can be written in simpler form:

$$I_{signal} = |E_{LO}|^2 + 2\,\mathrm{Re}[E_d]\,\mathrm{Re}[E_{LO}]\,, \tag{1.16}$$

The detected signal E_d induced by the nonlinear polarization $P^{(3)}$ can be obtained by solving the Maxwell wave equation:

$$\nabla \times \nabla \times E_d + \frac{n^2}{c^2}\ddot{E}_d = -\frac{4\pi}{c^2}\,\ddot{\mathbf{P}}^{(3)}. \tag{1.17}$$

By considering certain distance l in the nonlinear material, one can define the detected signal from the solution of Eq. 1.17 as follow

$$E_d = -\frac{4\pi i}{n}\,\frac{\omega}{c}\,l\,\mathbf{P}^{(3)}\,\mathrm{sinc}(\mathbf{K})\,\exp(i\mathbf{K}), \tag{1.18}$$

where **K** here is a simplified definition and form of wave vector phase. For convenience in describing the following explanation, first it is defined that

$$\chi^{(3)} = \chi_{real} + i\,\chi_{imaj}, \tag{1.19}$$

Then Eq. 1.18 can be rewritten as

$$\begin{aligned} E_d &= -\frac{4\pi i}{n}\,\frac{\omega}{c}\,l\,\chi^{(3)}\,E^3\,\mathrm{sinc}(\mathbf{K})\,\exp(i\mathbf{K}) \\ &= \frac{4\pi}{n}\,\frac{\omega}{c}\,l\,\left(i\,\chi_{real} + \chi_{imaj}\right)E^3\,\mathrm{sinc}(\mathbf{K})\,\exp(i\mathbf{K}) \end{aligned} \tag{1.20}$$

Therefore, one can get

$$\mathrm{Re}[E_d] \propto \mathrm{Im}\left[\chi^{(3)}\right]\,\mathbf{E}\,\mathbf{E}\,\mathbf{E} \tag{1.21}$$

Recalling Eq. 1.16 and Eq. 1.21, the detected signal is given by

$$I_{signal} = |E_{LO}|^2 + 2\,\mathrm{Im}\left[\chi^{(3)}\right]\mathrm{Re}[E_{LO}]\,\mathbf{E^3}\ , \tag{1.22a}$$

$$I_{signal} \propto Im\left[\chi^{(3)}\right]. \tag{1.22b}$$

From the Eq. 1.22, one can easily see that SRS signal is only sensitive to the imaginary part of $\chi^{(3)}$. SRS is then considered as a special case of intrinsic optical heterodyne detection. As the result, the non-resonant background is not detected in SRS microscopy and the SRS spectra are very identical to those of spontaneous Raman scattering.

1.1.5 Laser requirements for CRS microscopy

A laser source that can produce short pulses with high peak power is preferable for excitation beam in CRS microscopy in order to generate sufficient signal induced by nonlinear optical phenomena. However, the spectral resolution is limited by the spectral width of the incident laser pulses. Ultrashort pulse lasers are commonly applied for the excitation sources in CRS microscopy. Femtosecond laser can provide high peak power for CRS microscopy; however, it has poor spectral resolution for vibrational imaging without any processing of pulse shaping. On the contrary, picosecond laser can assure suitable spectral resolution for nonlinear Raman microscopy; but it lacks of high peak power and capability for pulse shaping. In short, the fulfillment of both short pulse and high spectral resolution cannot be satisfied simultaneously because of the Fourier transform relation between them. It is assumed that the laser has a Gaussian distribution profile which has a complex envelope with constant phase and Gaussian magnitude [24]:

$$\mathbf{A}(t) = \mathbf{A}_0 \exp\left[-\frac{t^2}{\tau^2}\right], \tag{1.23}$$

where τ is the real time constant. The intensity of pulse is defined as

$$\mathbf{I}(t) = \mathbf{I}_0 \exp\left[-\frac{2t^2}{\tau^2}\right], \tag{1.24}$$

with $\mathbf{I}_0 = |\mathbf{A}_0|^2$. The pulse duration expressed in full width at half maximum (FWHM) is then given by

$$\tau_L = \sqrt{2\ln 2}\,\tau. \tag{1.25}$$

The spectral intensity is equal to the to the square of the Fourier transform of **A**(t):

$$\begin{aligned}\mathbf{S}(\nu) &= |\mathcal{F}[\mathbf{A}(t)]|^2 \\ &\propto \exp[-2\pi^2\tau^2\nu^2].\end{aligned} \tag{1.26}$$

The FWHM of spectral bandwidth $\Delta\nu$ from $\mathbf{S}(\nu)$ is given by

$$\Delta\nu = \frac{\sqrt{2\ln 2}}{\pi\,\tau}. \tag{1.27}$$

As the function of the time constant τ, Eq. 1.25 and Eq. 1.27+ can be substituted into each other and the substitution results in

$$\tau_L\,\Delta\nu = \frac{2\ln 2}{\pi} = 0.441 \tag{1.28a}$$

or

$$\tau_L\,\Delta\omega_L = 4\ln 2 = 2.773, \tag{1.28b}$$

since $\Delta\omega_L = 2\pi\,\Delta\nu$. As the typical spectral bandwidth of molecular vibration is about 5 cm^{-1} [15], the required spectral resolution of the laser pulse is around 3–5 cm^{-1} or equal to pulse duration of 3–5 ps.

The frequency difference of incident beams in CRS microscopy can only excite a specific molecular vibration. In order to obtain CRS spectra, scanning of the frequency difference is needed, which means that one of the laser sources should be capable of wavelength tuning while the other one should maintain the wavelength. A common method to enable the wavelength scanning is the use of optical parametric amplifier (OPA) or optical parametric oscillator (OPO) [20, 25-30]. One can also apply a broad-band spectrum light which is be provided by femtosecond laser [31-33] or supercontinuum light generated by photonic crystal fiber (PCF) [34, 35]. Instead of tuning the wavelength, the broad-band

source enables the multiplex detection and the spectral information is retrieved using spectrum analyzer. Recently, a tunable laser from fiber laser system is also introduced to enable spectral CRS imaging [36].

1.1.6 General setup of CRS microscopy

CRS microscopy employs two color lasers that are overlapped spatiotemporally on the sample plane (Fig. 1.3). Typically, two lasers with picosecond pulse duration are employed to achieve high spectral resolution. The synchronization of two independent laser pulses is obligated to reduce to generate an effective CRS signal. By considering that scanning the wavelengths for spectral imaging is time consuming, a multiplex system has been developed using combination of narrow-band and broad-band laser sources [31-35]. Forward detection and backward detection (epi detection) are the general detection schemes for acquiring CRS signal (Fig. 1.3). Forward detection is the most popular configuration because the direction of detected CRS signal is strongly confined in the forward direction. Epi detection method is developed by considering the need of observing specimen with poor-transparency or significant thickness [37, 38]. Additionally, the epi detection can be used to reject the contribution of non-resonant background because of the destructive interference occurred in backward direction. For improvement of detection, the previous detection scheme is combined with other specific method, such as: polarization sensitive detection, time-resolved detection, heterodyne detection, and so on [39-41].

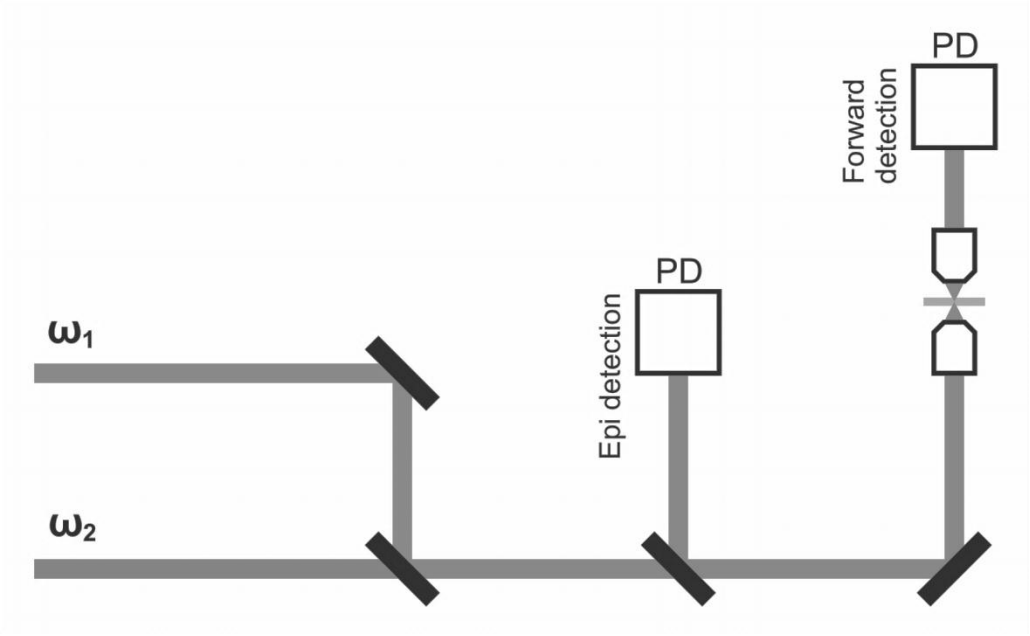

Figure 1.3. General setup of CRS microscopy: two lasers are overlapped and focused on sample, then the CRS signal is detected in the forward or backward direction

1.2 Tunable laser source for spectral CRS microscopy

1.2.1 Optical parametric oscillator

Optical parametric denotes a nonlinear optical process in which the initial and final quantum-mechanical states of the system are identical. Photon energy is always conserved during a parametric process. Parametric process can be described by a real susceptibility [11, 12]. One of the optical parametric phenomena is the optical parametric generation as shown in Fig. 1.4a. The illuminated material by incident laser beam ω_3 which is known as pump generates output fields ω_1 and ω_2 which are known as signal and idler, respectively. This material is placed inside an optical oscillator of which the mirrors highly reflect the signal and/or idler beams (Fig. 1.4b). During the reflection in the forward and backward direction, a parametric optical amplification based on the second order difference-frequency generation is occurred (Fig. 1.5). The presence of ω_3 and ω_1 generates ω_2 which has value of the frequency

difference between ω_3 and ω_1 ($\omega_2 = \omega_3 - \omega_1$). Likewise, in further process, the presence of ω_2 field stimulates the generation of ω_1 field. Thus, the generation of ω_1 field reinforces the generation of ω_2 field, and vice versa, leading to the growth of the both fields simultaneously [11, 12]. Optical parametric amplifier (OPA) follows the similar principle where the initial process is started by providing incident beams ω_3 and ω_1, where in this case ω_1 is known as seed to obtain the signal ω_2.

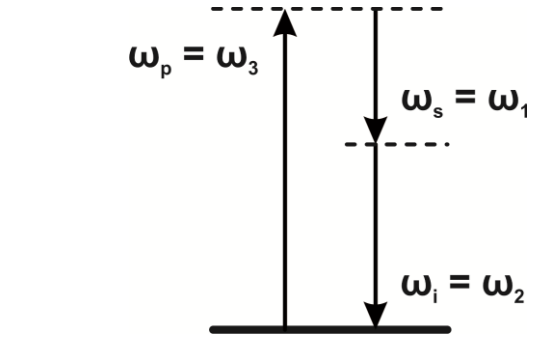

(a)

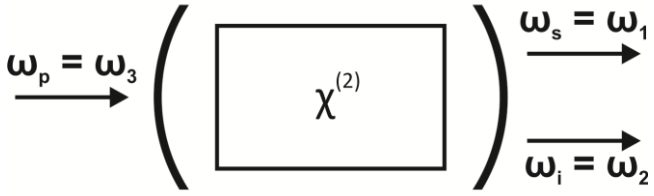

(b)

Figure 1.4. Optical parametric oscillator (OPO): (a) energy diagram of optical parametric generation in OPO, and (b) schematic of OPO

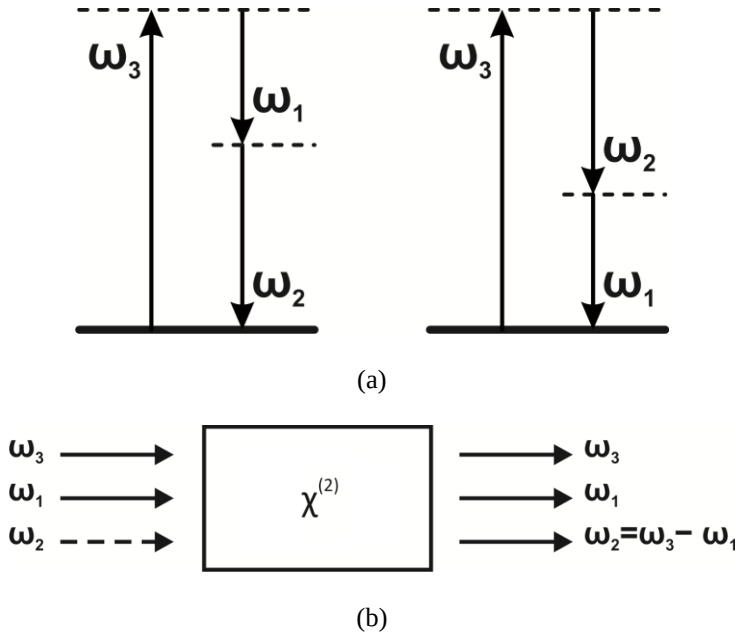

Figure 1.5. Second order difference-frequency generation: (a) energy diagram of second order difference-frequency generation, and (b) schematic of second order difference-frequency generation process

One usually calls ω_1 field, ω_2 field, and ω_3 field as signal, idler, and pump waves. The material that generates signal and idler beams is placed inside an optical oscillator of which the mirrors highly reflect the signal and/or idler beams (Fig. 1.5). The oscillation occurs as the consequence of the gain of the optical parametric amplification process and the device is known as optical parametric oscillator (OPO). The OPO has been proven as a reliable laser source with wavelength tunability over violet, visible, and infrared spectral regions [42, 43].

A very strict phase matching condition should be fulfilled to produce the amplified signal pulses using OPA/OPO [11, 12, 44-48]. Generally, OPA suffers from low power stability [44] and limited bandwidth during the tuning of grating [45]; whereas it is difficult for adjustment of OPO cavity length because it must be completely coincident with that of excitation beam [46, 47]. Angular orientation and temperature of nonlinear optical crystal should be carefully calculated and well maintained for developing a stable OPO laser source [48]. Though OPO has enough tunable range to cover whole Raman spectral region, OPO requires at least several tens of seconds for wide tuning range [27].

1.2.2 Femtosecond and picosecond mode-locked lasers

A femtosecond mode-locked laser is usually applied as the broad-band laser source for multiplex CRS microscopy. Femtosecond mode-locked laser has pulse-width characteristic on the order of picosecond to femtosecond, which in practice is typically around several hundreds of cm^{-1} or equal to around several tens of fs. The femtosecond laser is a type of ultrashort pulse laser which generates the pulse by superposition of a huge number of frequencies. Recently, the solid-state laser is preferable than dye laser because it provides stabler output with wider tunable range. In particular, Ti:sapphire laser generates the output with the wavelength at near infra-red region and it is suitable for biological application [49]. The main advantage of using femtosecond laser is the capability to access certain spectral region simultaneously. However, as it has been mentioned earlier, the femtosecond pulse hinders the achievement of high spectral resolution. For example, the overall spectral bandwidth of detected signal decreases by the rise of chirp rate because spectral components of the chirp pulse overlap with the detected spectral signal [31, 32]. One method to improve the spectral resolution of the femtosecond laser for multiplex imaging is pulse shaping [31, 32].

A picosecond mode-locked laser, on the contrary, provides a high spectral resolution with typical achievement of a few of cm^{-1}. It is also another type of ultrashort pulse laser. The tunability of the picosecond laser is usually achieved by rotating the intracavity birefringent filter [50]. The crystal material of the birefringent filter changes the polarization of pump laser into elliptical orientation and only limited wavelength range of output laser can remain linearly polarized. It also hinders pulses to reach lasing threshold, but only only narrow range of wavelength. Though a mechanical tuning is required in the setup, the adjustments of cavity length and temperature have been eliminated.

1.2.3 Fiber laser system and photonics crystal fiber

Fiber laser system enables the development of maintenance-free and compact system with relatively low cost. Additionally, the problem of optical alignment can be solved accordingly because the fiber laser system also provides permanent optical pathway once the setup is done. Some CRS microscopy systems employ fiber laser as both pump and Stokes sources [51] or only as Stokes source while another laser is served by picosecond mode-locked laser [21, 36]. The requirement of spectral resolution of CRS microscopy can also be achieved by fiber laser system. The typical wavelength generated from fiber laser system (around 1000 nm) enables the application of this type of laser source for biological application as well. The main challenge in the design of fiber laser system is the length of fiber which relates to the material nonlinearity. For CRS microscopy application, the dominant concern is that the nonlinearity of the fiber material may restrain the spectral pulse width and tunable range of the laser.

Supercontinuum light generated from photonics crystal fiber (PCF) can be used as a broadband light to serves as Stokes beam in multiplex CRS system [34, 35]. The supercontinuum light shares similar characteristic with femtosecond laser. It also takes the advantage of simpler, more compact setup than the bulk lasers do. Additionally, an ultrabroadband spectrum can be achieved which may cover a very wide range from fingerprint region to CH vibrational region.

1.3 Applications of CRS microscopy

1.3.1 Applications of CARS microscopy in biological imaging

CARS microscopy offers a label-free imaging with high molecular sensitivity for biological applications. One most suitable implementation of CARS microscopy is intracellular dynamics of lipid, particularly in lipid droplets (LDs) [8, 52-54]. This advantage comes from the fact that lipid contains abundant CH bond in its structure which generates strong Raman signal in specific region around 2850 cm^{-1}. With the complex profile, study of lipid becomes more popular recently. One of the most popular methods to observe the LDs is the application of fluorescent dyes for lipid such as Oil Red O (ORO) and Nile Red. However, the staining method usually provides indirect method because it is only applicable to fixed samples. Additionally, staining method also induce the deformation of LDs structure due to the used of methanol as solvent [8]. A good contrast can be achieved by CARS microscopy that is comparable to fluorescence microscopy. Furthermore, CARS microscopy can overcome the photobleaching problem that usually occurs in fluorescence microscopy. This feature is important for the application of time-course imaging to observe the lipid dynamics in living cells.

Detection of drug delivery in body is another interesting subject in biological imaging. The knowledge of drug-cells interaction is still limited and unclear. It is crucial to reveal the mechanism of drug action at cellular level and the cell response in order to determine the effectiveness of drug dosage given. Observation of CARS images in the fingerprint region provides more information of different chemical structures that may relate to the metabolism of drug [55, 56] or the chemical components of the drug [57]. At the tissue level, CARS images cover larger observation area and give major description of in vivo the drug delivery [25, 58].

1.3.2 Applications of SRS microscopy in biological imaging

SRS microscopy surpasses CARS microscopy in term of non-resonant background. SRS microscopy enables more sensitive biological imaging with less distortion of spectral line shape. The applications of SRS microscopy in biological imaging are very similar to those of CARS microscopy. Detection of intracellular lipid storage can be successfully performed in the CH vibration around 2850 cm^{-1} [29, 30, 33, 59, 60] and the fingerprint region around [19-21]. Various cellular structures such as cytoplasm, nucleus, and lipid droplets can be clearly distinguished by spectral imaging in the fingerprint region [61]. Observation of chemical compounds in drug [38] and the dynamics of drug delivery in tissue scale [62] using SRS microscopy are also demonstrated. In conclusion, SRS microscopy shares the same applications for biological imaging as CARS microscopy.

1.3.3 Enabling CRS microscopy in the Raman silent region

Biological specimen does not generate any Raman signal in spectral region stretched from 1800 – 2800 cm^{-1}. Rather than disadvantage, this behavior becomes very useful to enhance the application of CARS and other Raman-based microscopy for biological imaging. CD is known as the isomorphic structure of CH which generates blueshifted spectra around 2100 cm^{-1} [3, 63-65]. This isotope does not affect to the original function and reaction of lipid [64]. Other candidates for this purpose is nitrile bond (–C≡N) which have characteristic band at 2250 cm^{-1} [66]. In corporation with alkyne, –C≡C– generates Raman signal at 2120 cm^{-1} [67]. These molecule structures can act as Raman-tag for more sensitive CRS imaging applications.

1.4 Summary

CRS microscopy has potential as powerful label-free imaging tool for biological application. Spectral imaging and fast imaging will provide more advantages for observation of dynamics processes. Development of laser source which has wavelength tunability over wide range with high spectral resolution is required. Yet, it also has to produce stable power and be easily synchronized.

Chapter 2
High-speed tunable picosecond laser system for CRS microscopy

2.1 Introduction

It is found that the development of an ideal laser source for CRS microscopy still remains a challenge, especially for realizing a fast spectral imaging system. A tunable laser source is required for providing a Stokes beam for exciting various molecular vibrations, so that specific vibrational signatures in Raman spectra can be obtained. Therefore, the tunable laser should have high spectral resolution yet wide-range tunability. To observe the dynamics of biochemical processes, the laser should also have a fast tuning ability while providing sufficient, stable power. Moreover, good synchronization between the pump and Stokes beams should be maintained during the wavelength tuning.

A picosecond mode-locked laser has been used as a narrowband tunable laser source to achieve high spectral resolution [19, 38, 68, 69]. In biological applications, Raman spectra are usually observed in fingerprint and CH vibrational regions, typically around 1000 cm^{-1}, respectively [3, 15, 21]. Further enhancement can be achieved by extending the observation range to the silent region at 1800–2800 cm^{-1} where some Raman-tag molecules generate signals without any interference from biological specimens [63, 66, 67]. Fast wavelength tunability can be achieved by application of electronically control tuning system, such as an acousto optics tunable filter (AOTF) [70-75]. The tunable laser can be synchronized with other laser via feedback control with phase-locked loop technique [76, 77]. I adopted the

picosecond AOTF mode-locked laser from Megaopt as the tunable laser in the developed CRS microscopy system.

2.2 High-speed tunable picosecond laser

2.2.1 Schematic of high-speed tunable picosecond laser system

A high-speed tunable picosecond laser is based on the Ti:sapphire picosecond mode-locked laser equipped with an acousto optic tunable filter (AOTF) for the wavelength tuning (Megaopt). Another laser with the wavelength of 532 nm (Millenia Pro 5s, Spectra Physics) is used as the pump source for the operation of the Ti:sapphire picosecond mode-locked laser. For synchronization with another picosecond mode-locked laser, the end mirror is attached on a piezoelectric actuator (Model 840.10, 15 μm, PI). More compensation for repetition frequency change is introduced by installing a pair of parallel-plates pair (W2-PW1-1940-C-670-1064-45P, CVI Melles Griot) mounted on the galvanometer motors (PSM-130, Harmonic Drive Systems). The schematic of the modified AOTF laser is shown in Fig. 2.1.

Synchronization between the two lasers is determined by the time difference of the pulses. Therefore a pulse synchronization system with timing jitter detection is essential in the realization of tunable laser source for the CRS microscopy. I developed the high-speed tunable laser with pulse synchronization system that applied two types of timing jitter detection: an electronic phase detector and a balanced cross correlator (Fig. 2.2).

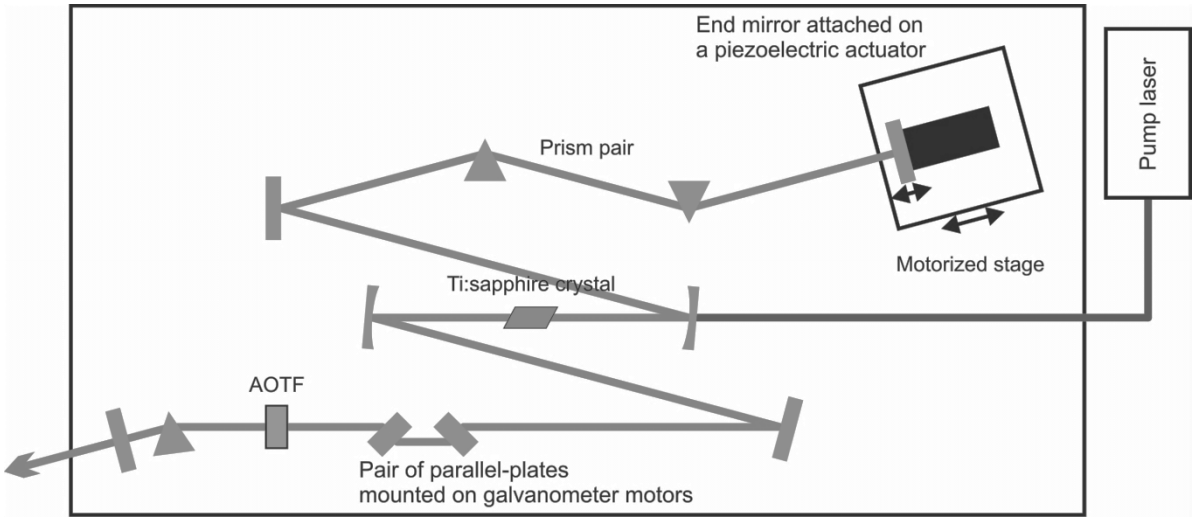

Figure 2.1. Schematic of high-speed tunable laser: a Ti:sapphire crystal pump by another laser (Millenia Pro 5s, 532 nm, Spectra Physics), end mirror attached on piezoelectric actuator (Model 840.10, 15 μm, PI), a pair of parallel-plates (PSM-130, Harmonic Drive Systems) mounted on galvanometer motors.

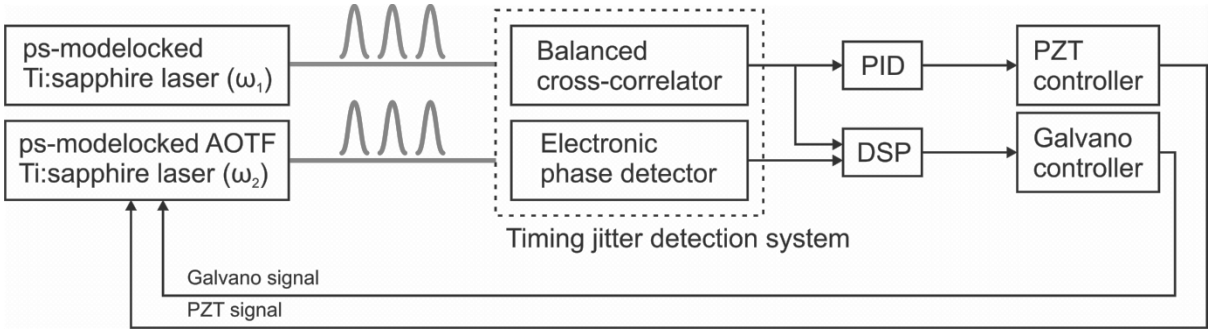

Figure 2.2. Pulse synchronization system that including two types of timing jitter detection system: an electronic phase detector and a balanced cross-correlator

2.2.2 Principle of AOTF

The AOTF is a piezoelectric device made from a birefringent crystal that alters the diffracted wavelength of incident light due to the applied acoustic waves [70, 71]. The birefringence of an anisotropic crystal is altered by the periodic compression and refraction wavefront as an acoustic wave propagating in the crystal. A certain wavelength of diffracted light can be extracted from broadband or multi-color light source by applying adequate

frequency and amplitude of the acoustic wave. Therefore, the wavelength of diffracted light can be tuned by varying the frequency and amplitude of the acoustic wave. With this feature, the AOTF can be used as the wavelength tuning system in the tunable laser source.

The common material of AOTF crystal to enable the operation in the near infrared region is Tellurium Dioxide (TeO_2) that is usually set in noncollinear arrangement where propagation of the acoustic wave in the crystal is at slightly different angle (Fig. 2.3) [70-72]. The acoustic wave is generated by an acoustic transducer bonded on one side of the TeO_2 crystal. The transducer is driven by a radio frequency (RF) wave and its frequency equals to that of the RF wave. As this acoustic wave propagates in the crystal, the alternate compression and relaxation occur on the crystal lattices and induce the periodic modulation of the refractive index. However, the AOTF can only diffract a limited bandwidth of optical frequency of the incident light because of the accumulation of diffractive light over sufficiently thick area of interaction which can satisfy the phase matching condition. The center wavelength of diffracted light will change accordingly with the RF frequency to maintain the phase matching condition. One can assume that the diffracted light has a specific wavelength of which the value is equal to the center wavelength. A couple of orthogonal diffraction is produced, so that it should use an aperture to stop the undiffracted, broadband light and one of the two orthogonally polarized, diffracted lights.

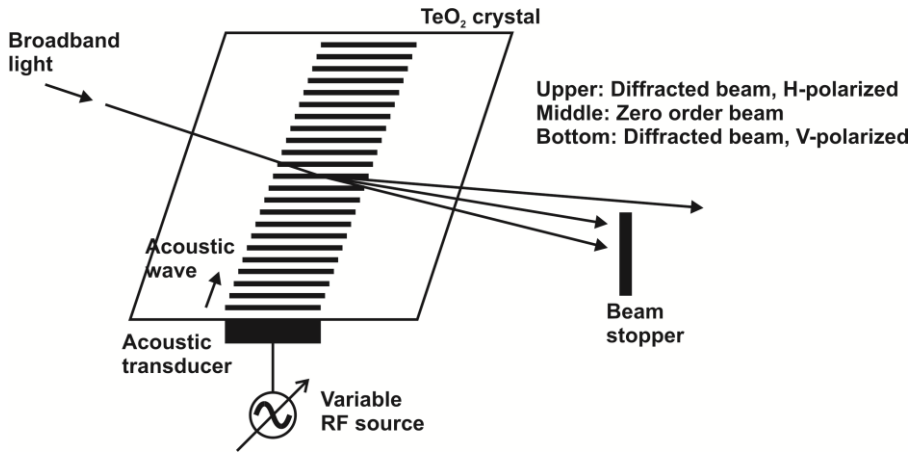

(a)

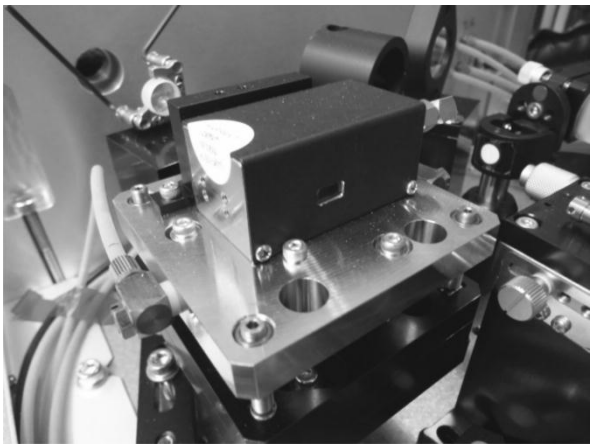

(b) (c)

Figure 2.3. (a) Schematic of AOTF made from TeO2 crystal in noncollinear configuration. The photographs of (b) AOTF device installed in the laser cavity and (c) the AOTF driver (Megaopt).

2.2.3 Electronically tunable picosecond mode-locked laser

First report on the development of AOTF application for wavelength tuning of Ti:sapphire laser is provided by S. Wada *et al* [73]. The characteristic of the TeO_2 crystal used in the AOTF was observed to obtain the information about the damage threshold and the diffraction efficiency using the conventional pulsed Ti:sapphire laser with nearly TEM_{00} mode. They found that an intensity of 42 MW/cm^2 at 781 nm initiated the damage to the crystal and a diffraction efficiency of 97.5% from 1.2 mm-diameter parallel beam could be

reached by applying RF input power of 1 W. The diffraction angle by the AOTF hindered the capability of wider tunable range. This deviation was compensated by introducing a prism at suitable orientation so that a wider wavelength tuning range produced sufficiently small, uniform deviation (Fig. 2.4). They could dramatically improve the tunable range from 12 nm to more than 100 nm. Then they put the Ti:sapphire crystal between an optical oscillator to generate a continuous wave laser and installed the AOTF in the optical pathway to enable the wavelength tuning. They demonstrated the tunability of the Ti:sapphire laser over a wide range without any involvement of mechanical action [74]. The wavelength of the self-starting picosecond laser pulses can be rapidly and arbitrarily accessed in the region from 760 to 880 nm by simply adjusting the RF via a computer.

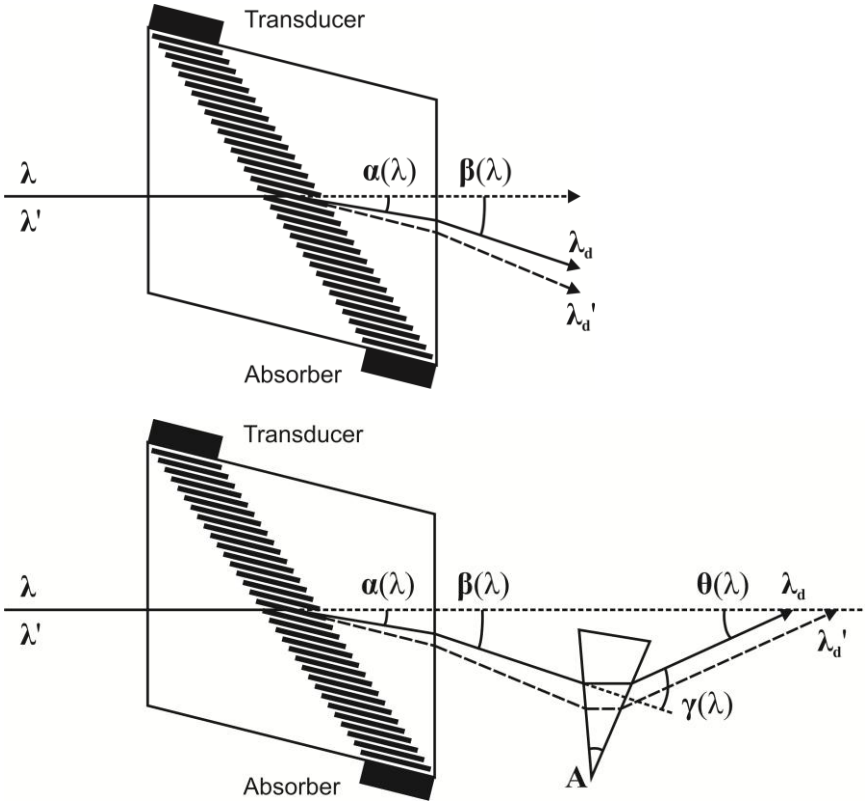

Figure 2.4. Correction of deviation of deflection angles caused by the AOTF

During the observation of the continuous wave Ti:sapphire laser tuning using AOTF, when the output coupler with 98% reflectivity was used, the laser showed a dual operating behaviors: continuous wave and mode-locked like modes. The mode-locked like pulse might possibly generated in the AOTF laser since the AOTF also served as the frequency shifter. When the frequency shift matched to the cavity round-trip frequency, the mode-locked like behavior was started and this condition can be maintained even when the RF was set far from the resonant frequency [74], which meant that presence of the AOTF that induced the frequency shift contributed no fatal effect to the mode-locking. They also remarked that the AOTF laser was also relatively insensitive to the detuning of the cavity length.

Regarding the combination of spectral shifting and filtering, one should realize that it will change the dynamics of the operation of Ti:sapphire mode-locked laser. Self-starting mode-locking was found to be a straightforward consequence of the competition between the frequency shift induced by the AOTF, the reshaping of the spectrum because of the frequency dependent loss and nonlinear spectral broadening. S. Wada, et al. noted that the nonlinear interaction in the laser medium might not be a unique reason for the mode-locked behavior [75]. They believe that linear and nonlinear interaction in the AO medium also plays important roles in dynamics and mode-locking in AOTF laser. The cavity resonance between cavity frequency and the RF may further enhance these nonlinear optical interactions and lead to a lower pump threshold for the self-starting mode-locked behavior.

The effect of diffraction angle deviation at the AOTF, the amount of beam shift, and the phenomenon of AOTF as frequency shifter laser seems to contribute to the mode-locking behavior of the AOTF laser. However, whole picture of the phenomenon of AOTF laser should include more causes and it has not been revealed completely yet.

2.2.4 Basic performance of picosecond AOTF mode-locked laser

The schematic of commercial picosecond AOTF mode-locked laser from Megaopt was described in Fig. 2.5 with specification shown in Tab. 2.1.

Table 2.1. Specification of picosecond AOTF mode-locked laser given by Megaopt

Picosecond AOTF mode-locked laser (Megaopt)	
Output wavelength region	850 – 920 nm
Spectral width	< 0.3 nm (FWHM)
Wavelength scanning amount	< 0.1 nm
Center wavelength repeatability	< 0.2 nm
Wavelength scanning speed	< 1ms
Pulse width	< 20 ps
Average output	> 100 mW
Output stability	< ± 3% pp (peak-to-peak) on arbitrary minute
Output beam diameter	< 2.0 mm
Output mode, beam quality	TEM_{00}, M^2 2
Polarization	Linear (perpendicular)

The AOTF is driven by two RF waves: RF1 is correlated to the wavelength lasing and RF2 is fixed at 110 MHz to stabilize the AOTF operation (Fig 2.6a). The intensity of RF1 is then adjusted to the optimal setting of laser intenstity at each wavelength, while the intensity of RF2 is following to provide constant value of RF power by 1 W which maintains the temperature change of the AOTF (Fig. 2.6b). Figure 2.7 shows the relation between laser output intensity and wavelength. All the characteristics shown above refer to the AOTF laser before modified into the synchronous laser by introducing new components into the laser cavity.

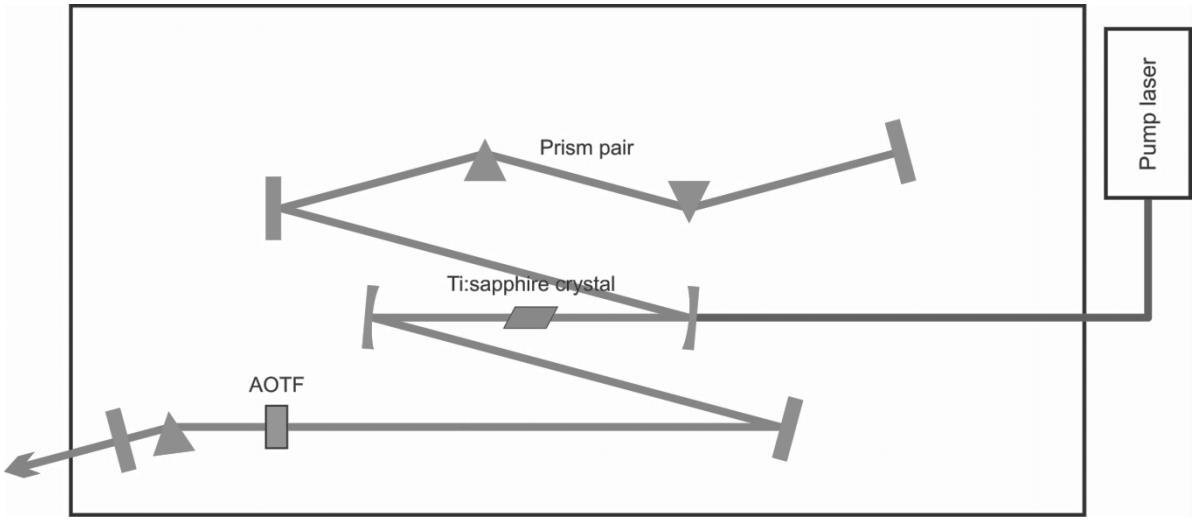

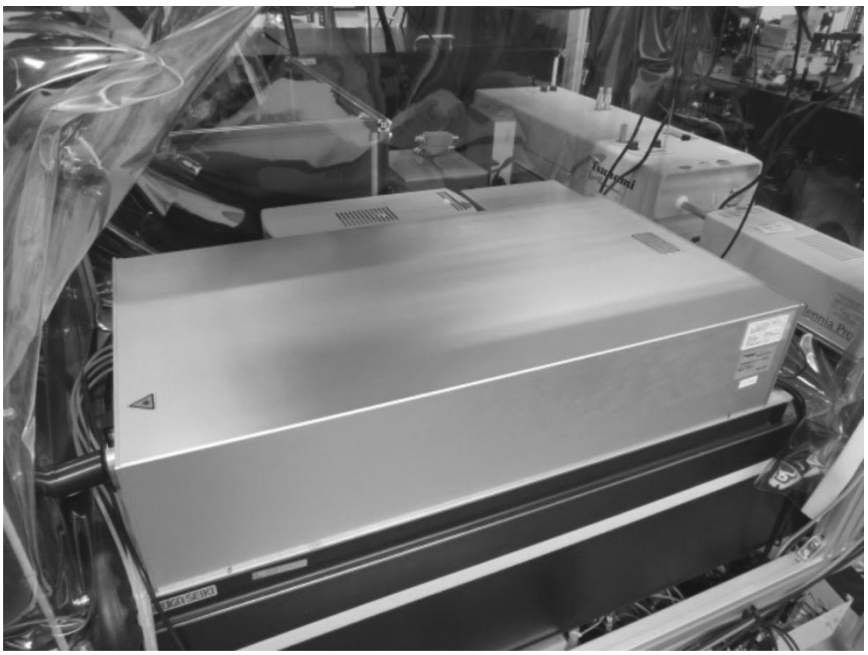

Figure 2.5. Schematic and photograph of commercial picosecond AOTF mode-locked laser (Megaopt)

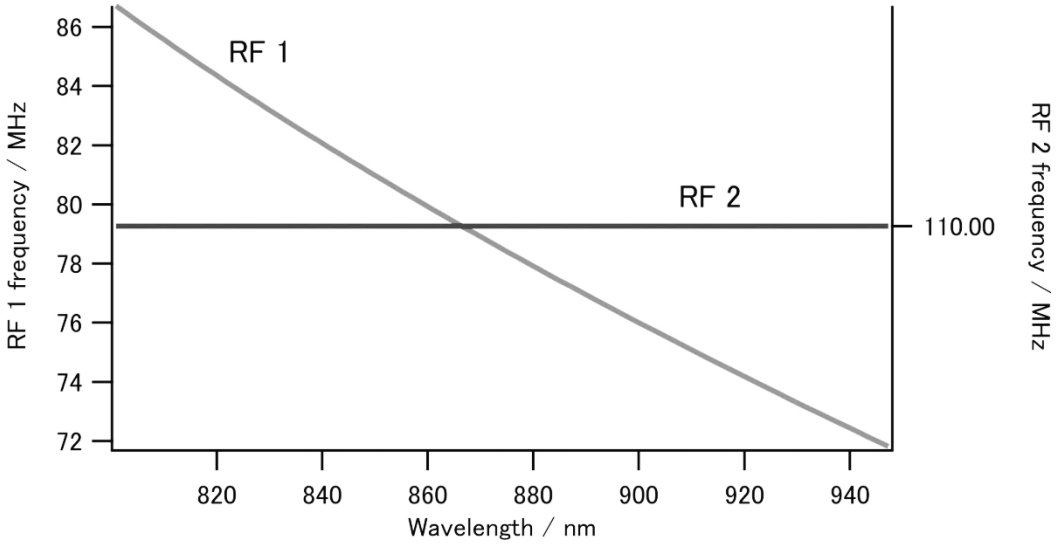

(a)

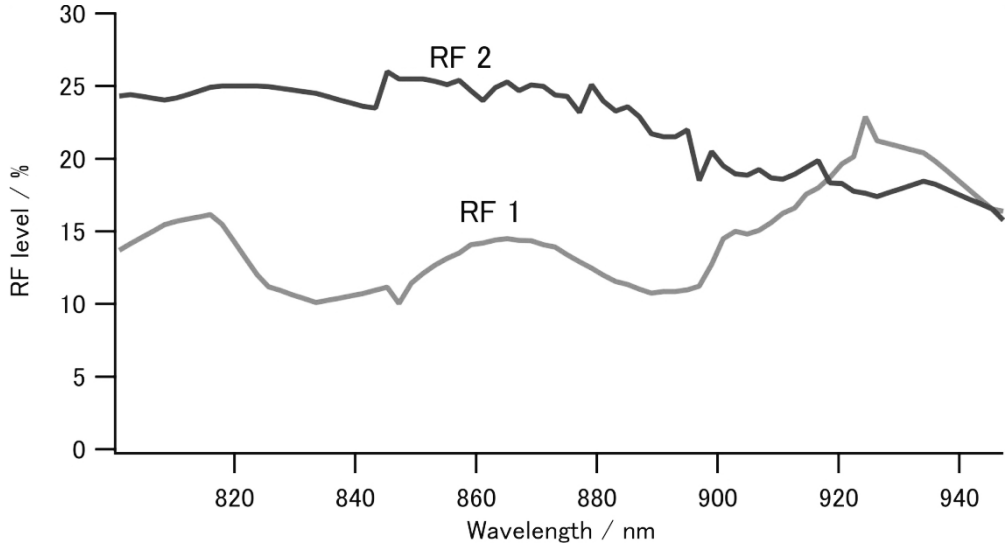

(b)

Figure 2.6. (a) Relation between RF given to the AOTF and output wavelength: RF 1 signal is correlated with the lasing wavelength and RF 2 is fixed at 110 MHz. (b) Relation between RF level given to the AOTF and output wavelength: the level of RF 2 is tuned so that total RF power is constant at 1W. The unit % represents the intensity of the RF generated by the AOTF driver.

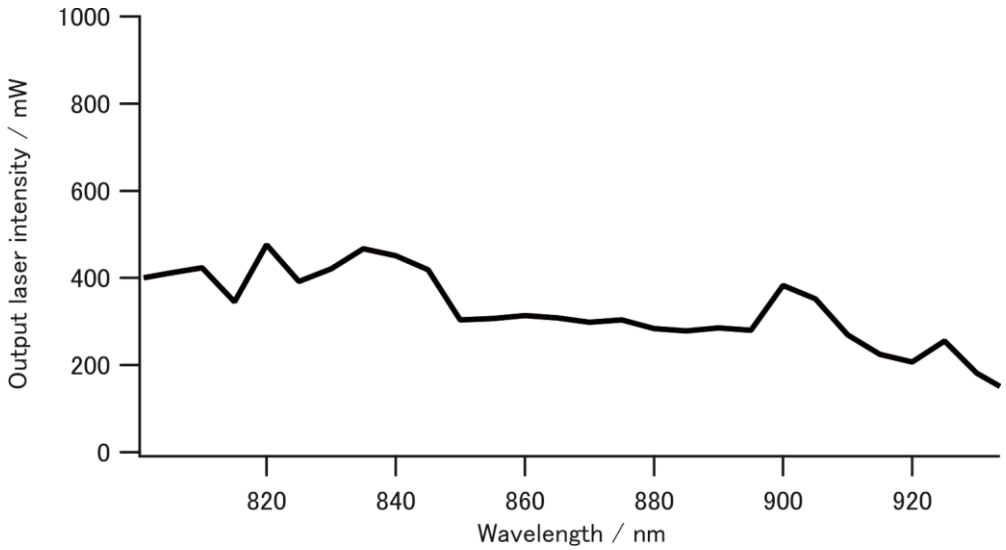

Figure 2.7. Relation between laser output intensity and output wavelength.

The AOTF laser can oscillate over the wide wavelength region without the need of cavity tuning. However, a repetition frequency change by the significant value of around 56.8 kHz occurred during the wavelength scanning from 800 nm to 957 nm (Fig. 2.8). The relationship between the repetition frequency, *f*, and the laser cavity length, *L*, is given by $f = c / 2L$, where *c* is the speed of light. This repetition frequency change was induced by the material dispersion of the optical components in the laser cavity which was dominated by the AOTF crystal. To compensate for the repetition frequency change, a high dispersion prism (SF-10) was place inside the laser cavity. It succeeded to reduce the repetition frequency change to around 43.9 kHz during the wavelength scanning from 800.95 nm to 933.60 nm (Fig. 2.8).

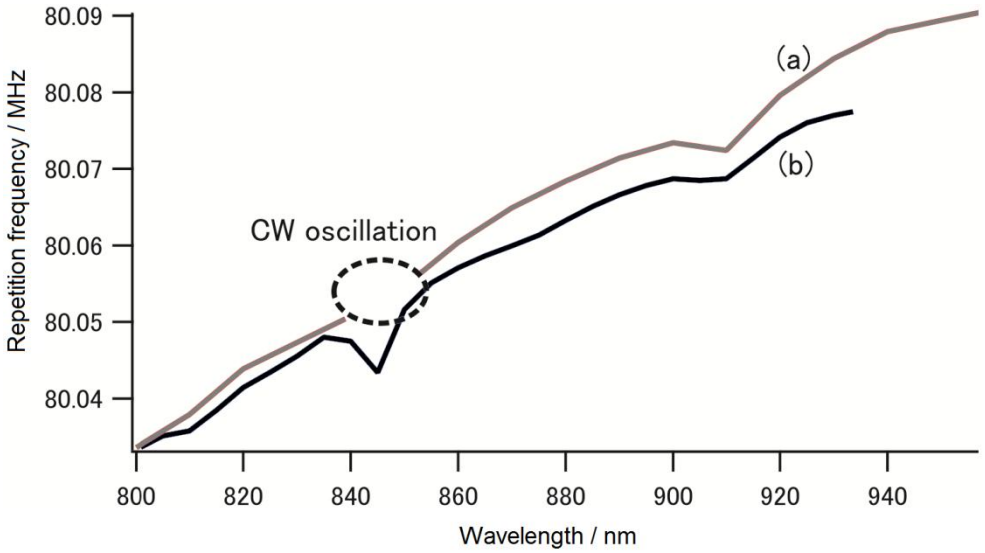

Figure 2.8. Relation between repetition frequency of the AOTF laser and output wavelength (a) without and (b) with SF-10 prism pair compensation.

2.3 Development of high-speed tunable laser system

2.3.1 Synchronization of two mode-locked lasers

The application of two independent picosecond mode-locked lasers for CRS microscopy is preferable to realize high spectral resolution since the spectral bandwidth of the pulse satisfy the requirement for typical resolution of vibrational microscopy. Both laser pulses in CRS microscopy must spatio-temporally overlap. To achieve spatial overlapping, one can adjust the beam pathways in the optical setup. The degree of temporal overlapping is determined by timing jitter during synchronization of both laser pulses. Reduction of timing jitter is very important for improving the signal-to-noise ratio of the CRS image.

Synchronization of two mode-locked lasers can be provided by a laser with controllable repetition frequency and another one with fixed repetition frequency as the reference. The controllable repetition frequency can be achieved if the laser cavity is controllable since the repetition frequency of a mode-locked laser depends on the cavity length. The end mirror

attached on a piezoelectric actuator is often used to control the laser cavity length due to capability of the piezoelectric actuator for fast response and high accuracy change (Fig. 2.9). However, as shown previously, the compensation value needed for the repetition frequency change of the laser during the wavelength scanning is around 43.9 kHz. This frequency change equals to 1100 μm laser cavity length change, while the piezoelectric actuator only has an operating range of few tens of μm, other compensation system is also needed to provide larger compensation value.

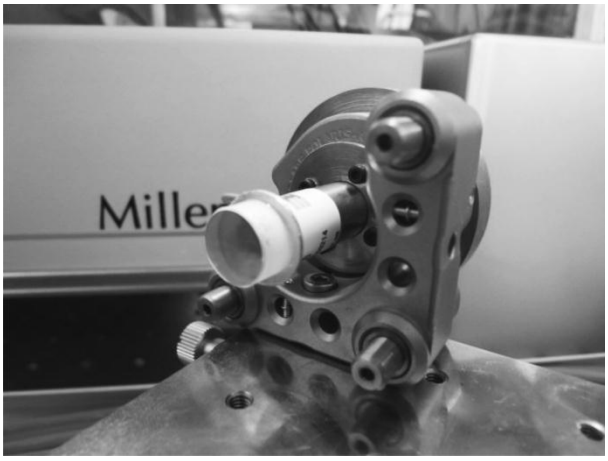

Figure 2.9. Photograph of the end mirror attached on the piezoelectric actuator for synchronization

To achieve larger compensation, I placed a pair of parallel plates from BK7 glass driven by galvanometer motors (Harmonic Drive Systems) inside the laser cavity. The parallel plates were made by cutting (Kiyohara Optics) the laser windows (W2-PW1-1940-C-670-1064-45P, CVI Melles Griot) to 12.0 mm × 4.3 mm × 10.0 mm (Fig. 2.10a). Each of plate was mounted on the galvanometer scanner (PSM-130 & plate holder, Harmonic Drive Systems). The parallel plates were rotated in opposite directions by the same angular increment, which was rapidly and precisely controlled by the galvanometer motors. The driver of the galvanometer scanner (LSA-20B-30, Harmonic Drive Systems) was equipped with water cooling system using a heatsink (P-100S, Takagi MFG. CO.) and a cooling water

circulator that is used for the AOTF crystal and the Ti:sapphire crystal in the laser (Fig. 2.10b). Theoretically, the galvanometer scanner system can cover a repetition frequency change of around 160 kHz on its full performance. The pair of the parallel plates driven by the galvanometer scanners were installed at 45° to minimize the reflection loss (Fig. 2.10c).

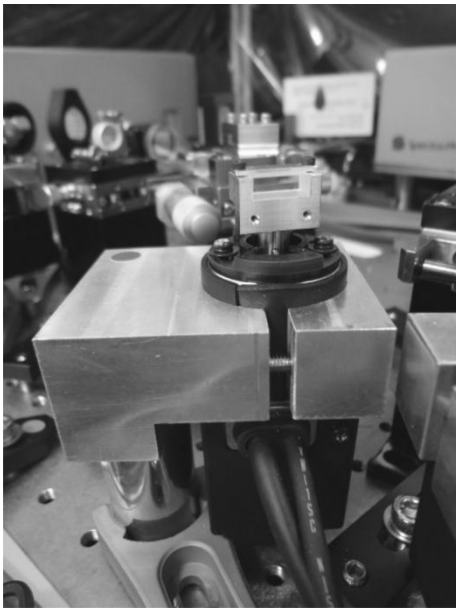

(a)

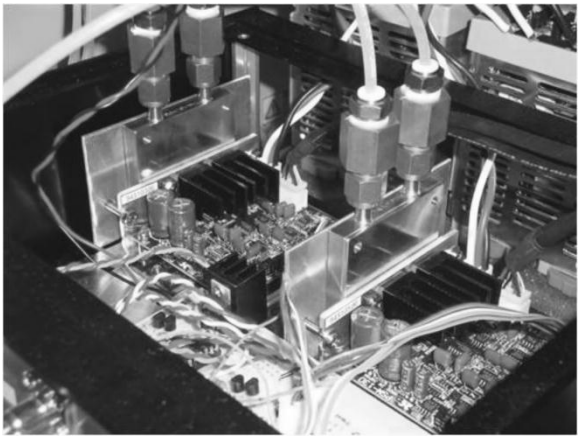

(b)

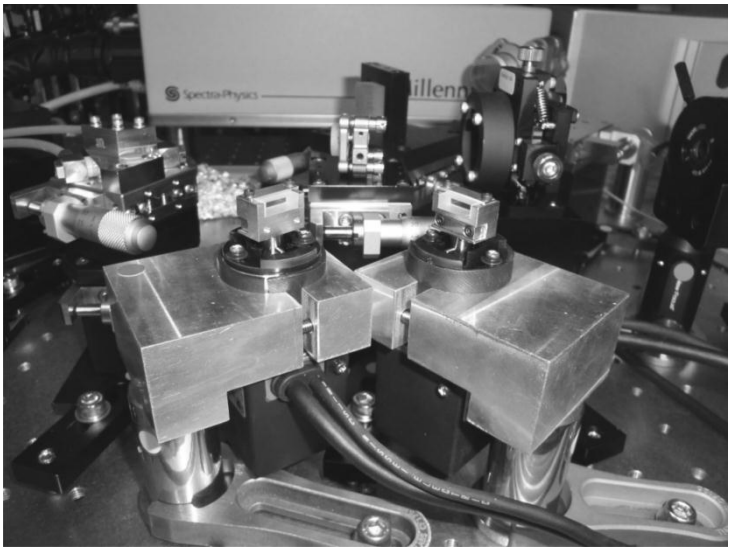

(c)

Figure 2.10. (a) Photograph of one of the parallel plates mounted on the galvanometer scanner. (b) Photograph of galvanometer scanner controllers with water heatsinks. (c) Photograph of the parallel plates pair mounted on the galvanometer scanner installed in the laser cavity

The combination of the end mirror attached on the piezoelectric actuator and the pair of parallel plates mounted on the galvanometer scanners allowed repetition frequency compensation of 65 kHz, which is enough to compensate the repetition frequency difference of 44 kHz from 800 to 930 nm. This configuration led to the power loss by the value of 20% at 845 nm (decrease from 400 mW to 320 mW). However, by optimizing the intensities of RFs to the AOTF, this power loss was negligible.

2.3.2 Pulse synchronization system

The timing jitter detection system and the phase-locked loop system for controlling the movements of piezoelectric actuator and galvanometer scanners should be separated to avoid the competition against each other to achieve the synchronization and reduction of the timing jitter. The repetition frequency of the laser by the value about 80 MHz requires the sensitivity of detection range around 12.5 ns. To obtain the high signal-to-noise ratio CRS images, the timing jitter should be reduced to femtosecond order while capability of timing jitter detection at femtosecond order is obligated. It is difficult to satisfy both needs using one timing jitter detection system. Therefore, I employed two types of timing-jitter detection systems: an electronic phase detector for coarse control at picosecond order and a balanced cross-correlator for fine control at femtosecond order [78].

2.3.2.1 Timing jitter detection at picosecond order

The timing jitter detection for coarse control of synchronization at picosecond order using electronic phase detector is described in Fig. 2.11a. The system consists of two PIN photodiode detectors (S5973, Hamamatsu Photonics), low-pass filters (98 MHz bandwidth,

BLP-100+, Mini-Circuits), an electronic phase detector (2.11b), a differential amplifier with controllable gain (CA-406L2, NF Corporation) (Fig. 2.11c) and a RC low-pass filter (5 kHz, R = 300 Ω, C = 0.1 μF). Portions of two pulsed laser beams from the lasers are introduced into the PIN photodiodes, and the optical pulses were converted to electric pulses. The converted signals are amplified and are fed to the electronic phase detector through electronic low-pass filters of which bandwidth is 98 MHz. The electronic phase detector consists of dual high speed ECL comparators (ADCMP563BRQ, Analog Devices) and phase/frequency discriminator (AD9901KQ, Analog Devices). The DC voltage output from the electronic phase detector corresponds to the phase difference of the two input signals derived from the two laser pulses. Therefore, the phase difference represents the time interval of two laser pulses. The electronic phase detector works as a frequency comparator for the detection of the difference over one cycle.

The detectable range of the phase detector was evaluated using two sinusoidal waves (30MHz, $1V_{p-p}$) which have small frequency difference generated by function synthesizer (WF1974, NF). As shown in Fig. 2.12a, the phase difference between the two pulses can be detected over 340 degrees. It indicates that the detectable range of a time interval between two laser pulses at repetition frequency of 80 MHz is 11.8 ns. However, instead of the full range detection of the phase difference, the narrow range is preferable for reducing the electric noise and increasing the voltage-to-phase sensitivity. For that purpose, the phase detector signal is amplified by 50 times and the detectable range is 20 degree. The gradient of the phase difference is 1.04 V/degree (Fig. 2.12b) which corresponds to 33.4 ps/V for repetition frequency of 80 MHz. The noise of phase detector is 32 mV at 5 kHz bandwidth which indicates that the phase sensitivity of the system with 5 kHz bandwidth is 0.031 degree which corresponds to 1.05 ps for repetition frequency of 80 MHz.

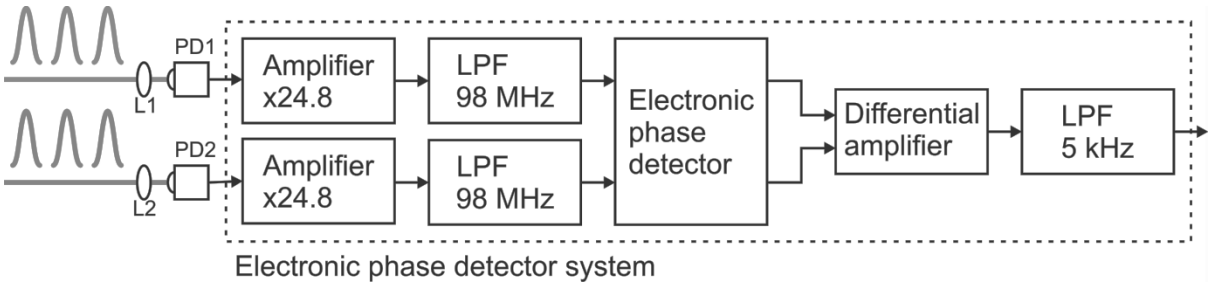

(a)

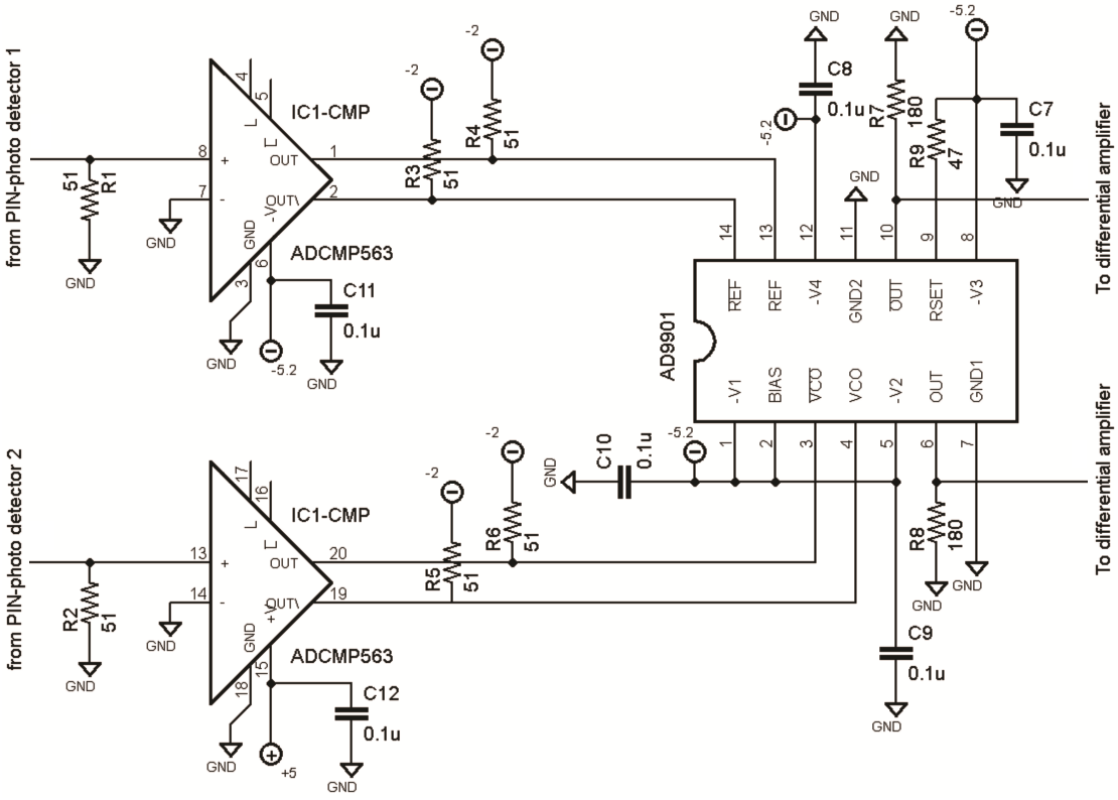

(b)

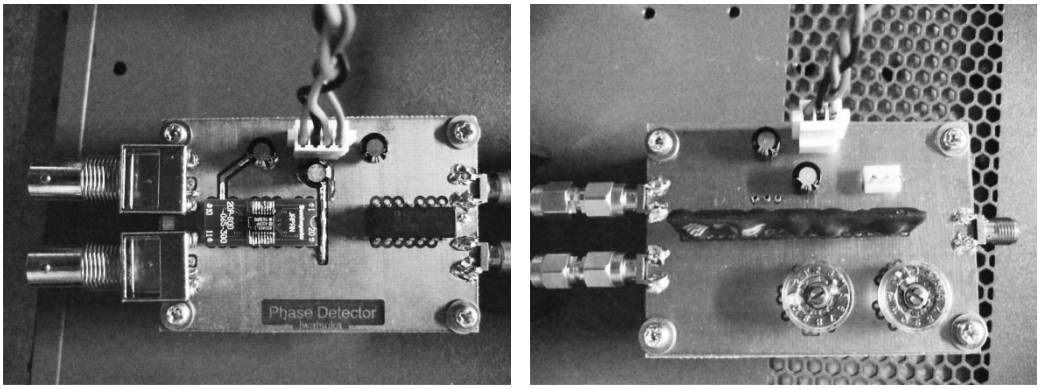

(c) (d)

Figure 2.11. (a) Schematic of the electronic phase detector system. (b) The electronic circuit of the electronic phase detector. The photographes of (c) phase detector and (d) differential amplifier circuits.

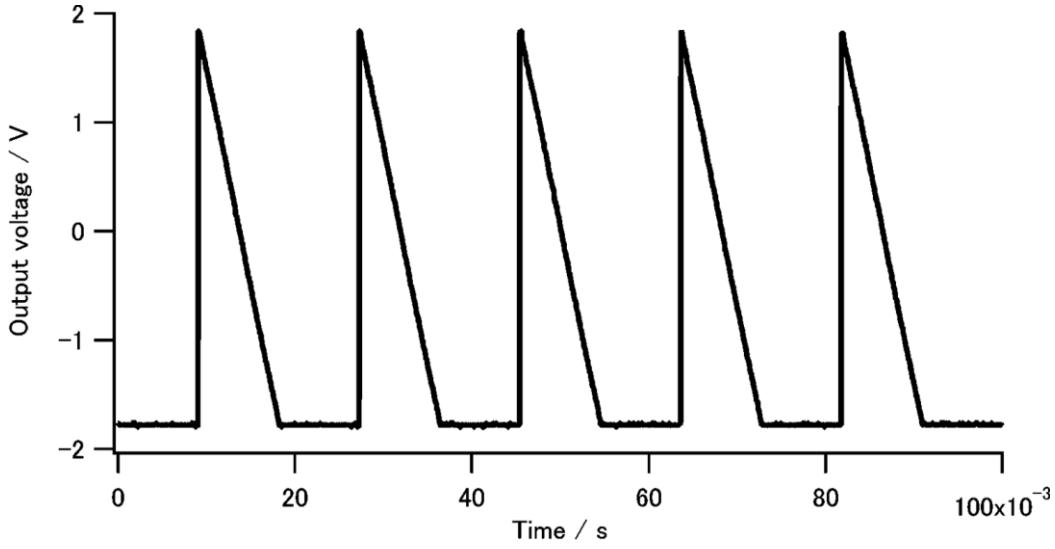

(a)

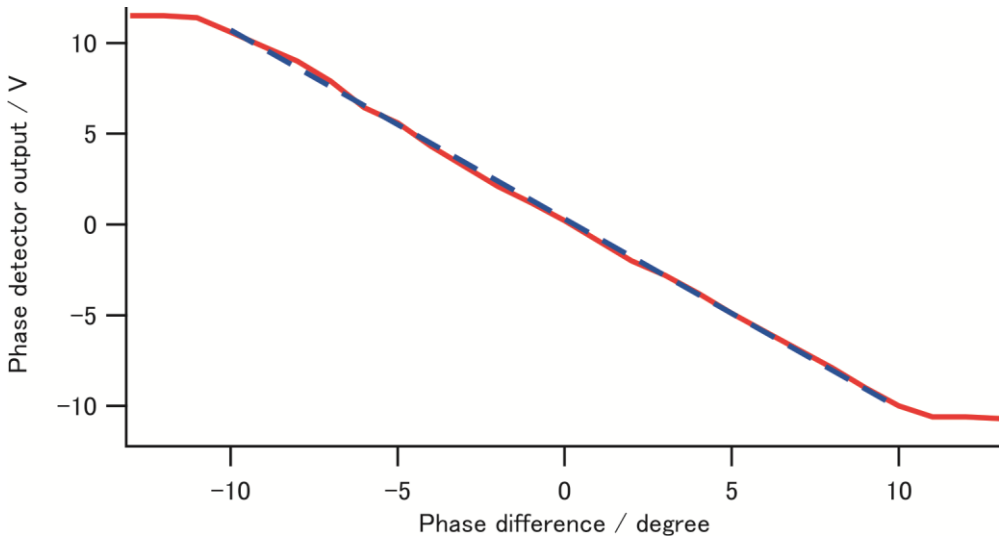

(b)

Figure 2.12. (a) Phase detector signal with two input sine wave (30MHz, 1 V_{pp}) which have small frequency difference. The phase difference of two pulse can be detected over 340 degrees. (b) Blue = output voltage of the phase detector given by data sheet. Red = amplified output voltage of the phase detector from measurement. The gain of the differential amplifier was set at ×50. The input signals generated by a function synthesizer were set at 30 MHz, sine wave, and 1 Vp−p. The gradient was 1.04 V / degree. Assuming that repetition frequency of the laser is 80 MHz (repetition rate of 12.5ns), this corresponds to 33.4 ps/V. The noise of phase detector was 66 mV at 100 kHz bandwidth. So, the phase sensitivity of the system with 100 kHz bandwidth was 0.063 degrees, which corresponds to 2.2 ps for 80 MHz.

2.3.2.2 Timing jitter detection at femtosecond order

A balanced cross-correlator is used as the timing jitter detection for fine control of synchronization at femtosecond order [78]. The developed balanced cross-correlator (Fig. 2.13a, Fig. 2.13b) consists of two cross-correlators (CC1, CC2) and a differential amplifier (CA-406L2, NF Corporation). Each of the cross correlators consists of a dichroic mirror (DM1: Short-wavelength-pass filter 800 nm, 3RD800SP, Omega Optical, DM2: Long-wavelength-pass filter 800 nm, 3RD800LP, Omega Optical), a high reflective mirror (M1/M2, Au coated mirror, Thorlab), a lens (L1/L2, NA 0.4, x20, S72C-20, Suruga Seiki), and a two-photon absorption detector (TPD1/TPD2, G1115, Hamamatsu).

The cross-correlation signal is obtained from a two-photon absorption detector (TPD) which detects a portion of collinearly overlapped pulse beams from two lasers reflected by a pair of dichroic mirror and high reflective mirror (Fig 2.13c, Fig. 2.13d). One of the overlapped beams is reflected by the dichroic mirror, and the other is reflected by the high reflective mirror. Therefore, a fixed time delay between two beams is given by this mirrors pair and it is adjustable by changing the distance between the mirrors. Different configuration of mirrors pair on each cross-correlator induced the delays to ω_1 beam in CC1 and ω_2 beam CC2. Therefore, the detected signals by TPD1 and TPD2 are given by:

$$S_{TPD1} = \int |g_1(t)|^2\, dt + \int |g_2(t)|^2\, dt + \int g_1(t-\Delta t)\, g_2(t-\tau)\, dt, \qquad (2.1a)$$

$$S_{TPD2} = \int |g_1(t)|^2\, dt + \int |g_2(t)|^2\, dt + \int g_1(t)\, g_2(t-\Delta t-\tau)\, dt, \qquad (2.1b)$$

where $g_1(t)$ and $g_2(t)$ are the amplitude function of pulse beams with Gaussian profile, Δt is the fixed delay by mirror pairs which is assumed to be at the same value in CC1 and CC2, τ denotes the timing jitter. A GaAsP photodetector is used as the TPD since it has a sensitivity to detect wavelength less than 680 nm, so that the Ti:sapphire laser beam (700 – 950 nm)

should not be responded by the detector.The balanced cross-correlator signal is then obtained from the difference between CC1 and CC2 using a differential amplifier.

$$S_{Diff} = S_{TPD1} - S_{TPD2}$$
$$= \int g_1(t-\Delta t)\, g_2(t-\tau)\, dt - \int g_1(t)\, g_2(t-\Delta t-\tau)\, dt, \qquad (2.2)$$

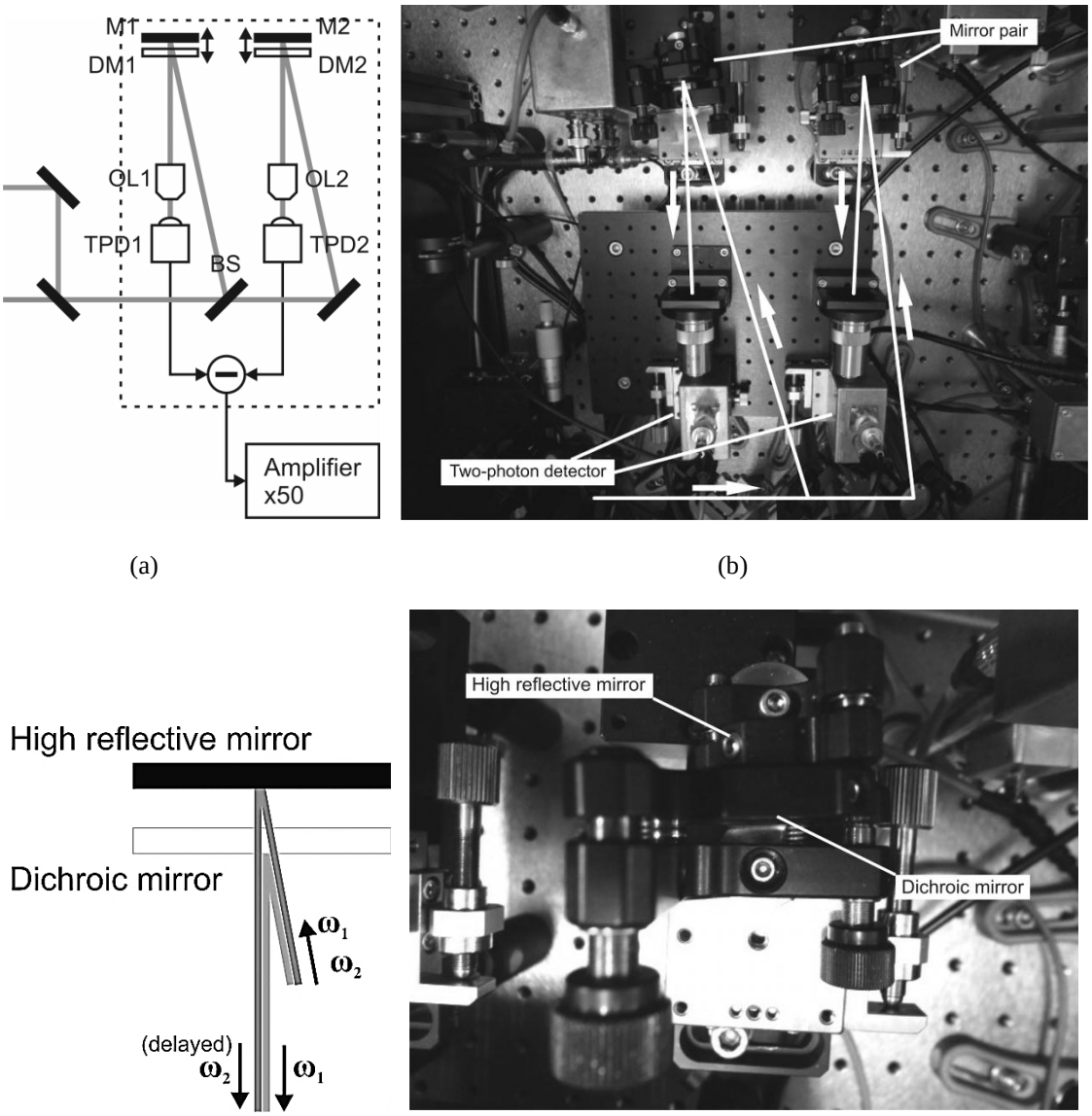

Figure 2.13. (a) Schematic and (b) photograph of balanced cross-correlator system. (c) The pair of dichroic mirror and high reflective mirror induced the time delay to one of the overlapped beams (in this case, the ω_2 beam). (d) Photograph of the dichroic mirror and high reflective mirror pair.

If the timing jitter τ is small enough, S_{Diff} will be balanced (Fig.2.14a). When the timing jitter delays ω2 beam ($\tau > 0$), S_{TPD1} becomes larger and S_{TPD2} become smaller, so that S_{Diff} has a positive value (Fig.2.14b). On similar behavior, when ω2 beam is in advanced ($\tau < 0$), S_{Diff} has a negative value. Therefore, the sign of S_{Diff} represents whether either beam is delayed or both are balanced, and the amplitude of S_{Diff} represents the length of delay (Fig. 2.14c).

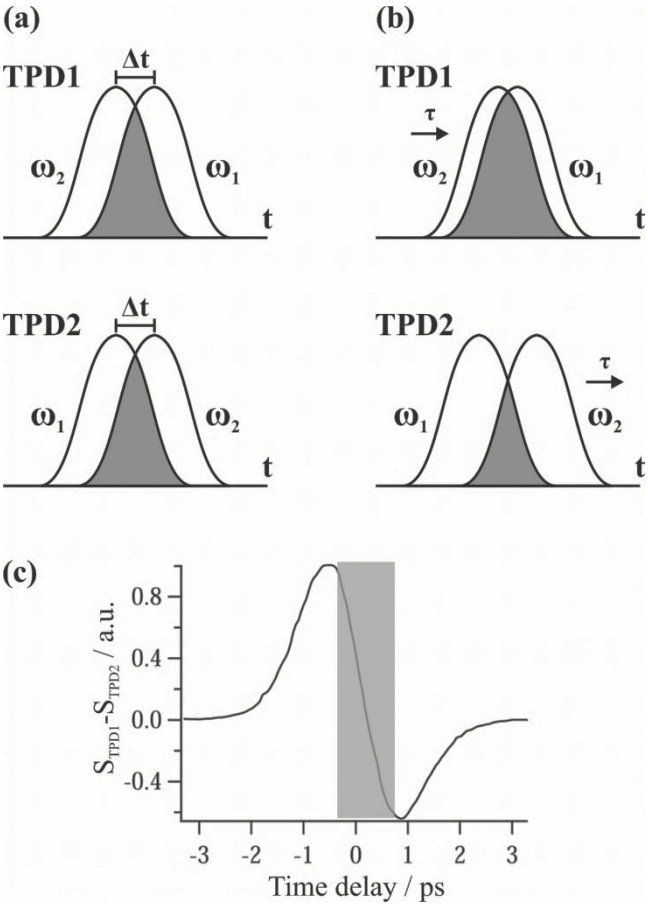

Figure 2.14. (a) Cross-correlation signal of overlapped pulses from two beams without timing jitter. When the timing jitter τ between two lasers (ω_1, ω_2) is negligible, the signal from TPD1 and TPD2 is balanced so that the difference is equal to zero. (b) Cross-correlation signal of overlapped pulses from two beams with timing jitter. When the timing jitter affects ω_2 to delay, the cross-correlation signal of TPD2 is bigger and the signal of TPD2 is smaller. (c) Balanced cross-correlation signal by scanning delay of the one of the lasers.

2.3.2.3 Synchronization control using electronic phase detector and balanced cross-correlator

Figure 2.15 shows the developed phase lock loop (PLL) control system for synchronization of the AOTF laser and another Ti:sapphire laser with fixed repetition frequency. The main parts of the synchronization control system are two picosecond mode-locked lasers, two types of timing jitter detection system (phase detector and the balanced cross-correlator), a digital signal processor (DSP, C6713DSK, Texas Instruments) with A/D-D/A (8 channels-4 channels) interfaces (DSK6713IFA, Hiratsuka Engineering), an analog proportional-integral-differential (PID) controller (T-PID01Z, Turtle Industry), the personal computer PC1, a piezoelectric controller (MDT694A, Thorlabs), a galvanometer scanner controller (Harmonic Drive Systems), an AOTF controller, a piezoelectric actuator driving the end mirror, galvano scanners driving parallel plates, and the AOTF.

The output from the electronic phase detector represented picosecond-order temporal differences between the two laser pulses. This signal was fed back to the galvanometer motors via the DSP controller to rotate the pair of parallel plates to compensate for variations in the repetition frequency caused by wavelength scanning and to synchronize both lasers. The output from the balanced cross-correlator was fed back to the piezoelectric actuator via the PID controller and to the galvanometer motors.

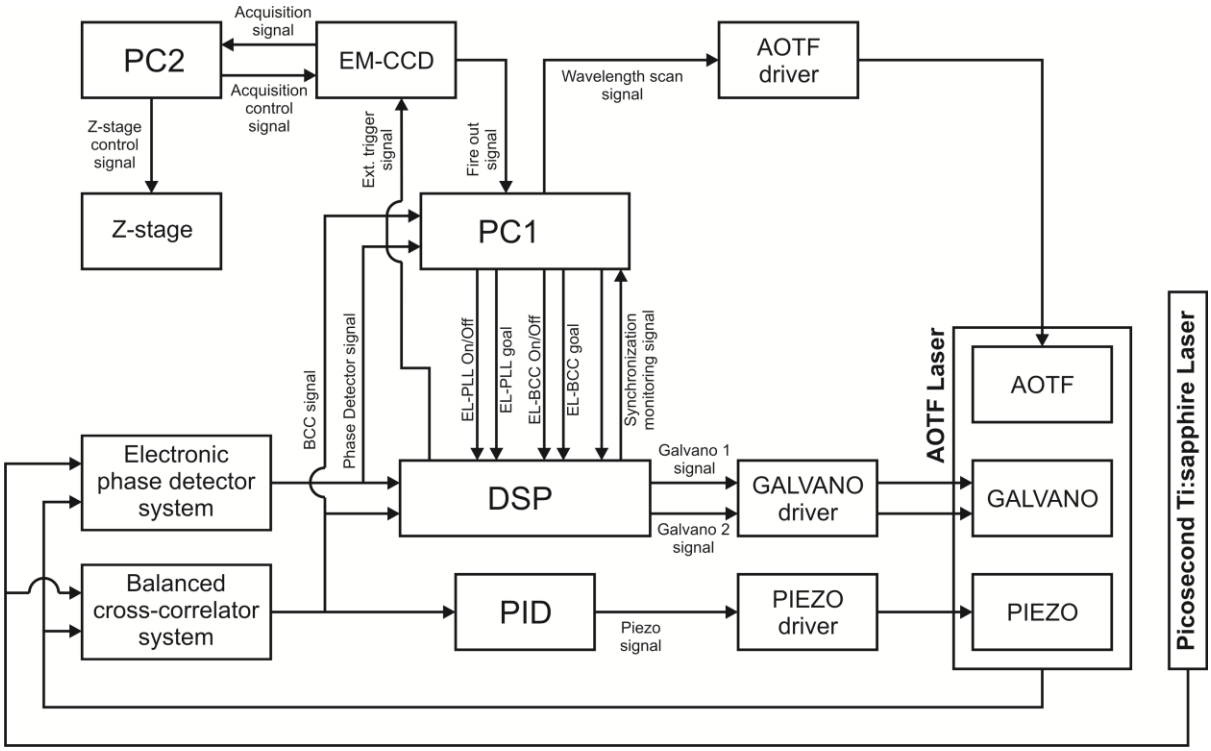

Figure 2.15. Schematic of total developed control system. PC1 controls the wavelength scan timing via wavelength scan signal to AOTF driver that related to the timing for DSP to send the external trigger to EM-CCD and also controls the PLL control system via DSP. Synchronization is controlled by PLL mechanism using galvano motors driving parallel plates (GALVANO) and piezoelectric actuator driving end mirror (PIEZO). The output signal from electronic phase detector was fed back to the galvano motors via the DSP controller, whereas that from BCC controller was fed back to galvano motors via DSP and to piezoelectric actuator via PID controller.

The timing jitter during synchronization using the electronic phase detector shown in Fig. 2.16 is calculated by the value of 12 ps. This timing jitter should be reduced to a few of picosecond or smaller to enable CRS imaging. The lack of resolution on the DSP may contribute to the occurrence of large timing jitter since the significantly large noise of DSP output (2.81 mV) interferes with the needed voltage (5.3 mV) to change the repetition frequency of 1 Hz using the piezoelectric actuator. The insufficient operating frequency range should also be considered and it may be solved by changing the piezoelectric actuator to the smaller size. The timing jitter in Fig. 2.17 shows the sequence of synchronization which is

started by the coarse control using galvanometer scanners (timing jitter is reduced to 8.7 ps with the bandwidth of 5 kHz) and then followed by the fine control using piezoelectric actuator (timing jitter is reduced to 1.6 ps with the bandwidth of 5 kHz).

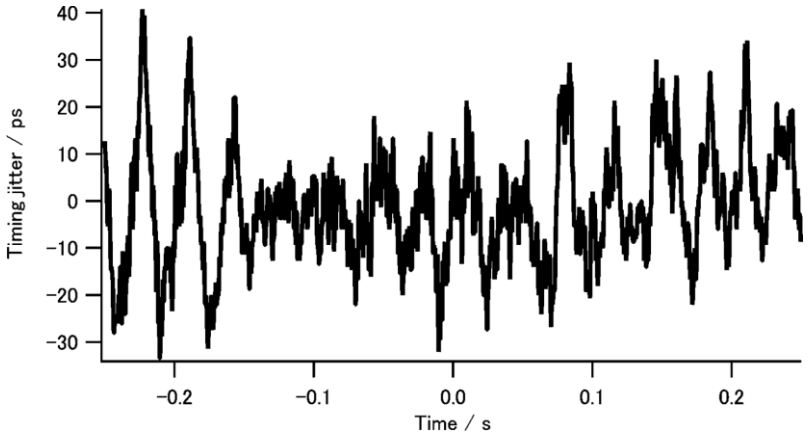

Figure 2.16. Phase detector signal while synchronizing the AOTF laser with the repetition frequency fixed Ti:S laser using the end mirror attached on the piezoelectric actuator (840.30, 45μm, PI)

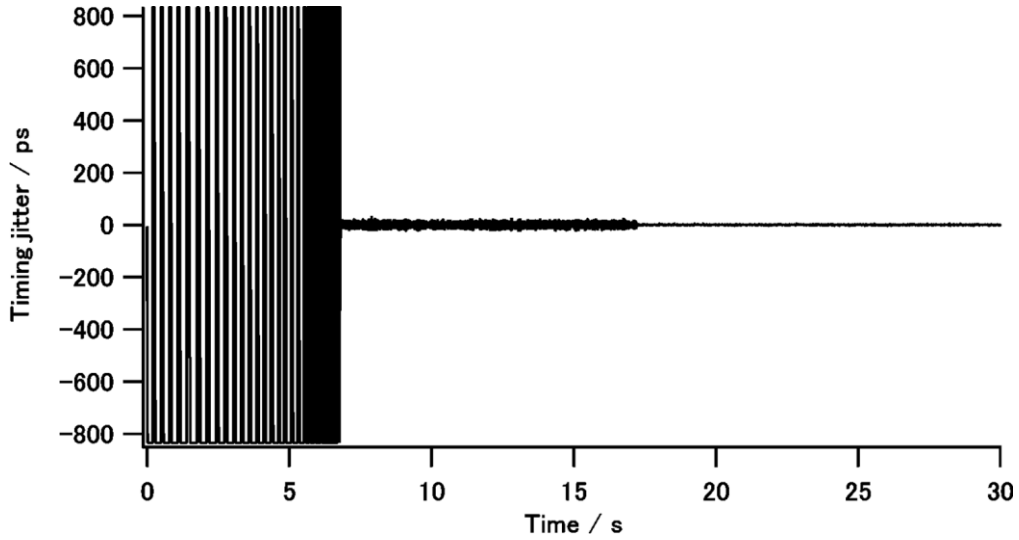

Figure 2.17. Behavior of the phase detector signal while synchronizing using the parallel plates pair mounted on galvanometer scanner and the end mirror attached on the piezoelectric actuator (840.10, 15μm, PI). Controlling using the parallel plates pair mounted on the galvanometer scanner, the timing jitter was reduced to 8.7 ps. Added controlling using the end mirror piezoelectric actuator, the timing jitter was reduced to 1.6 ps.

After adjusting the timing jitter to the sensitive region of the balanced cross-correlator, the PLL control using electronic phase detector was switched to the balanced cross-correlator. Figure 2.18 (top & bottom) shows timing jitter observed from the balanced cross-correlator output with 5 kHz bandwidth (top), and 150 Hz bandwidth (bottom). First, the lasers were synchronized with the electronic PLL control, and then the control system was switched to the feedback loop of the balanced cross-correlator after about 12 s. The output voltage from the balanced cross-correlator was converted to timing jitter by assuming that maximum/minimum voltage of +/- 6 V is equal to time difference of 5 ps from the pulse width. The standard deviation of the timing jitter before applying the feed-back loop of the balanced cross-correlator was about 1.6 ps, and it was reduced to 845 fs (5 kHz) and 538 fs (150 Hz).

The timing jitter during the wavelength scanning was also observed using the phase detector signal. First, the lasers were synchronized with the electronic PLL control with galvano and piezo actuator with timing jitter of 1.6 ps. Then the piezo actuator control was stopped and the wavelength was scanned with the increment of 0.1 nm. After scanning, the piezo actuator control was once again started and the timing jitter was reduced to 1.6 ps. The time required for every wavelength change sequence is 23 ms (Figure 2.19).

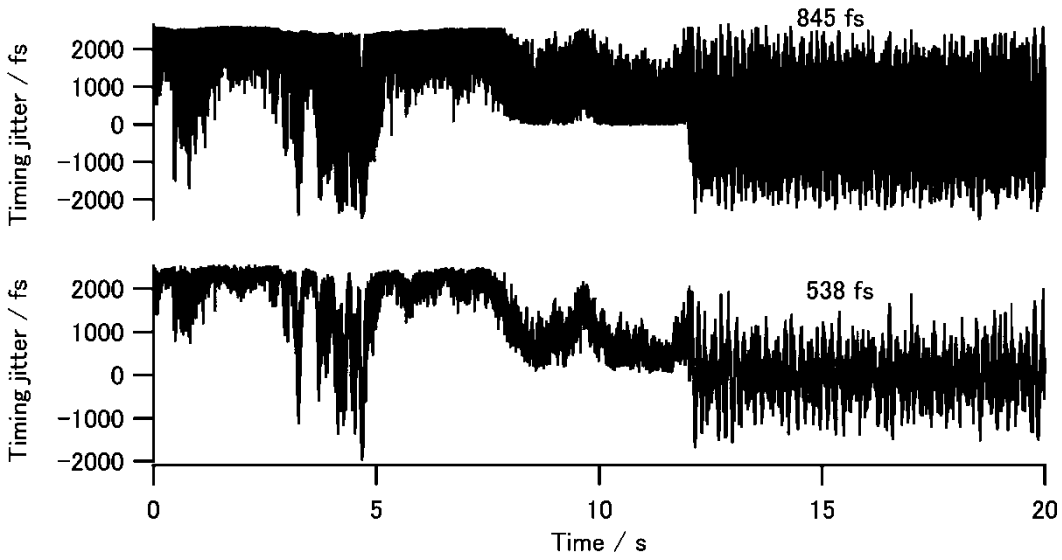

Figure 2.18. Timing jitter signal observed from the balanced cross-correlator output with 5 kHz bandwidth (top), and 150 Hz bandwidth (bottom). The timing jitter before applying the feed-back loop of the balanced cross-correlator was about 1.6 ps, and it was reduced to 845 fs (5 kHz) and 538 fs (150 Hz) after applying the feed-back loop of the balanced cross-correlator.

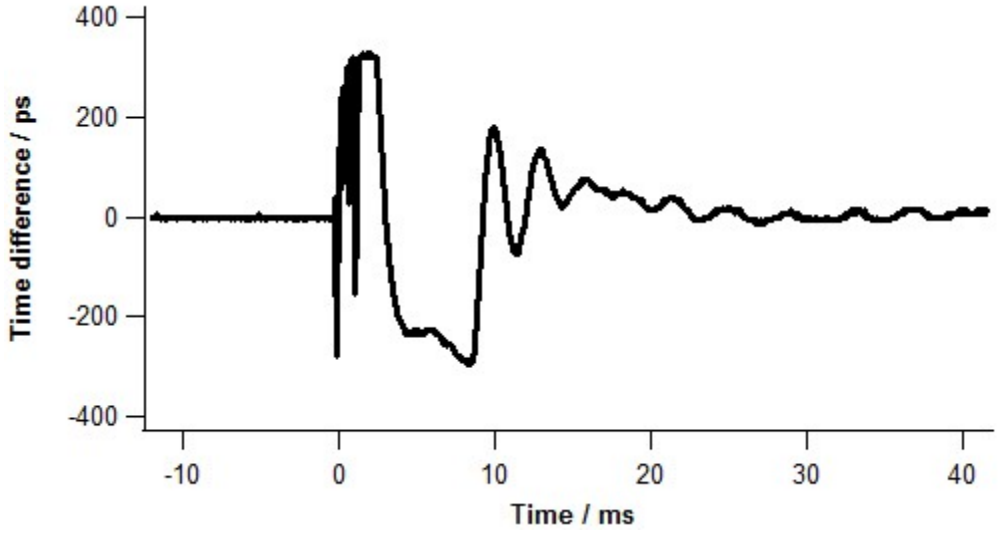

Figure 2.19. Timing jitter observed from the phase detector output while scanning the wavelength during PLL control. The timing jitter was 1.6 ps and thescanning time was 23 ms for every wavelength change with the increment of 0.1 nm.

2.4 Improvement of stability on pulse synchronization system

2.4.1 Electronic phase detector with autogain amplifier

The electronic phase detector output depended on the time difference and amplitudes of the two input pulses. It always considers the voltage information from the photodetectors as the phase of the detected pulse. The difference of the signals from both photodetectors is understood at the time difference of the pulses from two laser sources. Then, the output of the electronic phase detector will determine the behavior of synchronization at the picosecond order. Therefore, it is important to keep the stability of the signal from each photodetector before it is delivered to the electronic phase detector. I introduced an autogain amplifier (AD8368, Analog Devices) after each photodetector (Fig. 2.20) to keep the amplitudes stable. The autogain amplifier generated a 224 mV rms electrical output signal for any photodetector signal with amplitude larger than 63 mV rms.

2.4.2 Balanced cross-correlator with polarizing beam splitter

The output from the balanced cross-correlator obtained by optical detection was used for fine control of synchronization because it could detect the femtosecond-order temporal differences between the two laser pulses. The key point of balanced cross-correlator operation is the balanced between each cross-correlator which depends on the each beam. As it has been explained that the difference of the signal detected by TPD1 and TPD2 will equal to zero if the timing jitter is small enough and it is said that the two cross-correlators system are balanced. The non-zero value of the difference represents the delay occurs on one of the pulses due to the significant timing jitter. Therefore, it was necessary to conserve equal

separation of the pump and Stokes pulses to the two TPD to avoid misinterpretation by the balanced cross-correlator which cause the distortion to the synchronization behavior. As shown in Fig. 2.21, a polarizing beam splitter (PBS052, Thorlabs) together with two achromatic half wave plates (AHWP05M-980, Thorlabs) enabled us to easily control and maintain the balance of the transmitted and reflected intensities of the incident pulses, so that the balanced cross-correlator could minimize the timing jitter properly.

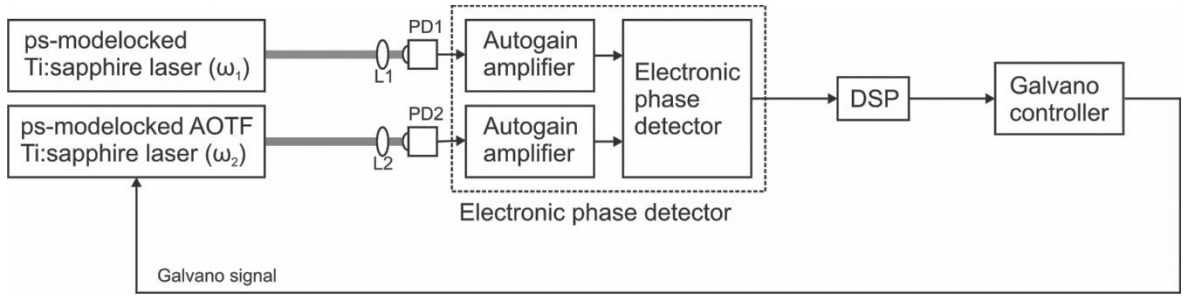

(a)

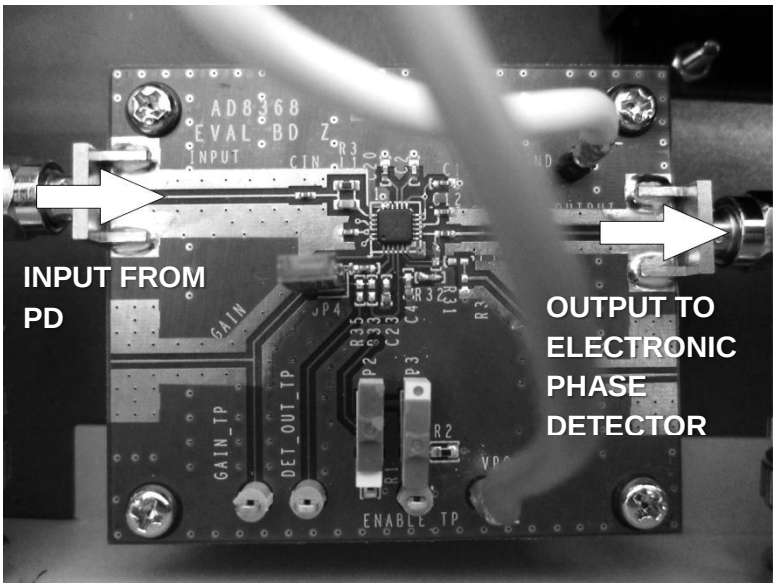

(b)

Figure 2.20. (a) Electronic phase detector with autogain amplifier. PD1, PD2 = photodetectors; L1, L2 = lenses. (b) The photograph of the autogain amplifier circuit (AD8368, Analog Devices). Left arrow = input. Right arrow = output.

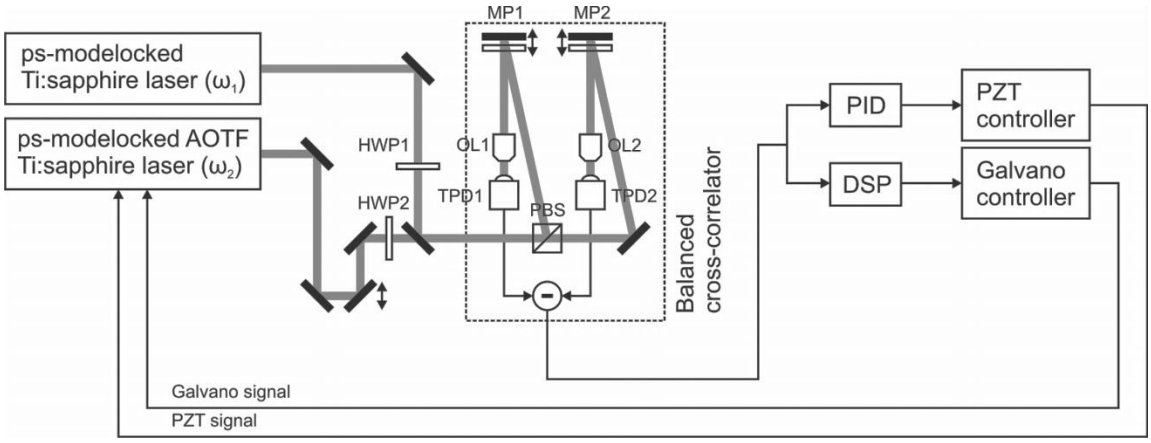

(a)

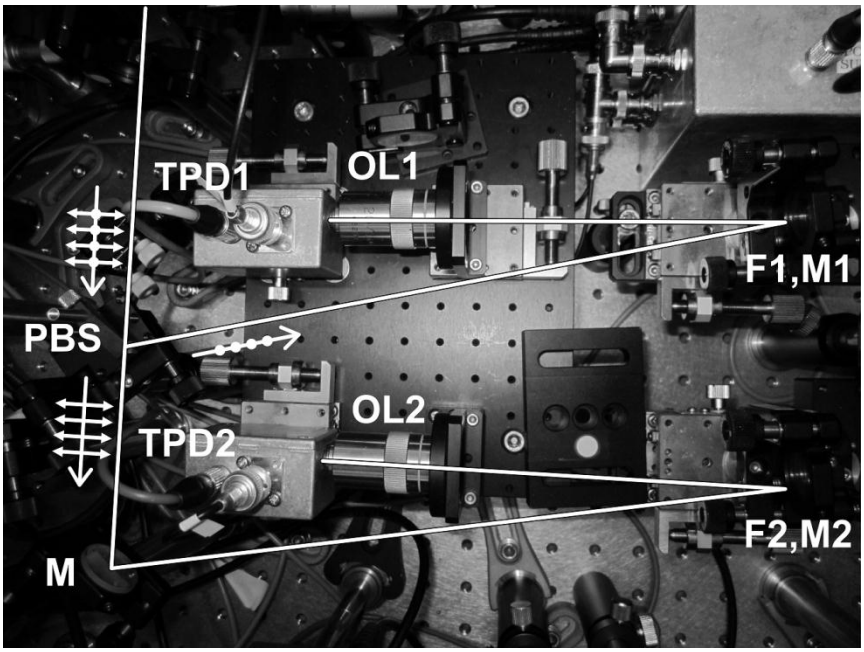

(b)

Figure 2.21. (a) Balanced cross-correlator with polarizing beam splitter and half wave plates. PBS = polarizing beam splitter; HWP1, HWP2 = half wave plates; TPD1, TPD2 = two-photon detectors; OL1, OL2 = objective lenses; MP1, MP2 = pair of dichroic mirror and highly reflective mirror. (b) Photograph of balanced cross-correlator with polarizing beam splitter and half wave plates (half wave plates do not appear here). Pairs of dichroic mirror (F1, F2) and highly reflective mirror (M1, M2) are equal to MP1 and MP2 in a. M = mirror. Yellow arrows show the separation of indicent light to PBS into two equal polarization components. This equal separation is determined by the adjustment of HWP1 and HWP2.

2.5 Summary

The development of high-speed tunable picosecond laser was enabled by introduction of electronically wavelength scanning system using the AOTF without any involvement of mechanical action. To synchronize with another picosecond laser, the synchronization system includes two types of timing jitter detection system: the electronic phase detector and the balanced cross-correlator. Both timing jitter detection systems were used for feedback control with phase-locked loop mechanism. The control signals are applied to the piezoelectric actuator where the end mirror attached on and the galvanometer scanners where the pair of parallel plates mounted on. The end mirror attached on the piezoelectric actuator and the pair of parallel plates mounted on the galvanometer motors were introduced to compensate for the repetition frequency change during the wavelength scanning, so that the synchronization could be maintained. For the stability improvement of the timing jitter detection system, an autogain amplifier was placed after each detector in the electronic phase detector. A polarizing beam splitter together with two achromatic half wave plates were also placed in the optical path of balanced cross-correlator to easily control and maintain the balance of the transmitted and reflected intensities of the incident pulses.

Chapter 3
Fast spectral CARS microscopy system

3.1 Introduction

CARS microscopy provides a label-free imaging for biological application with high molecular sensitivity. The intensity of CARS signal is much stronger than that of spontaneous Raman signal because the generated CARS radiation occurred as the result of constructive interference in the excitation volume. With sufficiently strong signal, CARS microscopy offers a possibility for fast acquisition imaging with additional advantage of 3-D sectioning capability [14]. It was reported that image acquisition at video rates has been achieved using CARS microscopy by employing a scanner system consisting of a polygon mirror and a galvanometer mirror [25]. This acquisition rates can satisfy the need of temporal sensitivity for biological study. Though it is still unclear, some analysis and observation tools in biological application have sensitivity of the order of several seconds to minutes [79-83]. The real biological processes may occur faster, and therefore, faster acquisition rates will be an advantageous.

In CARS microscopy, the incident beams can only excite a specific molecular vibration that matches to the frequency difference of the incident beams. In order to obtain spectral information, one of the laser sources should be tunable while the other one should maintain the wavelength to scan of the frequency difference. For that purpose, the tunable laser should have high spectral resolution yet wide-range tunability. The laser should also have a fast tuning ability while providing sufficient, stable power. A picosecond mode-locked laser meets the requirements of the laser for CARS microscopy. Therefore, I decided to develop a

CARS microscopy system using two picosecond mode-locked lasers which one of them is the picosecond AOTF mode-locked laser. The picosecond AOTF mode-locked laser has a high-speed wavelength tuning capability to enable spectral imaging.

CARS microscopy also demands a spatial point-by-point scanning to attain the image over certain area. The rapid point-by-point scanning using mirror system shortens the dwell time at each scanning point. Consequently, for generating desired CARS signal, it requires excitation beams with sufficiently high intensities which may induce a photo-damage effect on the sample [84-86]. The application of microlens array scanner for multi-focus imaging enables the high-speed image acquisition with less risk of sample disruption [79-82].

3.2 Fast spectral CARS microscopy system using microlens array scanner and high-speed tunable picosecond laser

3.2.1 Optical setup

The optical setup of the developed fast wavelength scanning CARS spectromicroscopy system using picosecond AOTF laser is shown in Fig. 3.1. The system consists of picosecond modelocked Ti:sapphire laser (pulse duration = 5 ps, repetition rate = 80 MHz, Tsunami, Spectra-Physics) and picosecond AOTF mode-locked Ti:sapphire laser (pulse duration <20 ps, repetition rate = 80 MHz, Megaopt) operating at different wavelengths, a high-precision pulse synchronization system, a microlens array scanner (lens diameter = 0.58 mm, focal length = 11.6 mm, MLA1-DD, Nanophoton), a modified inverted microscope (Ti-U, Nikon), and an electron-multiplying charge-coupled device camera (EM-CCD, DV-897, Andor). The two lasers were synchronized temporally by phase-locked loop (PLL) control using the synchronization system developed. These synchronized laser beams were spatially

overlapped and were directed to the microlens array scanner to split them into multiple beamlets. The beamlets were collimated with relay lenses and were focused to multiple spots on the specimen with an objective lens (CFI Plan Apo IR, x60, NA = 1.27, WI, Nikon). The system produced 7 focal spots on the specimen from laser beams 2 mm. CARS signals from the multiple focal spots on the specimen were collected by another objective lens (NIR Apo, x60, NA = 1.0, WI, Nikon), and the fundamental signals were cut with optical filters. The CARS signals were observed in parallel with the EMCCD camera, and a CARS image was obtained by rotating the microlens array disc at angular speed up to around 5000 rpm.

The fast spectral CARS imaging was obtained by scanning the wavelength of the ω_2 light. The system covers the Raman spectral range from 400 cm^{-1} to 2260 cm^{-1} with a pump beam at 775 nm, and from 1600 cm^{-1} to 3470 cm^{-1} with a pump beam at 709 nm.

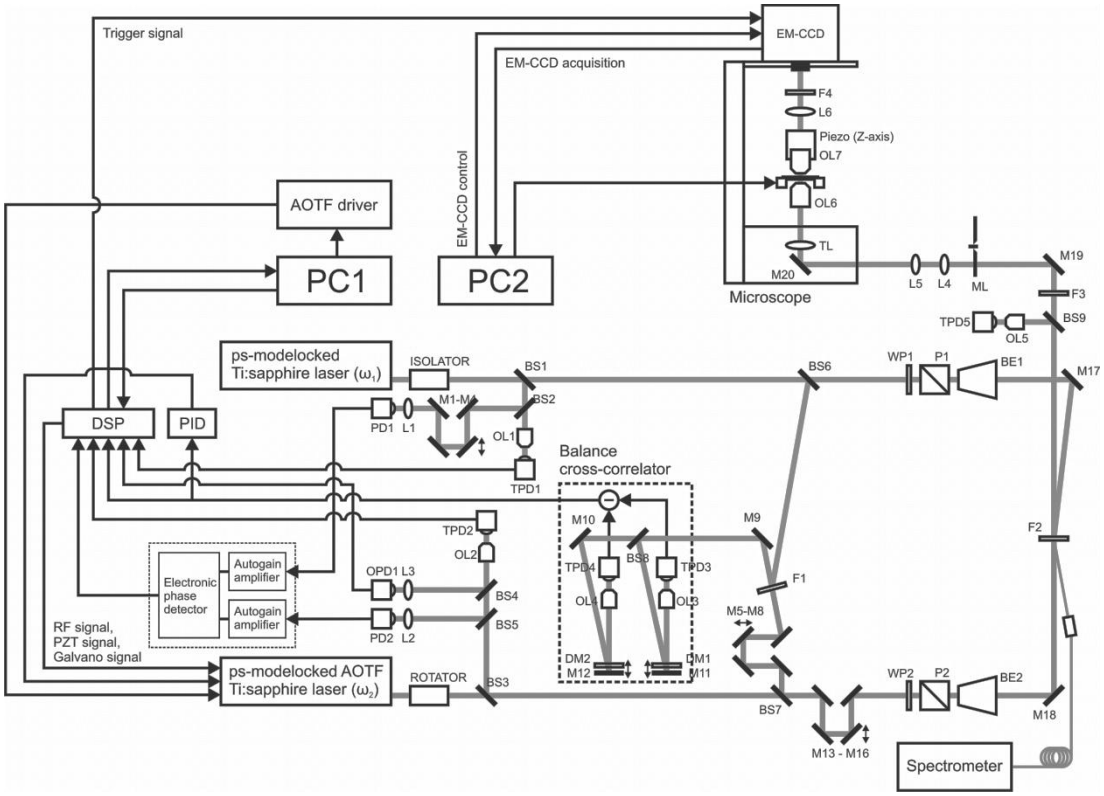

Figure 3.1. Optical setup of fast spectral CARS microscopy system: isolator, Faraday isolator; rotator, Faraday rotator (BB9-5R, EOT); M1-10, M13-19, dielectric multilayer mirror; M11, 12, Au-coated mirror (PF05-03-M01, Thorlabs); BS4, BS8, beam splitter (FABS-790-45-PW-1006-UV, CVI Melles Griot.); BS1-3, 5-7, 9, beam sampler (BSP10-B, Thorlabs); F1, 6, 785 nm edge filter (LP02-785RU, Semrock); F2, 800 nm short pass filter (3RD800SP, Omega); F3, 800 nm long pass filter (3RD800LP, Omega); F4, 780 nm laser line filter (LL01-780-12.5, Semrock); F5, 700 nm long pass filter (3RD700LP, Omega); F6, combination of notch filter (785 nm, NF01-785U-25, Semrock), band-pass filter (650–760 nm, 3RD650-760, Omega), short pass filter (770 nm, 3RD760SP, Omega) for detection in the Raman shift of 500–2000 cm^{-1}; or long pass filter (710 nm, Sigma Koki), band pass filter (560–640 nm, 3RD560-640, Omega), short pass filter (760 nm, 3RD760SP, Omega) for detection in the Raman shift of 2000–3500 cm^{-1}; OL1, 2, 5, objective lens (NA 0.25, x10); OL3, 4, objective lens (NA 0.4, x20, S72C-20, Suruga Seiki); OL6, objective lens (CFI Plan Apo IR, x60, NA = 1.27, WI, Nikon); OL7, objective lens (NIR Apo, x60, NA = 1.0, WI, Nikon); L1-3, plano-convex lens (f35 mm, f50 mm, f30 mm); L4, 5, achromatic lens (f50 mm, AC254-050-B, Thorlabs); PD1, 2, Si PIN-photodiode; TPD1-5, GaAsP photodiode; OPD1, Si photodiode (S2386-18K, Hamamatsu Photonics); WP1, Achromatic half-wave plate (WPA1312-λ/2-700-1000, Casix Inc.); WP2, Achromatic half-wave plate (AHWP05M-980, Thorlabs); P1, Glan-laser polarizer (PGL 5008, Union Optics); P2, Glan-laser polarizer (GL5-B, Thorlabs); BE1,2, Beam expander (BE02-05-B, Thorlabs)

3.2.2 Control sequence

The simplified schematic of fast spectral CARS microscopy is shown in Fig. 3.2. Personal computers (PC1, PC2) were mainly used for controlling the AOTF laser operation and image acquisition, respectively. Before starting spectral imaging, the AOTF laser pulses and the picosecond mode-locked laser pulses should be synchronized. This synchronization was conducted by employing a phase-locked loop mechanism using the electronic phase detector and the balanced cross-correlator as parts of the pulse synchronization system. It was also necessary to store proper amplitude and frequency values of the RF wave in the AOTF driver for determining the wavelength change of the AOTF laser. The values of amplitude and frequency of the RF wave could be adjusted in the PC1, and then the new values should be sent and stored in the AOTF driver replacing the previous ones. During the wavelength scanning, PC1 sent trigger pulses to the AOTF driver to start the wavelength changes. Wavelength changes were performed rapidly within one millisecond or less, and the pulse synchronization system attempted to recover the synchronization within 20 ms. Then, the DSP sent a trigger signal to an electron-multiplying coupled-charge device (EM-CCD) camera (Ixon, Andor) for image acquisition. The images were displayed and stored in PC2. The total time required to complete imaging at every wavelength change should include both the image acquisition and the resynchronization process. The wavelength change, the resynchronization, and the image acquisition processes were repeated until the whole scanning process was completed. Figure 3.3 shows the time chart for this automatically control to perform fast spectral CARS imaging.

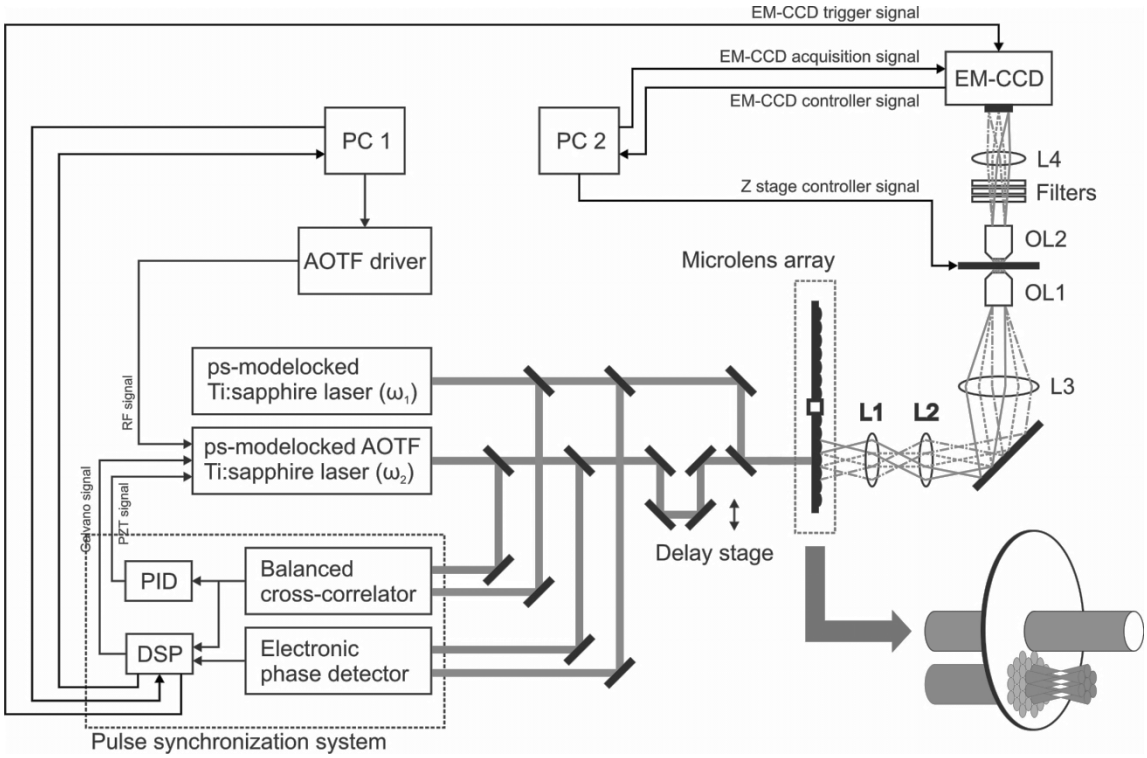

Figure 3.2. The simplified schematic of fast spectral CARS microscopy system with microlens array scanner and high-speed tunable laser.

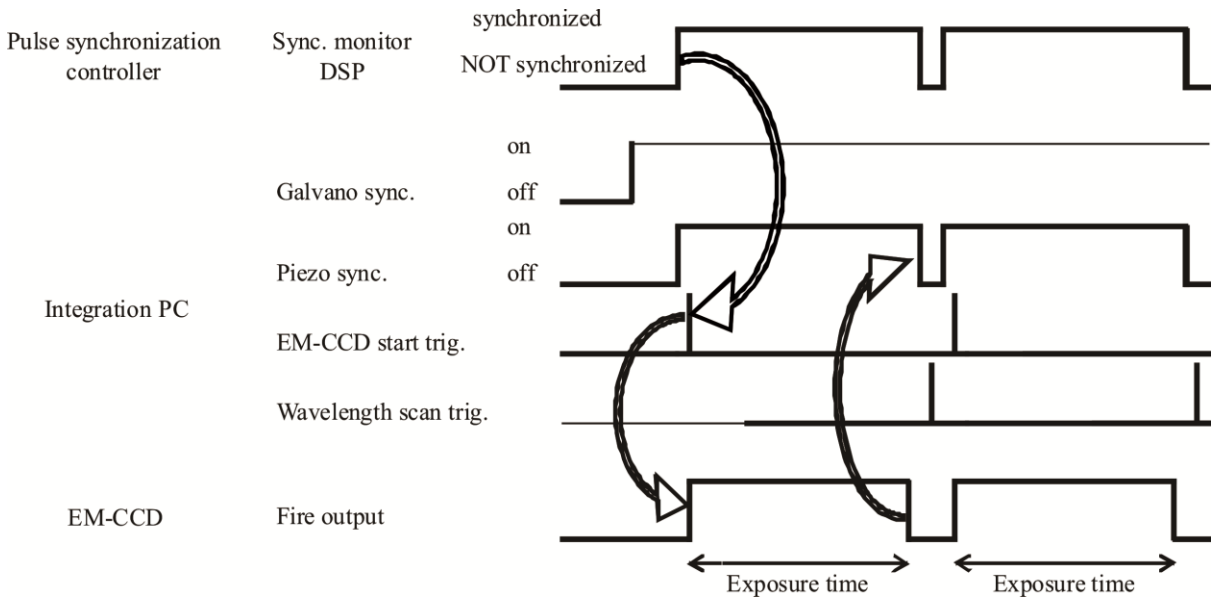

Figure 3.3. Time chart for automatic imaging mechanism using fast spectral CARS microscopy

3.2.3 Multi-focus scanning system

Intense light sources are needed to efficiently excite the molecular vibration and generate sufficient CARS radiation. The efficiency is then enhanced more by tightly focusing the overlapped beams on the sample using objective lens with high numerical aperture. An image was reconstructed by either scanning the beams over observation area or spatially scanning the sample plane on the beams focusing. The dwell time on the sample decrease significantly during the high-speed imaging using single-focus beam scanning. Hence, one should increase the intensity of the excitation beams to compensate for the short dwell time. The fact that the intensity of picosecond pulse laser is less than a few of tens of milli-Watts, typically only a few milli-Watts, restricts the limit of laser intensity introduced to the sample.

Other considerations that should also put into account when high intensity pulse laser is introduced into sample are the photothermal and photochemical damages. In particular for observation of biological samples which mainly contain water, the absorption in the wavelength range between 700-1100 nm seems to be non-negligible [84]. Fortunately, the thermal heating effect can be suppressed by the use of ultrashort pulse laser because most biological samples have lack of one-photon absorption efficiency in this region, except the cellular organelles with high concentration pigments, for example: hemoglobin, melanin, and chlorophyll [85]. Rather than photothermal damage, the nonlinear optical processes induce severe photochemical damage. With respect to the use of ultrashort pulse laser (especially femtosecond pulse laser), the nonlinear optical processes, such as two-photon absorption and three-photon absorption, occur effectively. However, the photodamage mechanism is likely to be a little bit different in CARS [86] and other coherent Raman scattering processes. The absorption due the molecular vibration may contribute to the major cause of photodamage.

Instead of increasing the peak power of the pulse laser, one can improve the image quality produced by nonlinear optical microscopy by expanding the temporal and/or spatial

partition. Expanding the temporal partition can be achieved by increasing the repetition frequency of the laser [91, 92]. Consequently, the mean intensity of the excitation beam is increased which in turn induces the increase of total intensity from the sample. Following the similar manner, the expansion of spatial partition can be attained from the use of multi-focus scanning system which introduces some focal spots on the sample simultaneously [87-90]. The improvement of excitation efficiency on the sample leads to the capability of fast imaging.

The schematic of image acquisition in multi-focus CARS microscopy system is shown in Fig. 3.4. The microlens array disc (MLA1-DD, Nanophoton) contains well-arranged microlenses which each of them has a diameter of 0.58 mm and focal length of 11.6 mm. The schematic and photograph of the microlens array scanner system are shown in Fig. 3.5. When laser beam with diameter of 2 mm is directed into the microlens array disc, 7 focal spots are appeared on the sample plane. Maximum number of the focal spots that can be produced by the microlens array disc is 200 foci which is limited by the maximum diameter of laser beam around 10 mm and the aperture on the housing of the microlens array disc. The microlens array scanner is capable of acquiring 12 images per rotation which equals to 1000 images per second with the maximum angular speed of 5000 rpm.

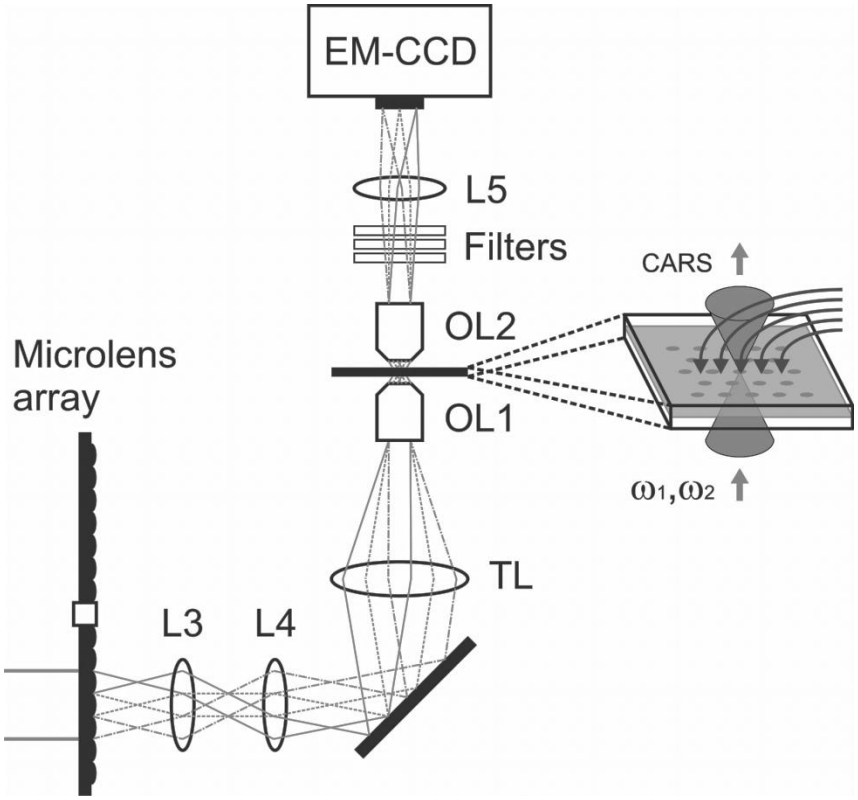

Figure 3.4. Optical setup of real-time CARS microscopy system with microlens array. L3: First relay lens (f50 mm). L4: Second relay lens (f100 mm). L5: Imaging lens (f200 mm). TL: Tube lens (f200 mm). OL1: Objective lens for focusing excitation laser beams (S Fluor, x10, N.A. 0.50, Nikon). OL2: Objective lens for correcting CARS radiation (UPlanApo, x40, N.A. 0.85, Olympus, or NIR Apo, x60, N.A. 1.0, Nikon).

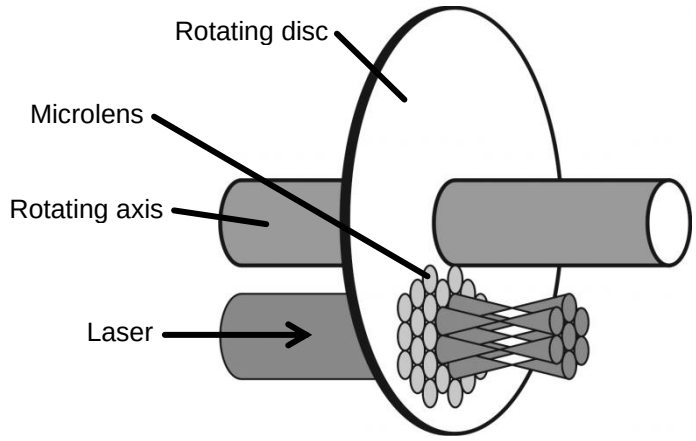

(a)

(b)

Figure 3.5. (a) Schematic and (b) photograph of multi-focus scmicrolens array disc

3.3 Fast spectral CARS microscopy for application in biological imaging

3.3.1 CARS imaging at rates faster than video rates

One of the suitable applications of CARS microscopy in biological imaging is the detection of lipid. Lipid contains abundant CH structures that emit strong vibrational signals in the Raman shift region from 2800 cm^{-1} to 3000 cm^{-1}, which is known as the CH vibrational region. As a model of lipid inside the cellular structure, I choose the adipocytes known as the

fat storing cells in mamalia. Further detail about lipid and adipocytes will be explained in other chapter of this dissertation (Chapter 5).

I demonstrated the performance of the developed CARS microscopy system for imaging at rates faster than video rates (~33 ms per frame). I tuned the Raman vibration to 2850 cm^{-1} for imaging lipid droplets in adipocytes and acquired CARS images at 10 ms/frame. The sample stage was moved during imaging to observe some locations. CARS images observed at some time points are shown in Fig. 3.6, presenting with timestamps. It shows various size and number of lipid droplets in different cells.

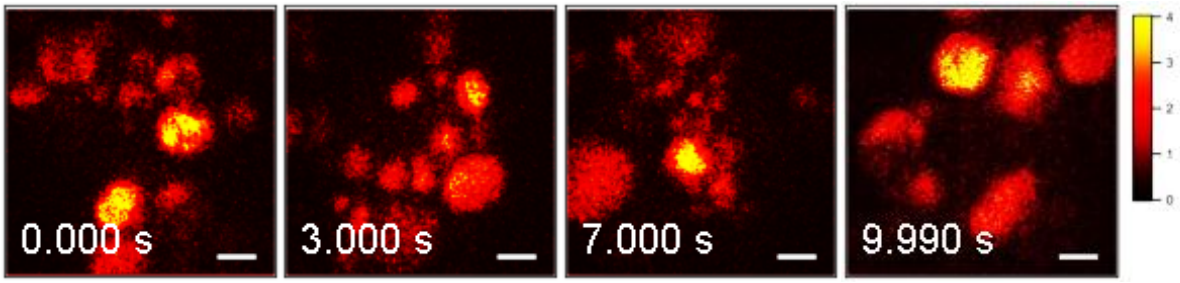

(a) (b) (c) (d)

Figure 3.6. (a–d) CARS images of lipid droplets in 3T3-L1 adipocytes from different locations taken at 2850 cm^{-1}. Acquisition time = 10 ms/image. Scale bar = 10 μm.

3.3.2 Spectral CARS imaging

Spectral CARS images of adipocytes in the CH vibrational region were observed by scanning the wavelength of the AOTF laser every 0.5 nm from 875.0 to 905.0 nm, which corresponded to a Raman shift of 2663.21 to 3049.41 cm^{-1}. For a 100 ms exposure time, the imaging process requires 120 ms/image to cover the wavelength change, laser resynchronization after the wavelength change, and image acquisition. To produce final images, the contributions of dark noise and the background from the CARS images were removed by subtraction. I also considered intensity fluctuations of the AOTF laser during

wavelength scanning and took this into account. Figure 3.7 shows spectral CARS images of 3T3-L1 adipocytes at 2663.21 cm^{-1}, 2845.31 cm^{-1}, and 2896.26 cm^{-1}, which were assigned to off-resonant vibration, CH_2 symmetric stretching vibration, and CH_3 stretching vibration, respectively. A CARS spectral profile in Fig. 3.7d was reconstructed by averaging the intensity in a 5×5-pixel area of interest (noted by white arrow in Fig. 3.7a–c).

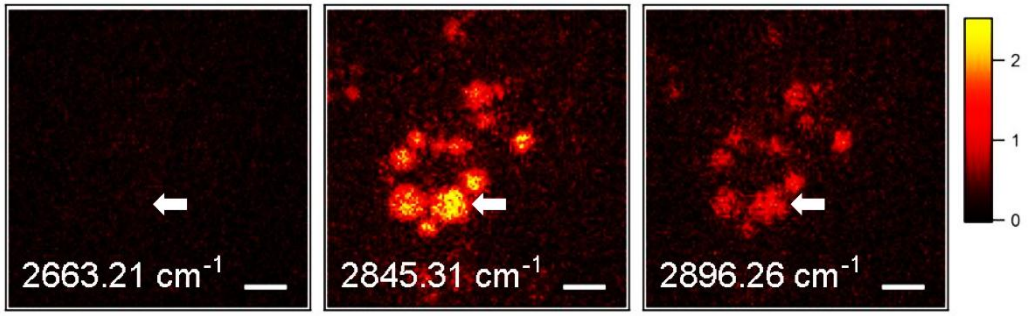

(a) (b) (c)

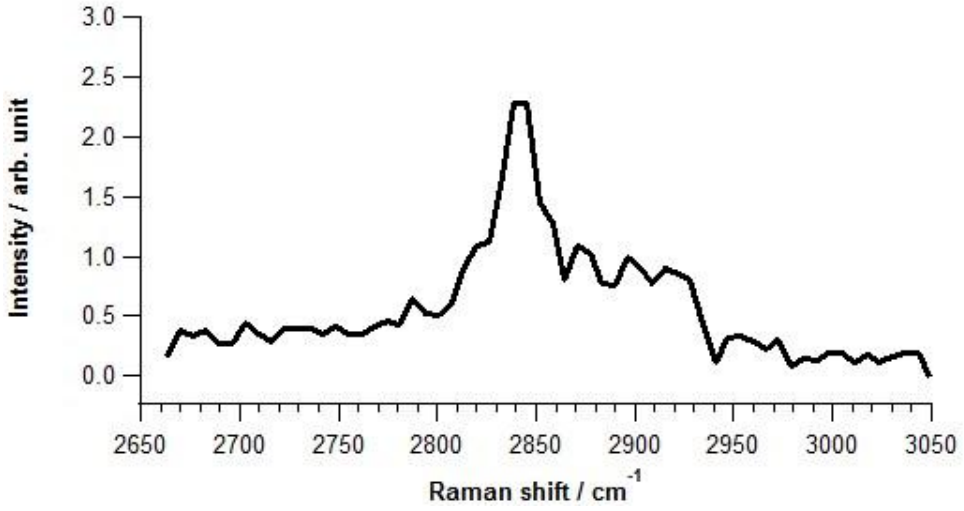

(d)

Figure 3.7. Spectral CARS images of adipocytes at (a) 2663.21 cm^{-1}, (b) 2845.31 cm^{-1}, and (c) 2896.26 cm^{-1}, assigned to non-resonant vibration, CH_2 symmetric stretching vibration, and CH_3 stretching vibration, respectively, taken with fast spectral CARS imaging system. Acquisition time = 120 ms/image. (d) CARS spectral profile reconstructed from area of interest indicated by white arrow in a–c (averaged over 5×5 pixels). Scale bar = 20 μm.

3.3.3 Fast switching CARS imaging

Deuterated lipid contains abundant CD bonds instead of CH bonds in its carbon chain. A deuterated lipid has a Raman vibration that is significantly downshifted to the silent region around 2100 cm^{-1} where no interference from biological specimens occurs [3, 63-65, 94, 95]. A stable, fast switching process between Raman shift of CD and CH is needed to distinguish the deuterated and non-deuterated lipid. I observed a mixture of deuterated and non-deuterated stearic acid as a sample for a rapid switching experiment using the developed fast spectral CARS microscopy system. This sample enabled us to detect sufficiently high Raman signals of CH_2 stretching and CD_2 stretching at 2850 cm^{-1} and 2100 cm^{-1}, respectively (Fig. 3.8a-b). For that purpose, the AOTF laser was rapidly switched between 833 nm and 888 nm, and CARS images were acquired within 520 ms/image. The merged CARS image indicated the locations where the deuterated and non-deuterated stearic acids were independently and colocatedly recrystallized (Fig. 3.8c). Hence, it is possible to use the CD bond as a chemical tag in CARS microscopy and other Raman-based microscopy. For instance, the exogenous lipid with deuterated structure should be distinctly detectable because naturally there is no deuterated lipid isotope inside the cells.

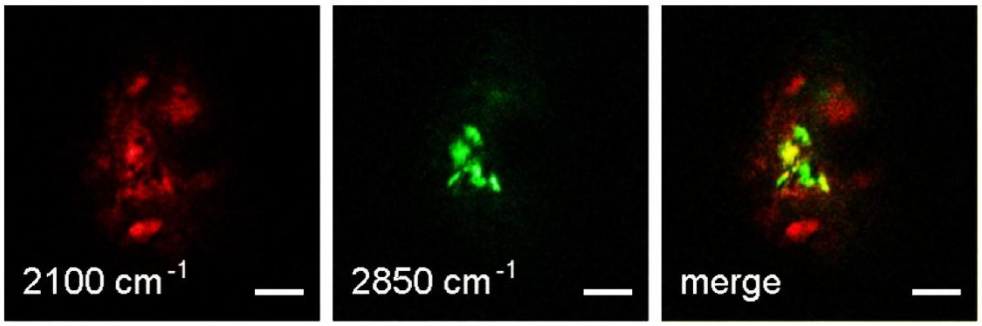

(a) (b) (c)

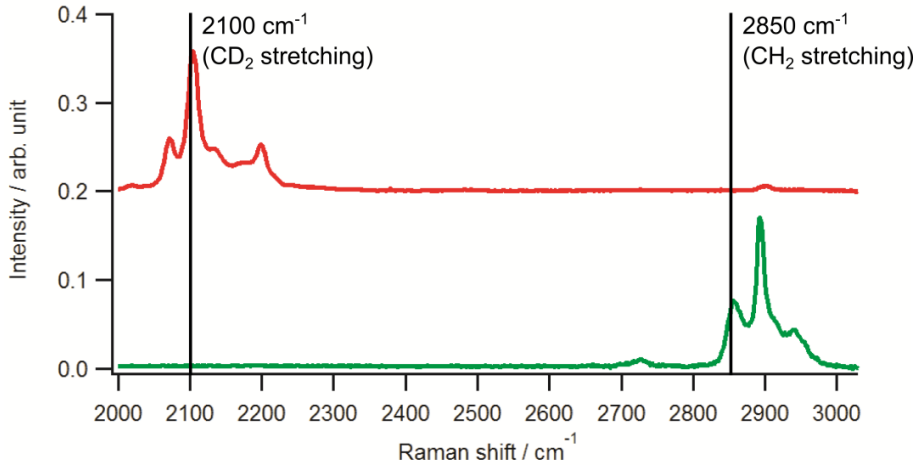

(d)

Figure 3.8. Fast switching CARS images of recrystallized deuterated and non-deuterated stearic acid mixture at (a) 2100 cm^{-1} and (b) 2850 cm^{-1}, assigned to CD_2 and CH_2 symmetric stretching vibrations. Imaging time = 520 ms/image. (c) Merged CARS images from a and b. (d) Spontaneous Raman spectra of each fatty acid. Red = deuterated stearic acid. Green = non-deuterated stearic acid. Yellow = collocated deuterated and non-deuterated stearic acid. Scale bar = 20 μm.

3.4 Summary

I employed the AOTF laser as a Stokes pulse source and constructed a fast spectral CARS microscopy system. The system demonstrated the capability of fast imaging acquisition at rates of 10 ms per frame (faster than video rates, ~33 ms per frame). The AOTF laser enables the fast spectral imaging over wide range around 400 cm^{-1} or equal to around 30 nm. It also allows fast switching imaging between two significantly different wavelengths

corresponding CD_2 stretching and CH_2 stretching vibrations that belonged to deuterated and non-deuterated stearic acid, respectively.

Chapter 4
Spectral SRS microscopy system

4.1 Introduction

CARS microscopy is a powerful tool for label-free imaging with high molecular sensitivity. However, the contribution of non-resonant background becomes its major drawback that decreases the image contrast and the sensitivity for detection of weak molecular vibration [11, 12, 19-21]. SRS microscopy presents as an alternative to overcome this problem since SRS can only be occurred if the frequency difference of the incident beams matches a specific molecular vibration, so that SRS microscopy is insensitive to the non-resonant contribution. To realize the spectral imaging, application of a tunable laser is also necessary for the SRS microscopy. OPO is the most popular laser source to provide the wavelength tunability during the spectral imaging [20, 28, 29, 33, 60, 62, 63]. Recently, a compact fiber laser system is also used as an alternative tunable laser [21, 36]. However, both systems involve mechanical action for wavelength tuning which may restrict the range and speed of tuning.

I decided to develop a spectral SRS microscopy using high-speed tunable picosecond laser. The high-speed tunable picosecond laser, which is also known as AOTF laser, meets most criteria for tunable laser source in CRS microscopy. For the image acquisition, I apply the single-focus scanning provided by the galvanometer scanner system and the signal is captured by the home-made photodetector system. As the SRS signal is relatively weak compared to that of the laser source, it is required an intensity modulator and a lock-in

amplifier to retrieve the small signal [20]. The output from the photodetector is then fed into lock-in amplifier before it is displayed and stored in the PC.

4.2 Spectral SRS microscopy system

4.2.1 Optical setup

The optical setup of the spectral SRS microscopy is basically the same as that of spectral CARS microscopy described in the Chapter 3 Section 3.3.1 with minor modification (Fig. 4.1). I employ the picosecond Ti:sapphire mode-locked laser (Tsunami, Spectra Physics) and the tunable AOTF laser (modified from Megaopt, modification has been explained in Chapter 2, Section 2.3) as the laser sources to enable spectral SRS imaging. Since the developed SRS microscopy is based on the SRL mechanism, the electro optics modulator (EOM, EO-AM-R-20-C1, Thorlabs) is placed in the optical path of AOTF laser to modulate its intensity at the frequency of 19.9 MHz (Fig 4.2) and the SRL signal is detected from the other picosecond laser. The EOM operates with a driven signal which has relatively high power (V_π, 21 V @888 nm). Therefore, the signal from a function generator (E-1205, NF) is amplified to satisfy sufficient power using an amplifier (AA290-RS, R. K). A beam expander (BE02-05-B, Thorlabs) is used to increase the size of beam diameter. To enable the adjustment of laser intensity, a pair of achromatic half wave plate (HWP, AHWP05M-980, Thorlabs) and a polarizer (P, GL10-B, Thorlabs) are placed in optical path of each beam before the two beams are overlapped on the dichroic mirror (DM, LP02-785RU, Semrock). The overlapped beams travel through a scanning system provided by galvanometer scanner (Fig. 4.3). The main part of the galvanometer scanner is constructed by a pair of galvano mirrors (GVS001, Thorlabs) for XY scanning with the typical resonant frequency up to 1 kHz. The beams are focused on the sample plane using an objective lens (CFI Plan Apo IR,

x60, NA = 1.27, WI, Nikon) and collected by another objective lens (NIR Apo, x60, NA = 1.0, WI, Nikon).

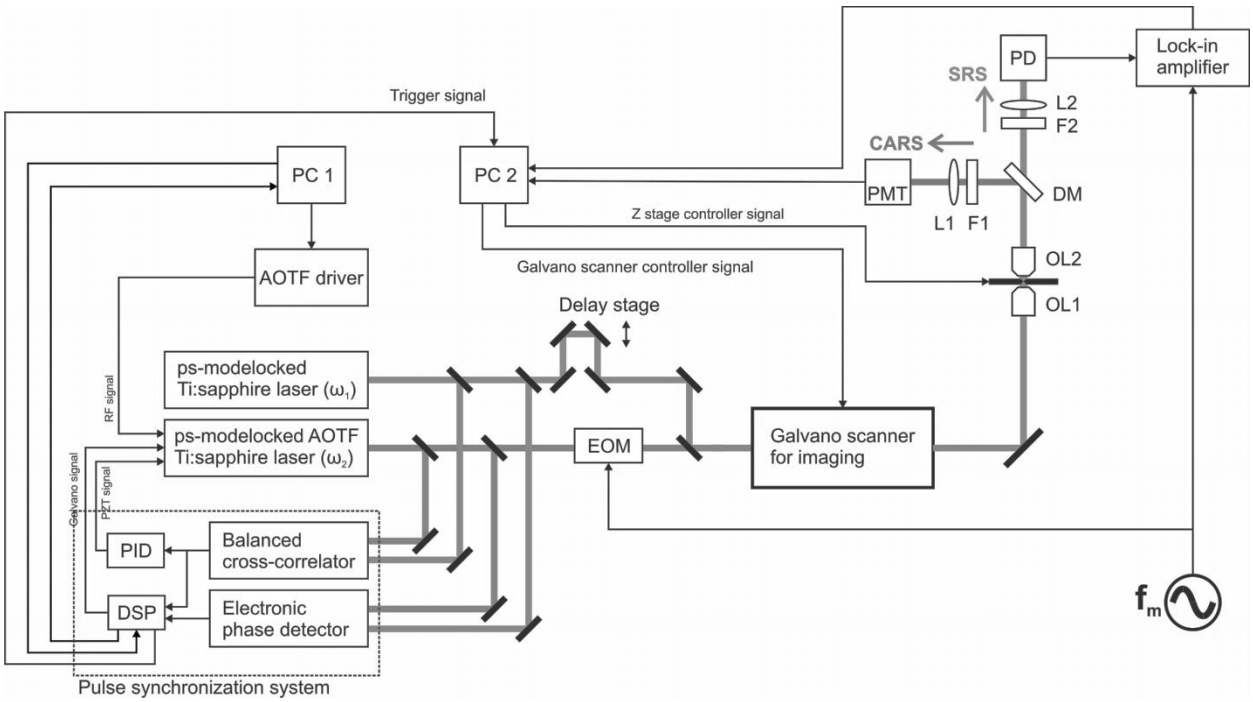

Figure 4.1. The setup of spectral SRS microscopy system with single scanning system and high-speed tunable laser. This setup is a modification from the spectral CARS microscopy system shown in Chapter 3 Fig. 3.8. A delay stage is added on the pump beam optical path. A EOM driven by function generator at frequency of f_m is placed on the Stokes beam path for modulation. Instead of microlens array scanner, single-focus galvano scanner system is used which can be controlled by PC2. On the imaging part, the beam from the sample can be separated as SRS signal and CARS signal by DM mirror (FF665-DiO2, Semrock for detection in the CH vibrational region or FF757-DiO1, Semrock for detection in the fingerprint region). The CARS signal is detected by photo multiplier tube (PMT, C6270, Hamamatsu) while the SRS signal is detected by photodiode (S3399, Hamamatsu) that is integrated into home-made detector system. Output from the PD is deliver to lock-in amplifier (SR844, Stanford Research Systems) locked to the frequency of f_m from function generator for extraction of SRS signal.

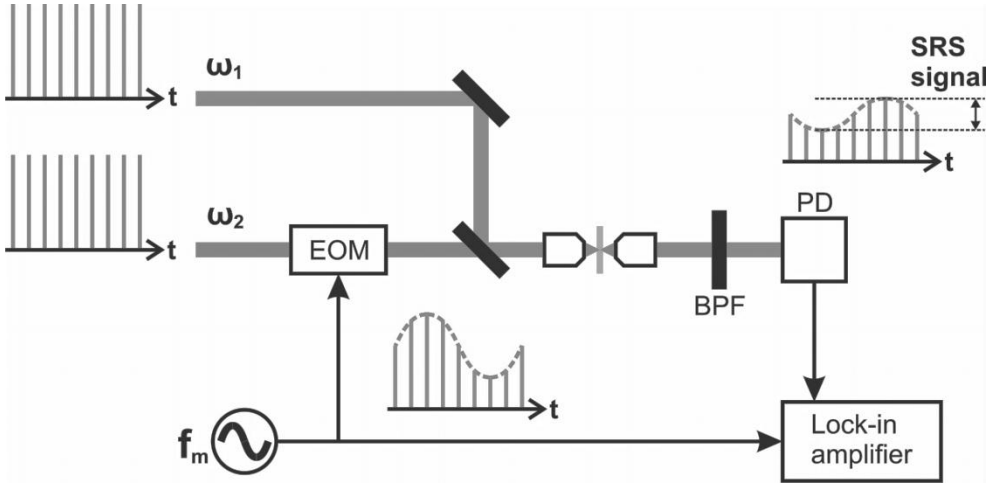

Figure 4.2. Basic setup of SRS microscopy that requires the modulation on one of the excitation beams (in this case, Stokes beam) and lock-in amplifier to demodulate the detected signal by the PD for extraction of SRS signal (in this case occurred due to SRL).

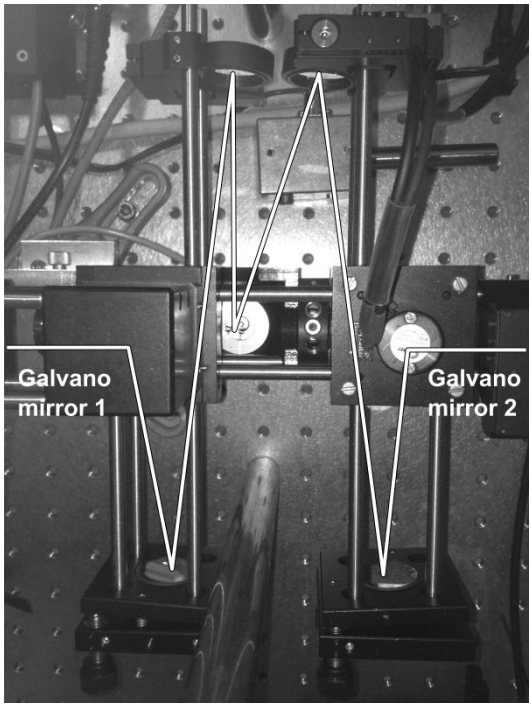

Figure 4.3. Single-focus scanning mechanism by galvano scanner using a pair of galvano mirror (GVS001, Thorlabs) for XY scanning on sample plane, maximum resonant frequency = 1 kHz.

As the CARS and SRS microscopy principally share the same optical components and arrangement, CARS and SRS signals can be detected from the same setup. Therefore, the

beam collecting from the sample can be then separated into two paths (Fig. 4.4) by a long-pass beam splitter (FF665-DiO2, Semrock for detection in the CH vibrational region or FF757-DiO1, Semrock for detection in the fingerprint region). The CARS signal is extracted from the reflected beam by a set of filters (long pass filter (710 nm, Sigma Koki), band-pass filter (560–640 nm, 3RD560-640, Omega), short pass filter (760 nm, 3RD760SP, Omega) for detection in the CH vibrational region; or notch filter (785 nm, NF01-785U-25, Semrock), band-pass filter (650–760 nm, 3RD650-760, Omega), short pass filter (770 nm, 3RD760SP, Omega) for detection in the fingerprint region), and detected by a photo multiplier tube (PMT, C6270, Hamamatsu). The sensitivity of the PMT can be adjusted by the handmade variable voltage source from 0 V to 5 V. The output from the PMT is amplified and converted into electric voltage (As-905-1, NF), and then is sent to PC2. The transmitted path provides the beam carried the SRL signal which is obtained by introducing a laser line filter (FF01-711, Semrock for detection in the CH vibrational region, or LL01-780, Semrock for detection in the fingerprint region) and an ND filter (ND10A, OD: 1.0, Thorlabs). The beam is then detected by a PIN photodiode (PD, S3399, Hamamatsu) which is integrated into a home-made detector system. The SRL signal is extracted from the PD output with a lock-in amplifier (SR844, Stanford Research Systems) and is then sent to PC2. Finally, the CARS/SRS image were observed on and stored in PC2.

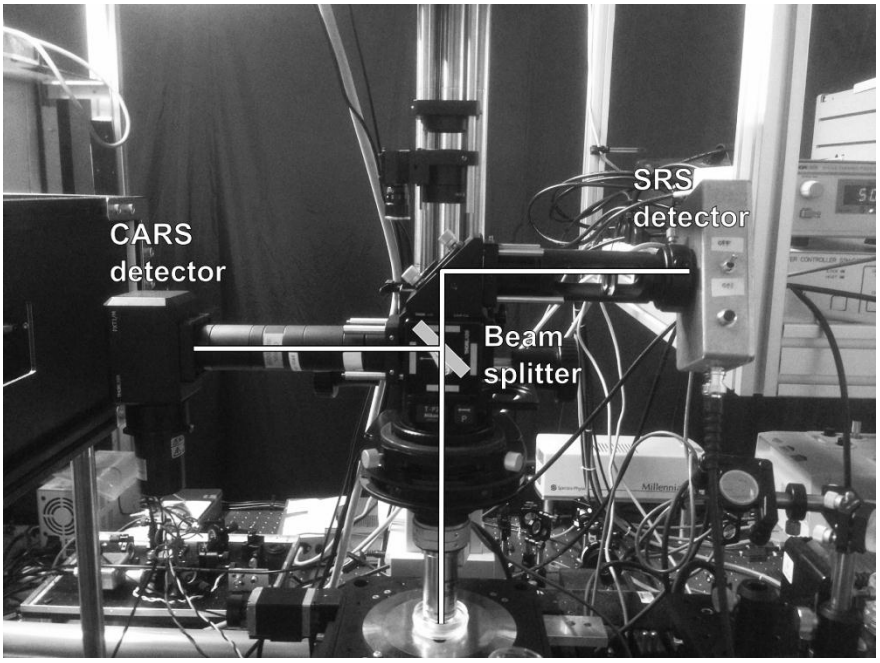

Figure 4.4. Photograph of imaging part in spectral SRS microscopy. The beam from the sample is separated into CARS signal and SRS signal by a long pass beam splitter (FF665-DiO2, Semrock for detection in the CH vibrational region or FF757-DiO1, Semrock for detection in the fingerprint region). CARS signal is detected by a photo multiplier tube (PMT, C6270, Hamamatsu) with a set of filter combination (notch filter (785 nm, NF01-785U-25, Semrock), band-pass filter (650–760 nm, 3RD650-760, Omega), short pass filter (770 nm, 3RD760SP, Omega) for detection in the Raman shift of 500–2000 cm^{-1}; or long pass filter (710 nm, Sigma Koki), band-pass filter (560–640 nm, 3RD560-640, Omega), short pass filter (760 nm, 3RD760SP, Omega) for detection in the Raman shift of 2000–3500 cm^{-1}). The pump beam carried the SRS signal is filtered using a laser line filter (FF01-711, Semrock for detection in the Raman shift of 2000–3500 cm^{-1}, or LL01-780, Semrock for detection in the Raman shift of 500–2000 cm^{-1}) and then is detected by a photodiode (S3399, Hamamatsu) integrated into home-made detector system.

4.2.2 Lock-in detection in SRS microscopy

SRS microscopy provides an amplification to the Raman vibrational energy at transitional rate, so that one of the excitation beam experiences an intensity gain (stimulated Raman gain/SRG) while the other one oppositely experiences an intensity loss (stimulated Raman loss/SRL). Nevertheless, this intensity gain/intensity loss is still relatively smaller

than the intensity of the excitation beams [20, 24]. Consequently, the SRS signal is usually sunk under the excitation beam noise. Therefore, an ultimate detection method to recover the SRS signal is obviously needed. Taking advantage by the fact that the noise that conceals the SRS signal occurs in the low frequency region, one can apply a lock-in detection method at higher frequency (recently at the typical value of some MHz to a few ten of MHz).

The lock-in detection, which is also known as phase-sensitive detection, has been applied in various applications [96-99]. It is a common method to detect small signal that is buried in the noise by the use of a reference at the same frequency as the modulator of the detected signal [100, 101]. The reference frequency is usually provided by a fixed frequency from an oscillator or a function generator.

The schematic of the lock-in amplifier is presented in Fig. 4.5. The input signal is assumed as sinusoidal signal given by:

$$V_1 = V_{sig}\sin\left(\omega_{sig}\,t + \theta_{sig}\right), \tag{4.1}$$

where V_{sig}, ω_{sig}, and θ_{sig} are the amplitude, the frequency, and the phase of the input signal, respectively. The lock-in amplifier usually generates internal reference signal:

$$V_2 = V_{ref}\sin\left(\omega_{ref}\,t + \theta_{ref}\right), \tag{4.2}$$

where V_{ref}, ω_{ref}, and θ_{ref} are the amplitude, the frequency, and the phase of the internal reference signal, respectively. The lock-in amplifier amplifies the input signal and multiplies it with the internal reference signal using a phase sensitive detector (PSD) which basically is a multiplier. The output from the multiplier is given by:

$$\begin{aligned} V_{PSD} &= V_{sig}\sin\left(\omega_{sig}\,t + \theta_{sig}\right) V_{ref}\sin\left(\omega_{ref}\,t + \theta_{ref}\right) \\ &= \tfrac{1}{2}\,V_{sig}\,V_{ref}\cos\left[\left(\omega_{sig} - \omega_{ref}\right)t + \left(\theta_{sig} - \theta_{ref}\right)\right] \\ &\quad -\tfrac{1}{2}\,V_{sig}\,V_{ref}\cos\left[\left(\omega_{sig} + \omega_{ref}\right)t + \left(\theta_{sig} + \theta_{ref}\right)\right], \end{aligned} \tag{4.3}$$

If $\omega_{sig} = \omega_{ref}$ and the PSD output is passed through a low pass filter, the remaining PSD signal will be:

$$V_{PSD} = \frac{1}{2} V_{sig} V_{ref} \cos(\theta_{sig} - \theta_{ref}), \quad (4.4)$$

It is suggested from Eq. 4.4 that the remaining signal is a DC signal proportional to the amplitude of input signal. Consequently, the consistency of the phase of the input signal and the internal reference signal should remain unchanged over time or otherwise the value of $\cos(\theta_{sig} - \theta_{ref})$ will alter and V_{PSD} will not be a DC signal anymore. Therefore the internal reference signal should be locked to an external reference signal using a phase-locked loop (PLL). The PLL actively monitors the external reference signal, so that the frequency change of the external reference signal is negligible. One can rewrite Eq. 4.4 as follows:

$$V_{PSD} = \frac{1}{2} V_{sig} V_{ref} \cos\theta, \quad (4.5)$$

where θ is the phase difference between the input signal and the internal reference signal. By adjusting θ_{ref}, one can make either θ value is zero so that V_{sig} can be measured or conversely θ value is $\pi/2$ so that no output can be detected. This mechanism is known as single-phase lock-in detection and the output is simply given by

$$V_{out} = V_{sig} \cos\theta, \quad (4.6)$$

By providing a second PSD with the phase of the internal reference signal is shifted by $\pi/2$, two different PSD signals are obtained:

$$V_{PSD1} = \frac{1}{2} V_{sig} V_{ref} \cos\theta, \quad (4.7a)$$

$$V_{PSD2} = \frac{1}{2} V_{sig} V_{ref} \sin\theta, \quad (4.7b)$$

Hence, now one has two outputs: the first one (X) is proportional to $\cos\theta$ and the second one (Y) is proportional to $\sin\theta$:

$$X = V_{sig} \cos\theta, \quad (4.7a)$$

$$Y = V_{sig} \sin\theta. \quad (4.7b)$$

These two signals represent the input signal as a vector relative to the internal reference signal of the lock-in amplifier. When there is no phase difference between both signals, X will reveal the input signal while Y will equal to zero. Thus, X is known as the in-phase component and Y is known as the quadrature component, and then this mechanism is called the binary-phase lock-in detection. By calculating the magnitude R of the signal vector, the phase dependency does not affect anymore:

$$R = \sqrt{X^2 + Y^2} = V_{sig} \, . \tag{4.8a}$$

Additionally, one can attain the value of the phase difference θ in exchange by calculating

$$\theta = \tan^{-1}\left(\frac{Y}{X}\right). \tag{4.8b}$$

In the application for SRS microscopy, the binary-phase lock-in amplifier will directly measure the amplitude of SRS signal which are phase-independent and also show the phase difference change during the measurement of SRS signal.

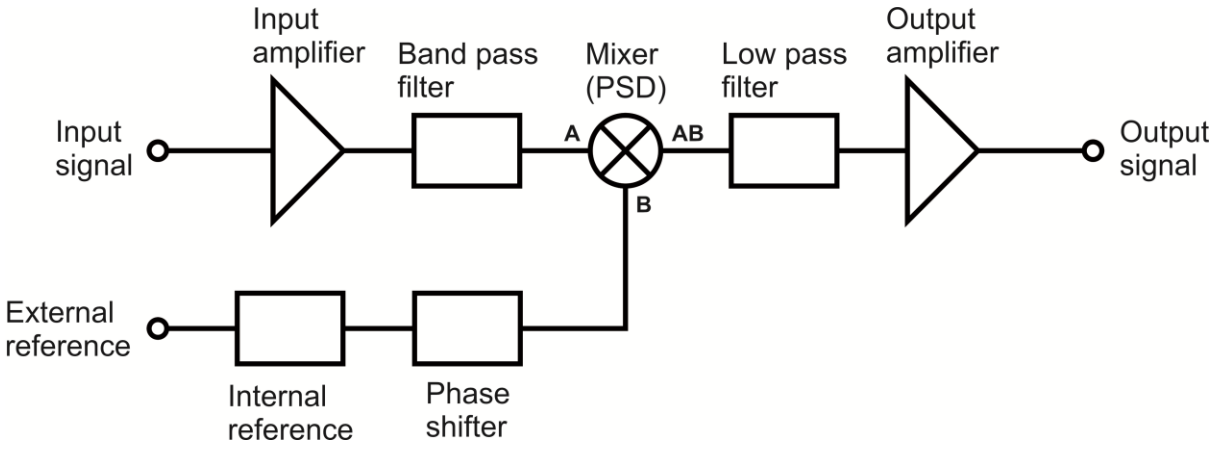

Figure 4.5. General mechanism of lock-in detection. The input signal is amplified and filtered using a band pass filter to remove low frequency noise. The filter signal is then multiplied with the internal reference signal. The multiplied signal is filtered using low pass filter to reject the high frequency noise from the repetition frequency of the laser. Then, it is amplified again to provide sufficient signal for displaying and storing. The internal reference signal is locked to the modulating frequency of Stokes beam.

4.2.3 Modulation of excitation beam

Modulation on one of the excitation beams with a known fixed frequency is required to enable the lock-in detection for extracting the SRS signal. For experiment, I modulate the Stokes beam which provided by the AOTF laser and detected the SRL signal from the pump beam provided by another picosecond laser. For the intensity modulator, I apply an electro optic modulator (EOM, EO-AM-R-20-C1, Thorlabs) that is driven by the amplified sinusoidal signal from a function generator (Fig. 4.6).

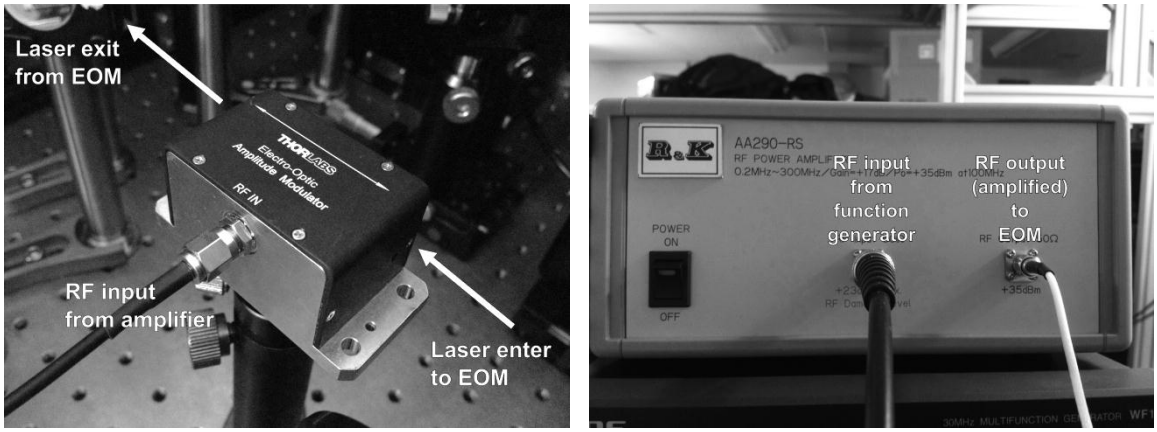

Figure 4.6. Photograph of EOM (EO-AM-R-20-C1, Thorlabs) and power amplifier (AA290-RS, R. K) to amplify the driven oscillating signal from function generator (E-1205, NF).

EOM is a Pockell cell-type modulator made from an electro optic crystal, such as Lithium Niobate/$LiNbO_3$, which is typically connected to a pair of electrode driven by a variable electric field [24]. As an optical beam travels inside the Pockell cell at certain distance to which an electric field is applied will undergo a phase shift (Fig 4.7a). The applied electric field leads to the change of refractive index of the crystal. As the result, the travelling beam will experience a retardant effect which linearly depends on the applied electric field given by (Fig 4.7b):

$$\Gamma = \Gamma_0 - \pi \frac{V}{V_\pi}, \tag{4.9}$$

where Γ and Γ_0 are the phase retardation occurred in the presence and absence of the electric field *V*. The important parameter for this kind of device is knows as half-wave voltage (V_π). It is defined as the applied voltage which induces the phase shift by π. The parameter V_π is determined by the material properties (refractive index n, Pockell coefficient r, the EOM contains two types material with different polarizations) on the wavelength λ_0 and on aspect ratio of d/L (d is distance of two electrodes, L is travelling distance of optical beam in the crystal):

$$V_\pi = \frac{d}{L} \frac{\lambda_0}{r_1 {n_1}^3 - r_2 {n_2}^3}, \tag{4.11}$$

One can therefore easily and rapidly modulate the intensity of the optical beam by varying the value of voltage *V*. The transmittance of the optical beam due to the retardation at a given voltage is equal to

$$T(V) = sin^2\left(\frac{\Gamma_0}{2} - \frac{\pi}{2}\frac{V}{V_\pi}\right), \tag{4.11}$$

The transmittance of the device is then manifested as a periodic function of *V* (Fig 4.7c).

The EOM requires a sufficiently high value of V_π which is difficult for the operation with a few ten of MHz. One can solve the problem by applying a longer crystal to reduce the V_π value (Eq. 4.11). Unfortunately, the use of longer crystal will cause the optical path of the Stokes beam become longer and thus the time difference two lasers will increase significantly. Another alternative to reduce the need of the high value of V_π is the use of resonant frequency of the EOM installed now at 19.9MHz. The voltage requirement vastly decreased from 205 V to 15 V; however the modulation frequency of EOM becomes limited. Additionally, the size of the hole at the entrance and exit of the EOM device hinder the achievement of sufficient power. Two lenses (L3, L4, AC254-200-B-ML, AR coating: 650–1050 nm, *f* = 200 mm, AC254-100-B-ML, AR coating: 650–1050 nm, *f* = 100 mm, Thorlabs)

are put at both ends of EOM to reduce the beam size while entering the EOM so that the output intensity after the EOM is maximized and achieves up to 212 mW. Figure 4.8 shows the temporal profiles of Stokes beam without and with modulation using EOM at 20 MHz which are observed using a photodiode (PDA10A-EC, Thorlabs) and an oscilloscope (TDS2024C, Tektronix).

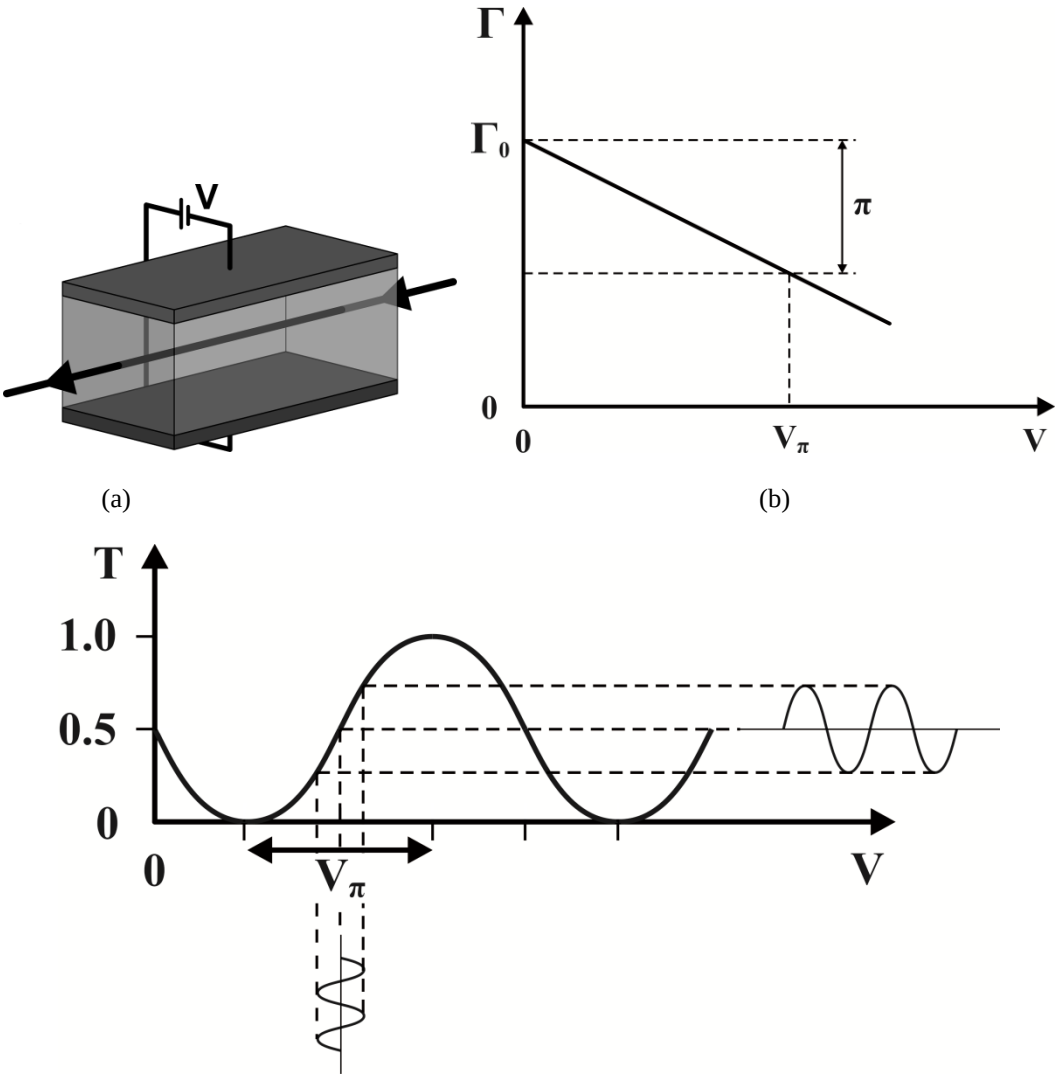

Figure 4.7. (a) Schematic of Pockell cells which is applied as the EOM. (b) Linear correlation between retardation and voltage varying source. (c) The transmittance profile by the voltage varying which in turn change the polarization orientation of the travelling beam.

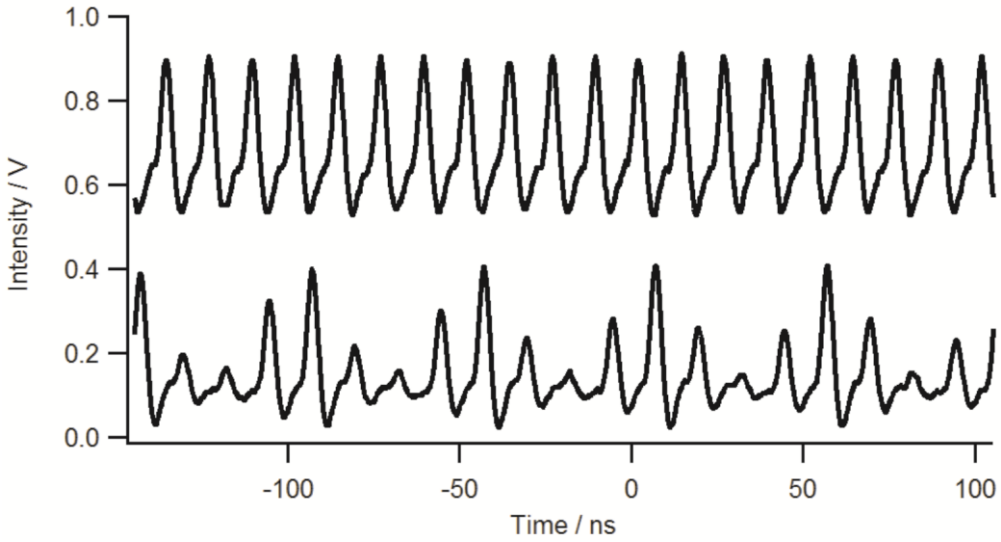

Figure 4.8. The profile of Stokes beam without (upper graph) and with modulation (bottom graph)

4.3 Development of detector system for SRS microscopy

Realizing the need to minimize the noise that interferes with the desired SRS signal, I was motivated to develop a home-made detector system which includes the filter and amplifier for signal treatment before it enter the lock-in amplifier. Basically, I try to suppress the contribution of fundamental beams by filtering and only the expected SRS signal at the modulation frequency can pass to the lock-in amplifier. Preamplification is applied to the signal to increase the sensitivity in the lock-in amplifier detection.

The design of the circuit for the detector system is presented in Fig. 4.9 and Fig 4.10. Here I need to determine the value of the components for the filter. The first part is the band stop filter to ensure that the 20 MHz signal will go to the Output 2 and prevent it to appear in the Output 1. I determined that the components for the 20 MHz band stop filter should be resistor of 250 Ω, inductor of 180 nH, and capasitor of 360 pF. Instead of using fixed capasitor 370 pF, I use a fixed capasitor of 330 pF and variable capasitor (7–50 pF), so that it can be tuned to the accurate value. For the 80 MHz band stop filter, the components are

resistor of 5 kΩ, inductor of 82 nH, and capasitor of 38 pF (33 pF fixed capasitor and 4.5–20 pF variable capasitor). The 20 MHz filtered signal is then enter the input of high-speed response op-amp (AD8099, Analog Device) for preamplification and low noise rejection, and finally produce an output on Output2. The other op-amp is the slow-response one (AD 8597, Analog Device) for outputting a signal considered as the transmitted signal of the sample on Output1. Both op-amps are supplied with dual supply +/- 4.5 V which are obtained from the voltage division of rechargeable 9 V battery by rail splitter (TLE2426CLP, Texas Instrument). The photodiode is supplied with separated 9 V batteries. The Output2 from detector system is then connected to the input of lock-in amplifier.

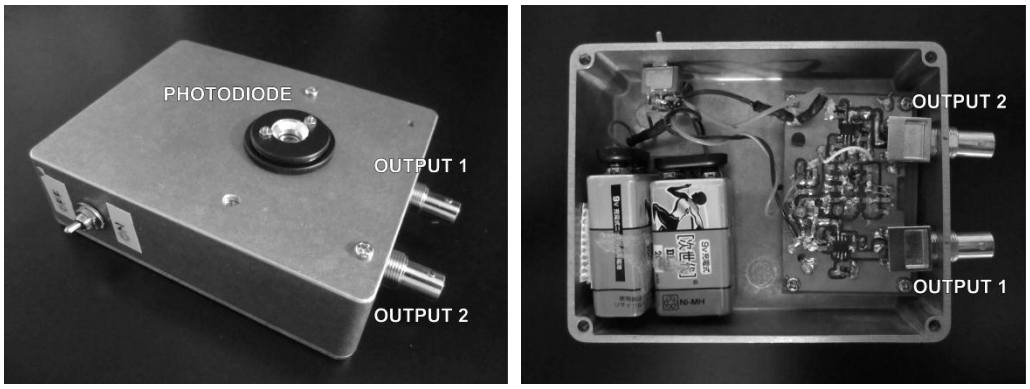

Figure 4.9. Photograph of the home-made detector system for SRS microscopy.

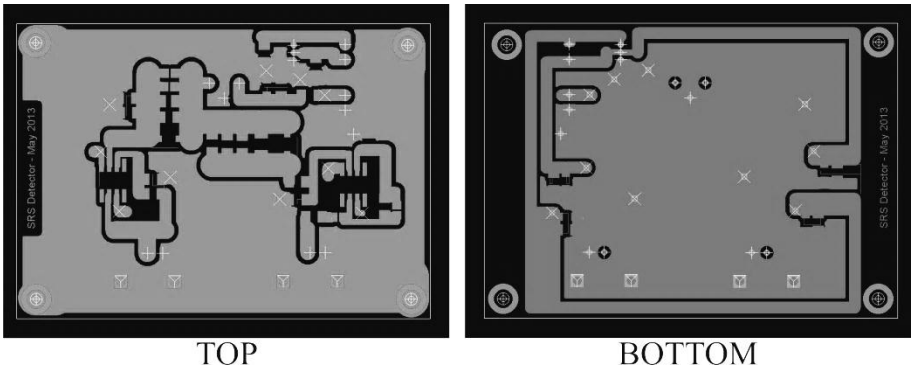

(a)

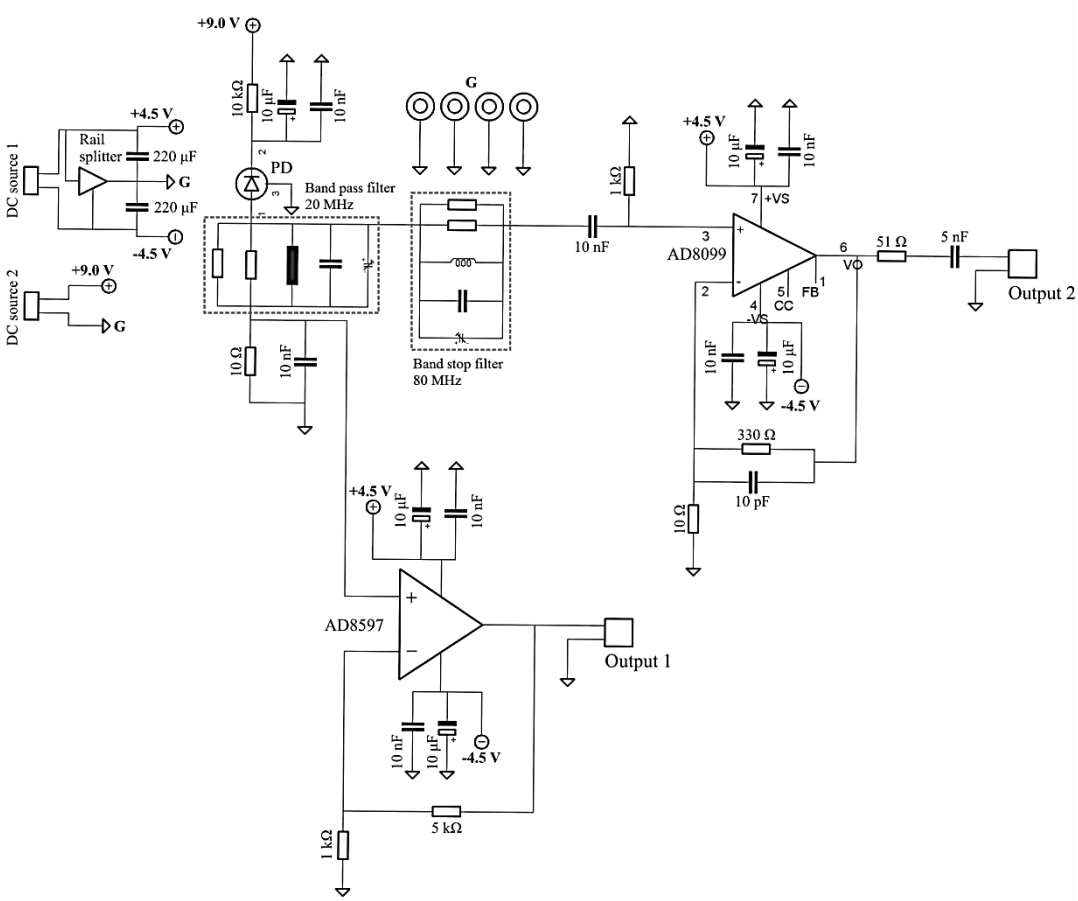

(b)

Figure 4.10. Electronic design of the home-made detector system: (a) IC board patternand (b) correlated schematic diagram created using Eagle 5.1.1 (freeware). Components for the 20 MHz band pass filter: resistor = 2 x 510 Ω, inductor = 180 nH, capasitor = 330 pF (fixed) and 7–50 pF (variable). Components for the 20 MHz band stop filter: resistor = 2 x 10 kΩ, inductor = 82 nH, capasitor = 33 pF (fixed) and 4.5–20 pF (variable). DC source 1 with rail splitter produced +/-4.5 V supply for the op-amp (high-speed response: AD8099, Analog Device; slow response: AD 8597, Analog Device). DC source 2 provided +9 V for the photodiode. Output 1 is the slow response output for transmission image, Output 2 is the high-speed response output for SRS image.

To obtain stronger SRS signal, I can simply increase the intensity of the excitation sources. However, it is not suitable for the application of live cells imaging since the excessive intensity of laser source induce the photodamage [84, 85]. Instead of increasing the intensity of the excitation source, it is preferable to increase the detection sensitivity of the lock-in amplifier by enhancing its detection and by preamplification. The detection range of the lock-in amplifier stretches from 25 kHz to 200 MHz. The input signal is first filtered by 200 MHz low pass filter (LPF) and then attenuated by the value of 20 dB before the 20 kHz high pass filter (HPF). The signal will amplified again by 20 dB for multiplexing with reference signal in the mixer. The signal with low frequency is extracted from the mixer output and is amplified again with variable gain. The signal is converted from analog into digital for extracting its magnitude and phase difference, and then it is converted back into analog signal for acquisition by the PC. Figure 4.11 shows the spectral profile of pump beam which shows appearance of unwanted signal at frequency other than 80 MHz. The signal at 80 MHz originates form the repetition frequency of the laser source while that at 160 MHz originates from the second order harmonic effect. During amplification, these signals lead to the saturation in the lock-in amplifier. The rejection of these signals at earlier process before the lock-in amplification will contribute to the increase of SRS signal. One solution is provided by the design of the detector system as has been explained previously.

I can also put an additional LPF (BLP-21.4+, Mini-circuits) on the input of the lock-in amplifier to cut the 80 MHz signal as shown by the upper graph in Fig. 4.12. The signals detected at the multiples frequency of 20 MHz rise from the aliasing of the original signal at 20 MHz and the repetition frequency of the laser, while those in the lower frequency region are contributed by the noise from electric circuit and power supply of the spectrum analyzer. Those unwanted signal can be greatly removed by the LPF (bottom graph in Fig. 4.12), so

that the use of ND filter to avoid the saturation is no longer needed and the PD can now detect the stronger intensity up to 2.5 mW.

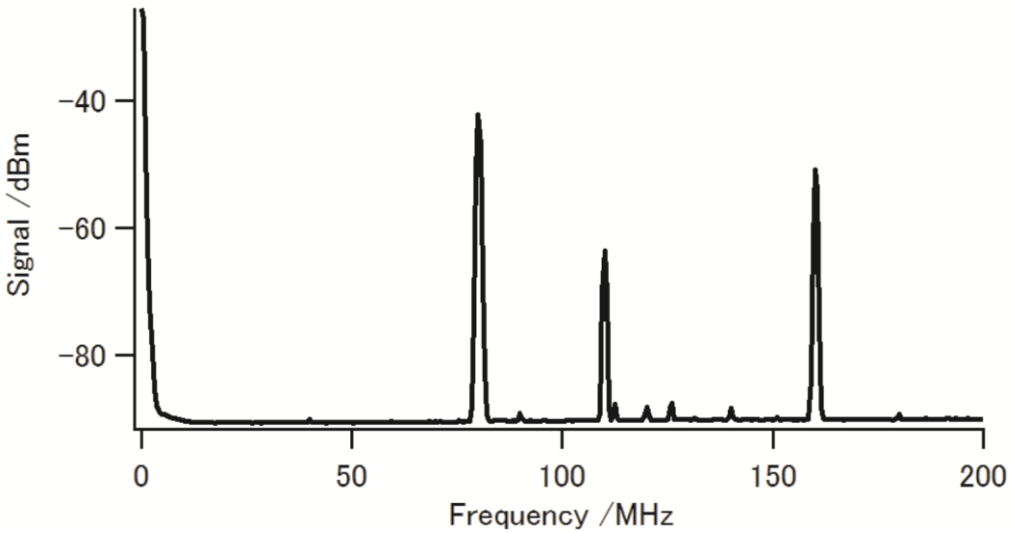

Figure 4.11. Spectral profile of the pump laser detected by the home-made detection system without any filter. 80 MHz = repetition frequency of the laser, 160 MHz = the second order harmonic effect, 120 MHz = aliasing

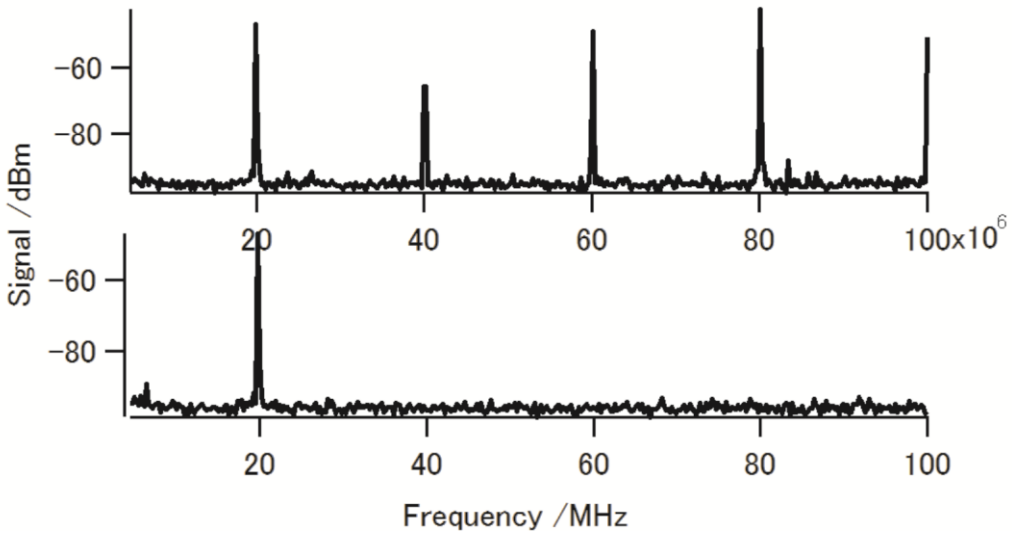

Figure 4.12. Spectral profile of the modulated pump laser detected by the home-made detection system without and with filter. Without filter (upper graph): many signals appear on the multiples of 20 MHz because of second order harmonic effect and aliasing, 80 MHz signal also includes the repetition frequency of pump laser. With filter (bottom graph): only 20 MHz signal appear related to the SRS signal.

4.4 Spectral SRS microscopy for application in biological imaging

4.4.1 Spectral SRS imaging

Spectral images and reconstructed spectral profile were obtained from lipid droplets in adipocytes using the SRS microscopy system with high-speed tunable laser. The AOTF laser was scanned from 875 nm to 905 nm which equaled to Raman shift from 2650 cm^{-1} to 3050 cm^{-1} and covered the whole region of CH vibration. Every image was acquired within 2 s. Since there is no contribution from non-resonant background, I only removed the contribution of dark noise by subtraction and normalized the intensity of SRS signals with the measured intensity of AOTF laser as Stokes pulse source detected by a two-photon detector. Figure 4.13 a-c showed spectral SRS images at 2655.45 cm^{-1}, 2850.81 cm^{-1}, and 2902.56 cm^{-1}, which were assigned to off-resonant vibration, CH_2 symmetric stretching vibration, and CH_3 stretching vibration, respectively. The SRS spectral profile in Fig. 4.13 d was reconstructed by averaging the intensity in a 10×10-pixel area of interest (white arrow in Fig. 4.13 a-c).

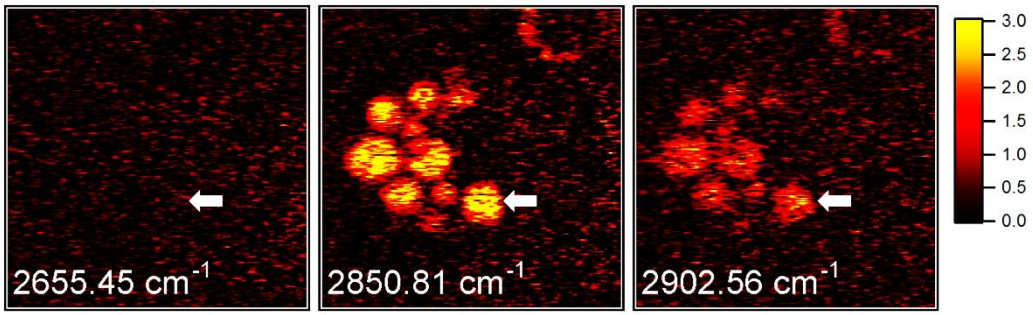

(a) (b) (c)

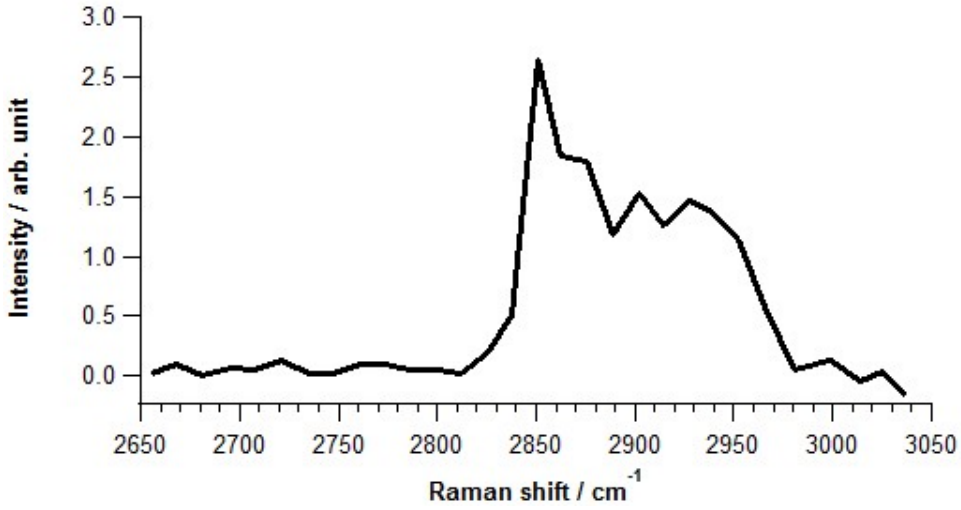

(d)

Figure 4.13. Spectral SRS images of adipocytes at (a) 2655.45 cm^{-1}, (b) 2850.81 cm^{-1}, and (c) 2902.56 cm^{-1}, assigned to non-resonant vibration, CH_2 symmetric stretching vibration, and CH_3 stretching vibration, respectively, taken with spectral SRS imaging system. Acquisition time = 2.5 s/image. (d) SRS spectral profile reconstructed from area of interest indicated by white arrow in a–c (averaged over 10×10 pixels).

4.4.2 Comparison of SRS and CARS images

Here I present the comparison of the results from SRS and CARS microscopy. The main drawback of the CARS microscopy that is superseded in SRS microscopy is the non-resonant background. This non-resonant background usually can be easily observed in the Raman shift that has no assignment of any vibrational band (off-resonant) or that has weak signal such as CD. In Fig. 4.14, the images in the first row show the SRS images at 2100 cm^{-1},

2300 cm^{-1}, and 2850 cm^{-1}, which are assigned to CD_2 symmetric stretching vibration, off-resonant vibration, and CH_2 symmetric stretching vibration. It is obvious that there is no image at the off-resonant, while the image at CD_2 stretching is very weak and can hardly be recognized. However, noticing the images in the second row that belongs to CARS images, there are distinct structures of lipid droplets shown which should not related to the vibrational mode. These images suggest the great contribution of the non-resonant background occurred in CARS microscopy.

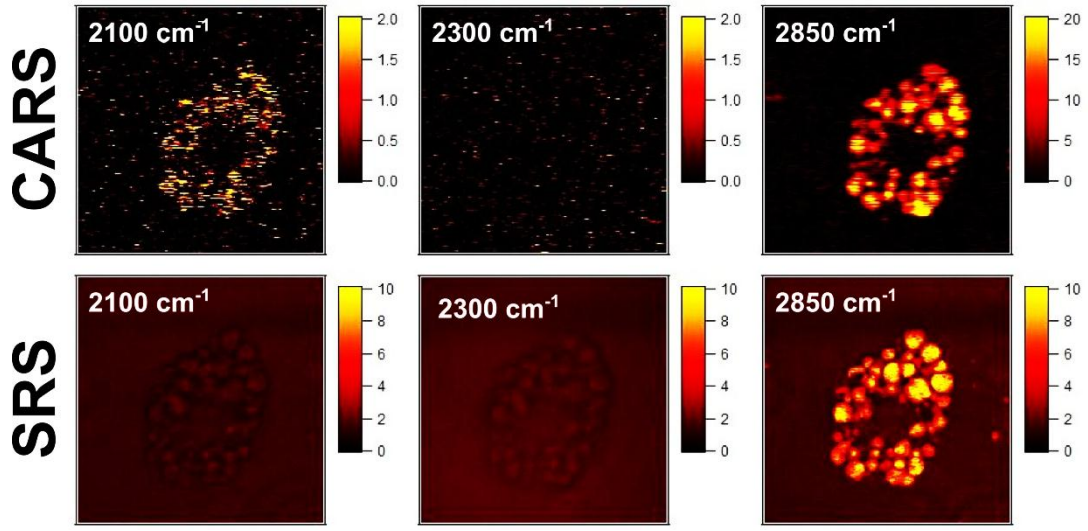

Figure 4.14. Comparison of CARS and SRS images from treated 3T3-L1 adipocytes with deuterated stearic acid. SRS images = upper row. CARS images = bottom row. 2100 cm^{-1} = left column, CD_2 symmetric stretching. 2300 cm^{-1} = middle column, off resonant. 2850 cm^{-1} = right column, CH_2 symmetric stretching.

4.5 Summary

SRS microscopy proved its feasibility as powerful imaging tools for the biological application, especially the absent of non-resonant background. By employing the AOTF laser as a Stokes pulse source, SRS microscopy can perform a spectral imaging of lipid droplets in adipocytes around 2850 cm^{-1}. To retrieve the SRS signal, one should apply the intensity

modulation and lock-in detection for sensitive measurement. Integration of CARS microscopy and SRS microscopy can be useful to complement each other.

Chapter 5
Application of spectral CRS microscopy system using high-speed tunable picosecond laser for lipid droplets imaging

5.1 Introduction

One important concern in biomedical studies is detection and observation of properties and processes of the biomolecules [1, 102]. As the smallest functional structure of organism, cell can act as the container with real environment for biomolecules dynamics [103]. Therefore, study of biomolecule reaction at cellular level becomes an important issue in recent biomedical researches and developments. One of the biomolecule which gets more attention is lipid since the fact that it plays some important roles in living organism as energy storage, structural components of cellular membranes, signaling molecules, and many other functions [53, 104-116]. Lipids represent a broad group of molecules that covers various categories due to their unique structures and metabolism pathways [1, 102]. For biomedical studies, fatty acids and glycerolipids become popular subjects since they involved in many medical diagnosis and diseases.

In general understanding, lipids become very interesting subjects in biomedical researches since lipids are considered as important cellular components with complex profiles. Raman-based microscopy, such as CRS microscopy, offers a powerful method for lipids observation since lipids mainly consist of CH bonds of which the vibrational frequencies uniquely inhabit specific region in Raman spectra [8, 52, 53]. Furthermore, to enhance the

detection of lipids due to the CH bonds, many researchers also take advantages of CD bonds that have isomorphic structures with the correlated CH bonds . The new structures will dramatically downshift the vibrational frequency of CH bonds to the Raman silent region, where there should be no signal from biological specimens will interfere [3, 63, 64, 94, 95].

5.2 Fatty acid and its intracellular metabolism

5.2.1 Fatty acid

Fatty acids are formed by hydrocarbon chains and terminals of carboxylate group (Fig. 5.1). The systematic names of fatty acids follow the names of the hydrocarbon chains and sometimes with variations of molecular orientations and degrees of unsaturation [1, 102]. Fatty acids act as fuel molecules, which provide energy during the rest or moderate activities of organisms. In cooperation with many proteins, fatty acids can also perform as targeting molecules to cellular membranes. Derivatives of fatty acids serve as hormones and carriers of cellular information. Regarding the function of lipid acids as fuel molecules, they go through identical degradation-synthesis processes in their basic chemistry [1, 102]. Degradation is an oxidative process that converts fatty acids into activated acetyl units, whereas synthesis is essentially the reverse of degradation process.

Fatty acids accumulate in organisms' cells as lipid bodies. Lipid bodies are also known with various terms due to their cellular-subcellular locations or functions. Lipid droplets refer to the disposition of the lipid bodies in adipose cells or other fat cells such as fibroblasts [107, 108]. Lipid bodies are usually associated with particular role of tissue in lipid storage or transport. The malfunction of lipid bodies' metabolisms may indicate some specific diseases such as atherosclerosis and diabetes [107, 108]. Recent studies revealed that the roles of lipid

bodies are more complex than simply lipid storage or transport. Here I will use the term lipid droplets instead of lipid bodies.

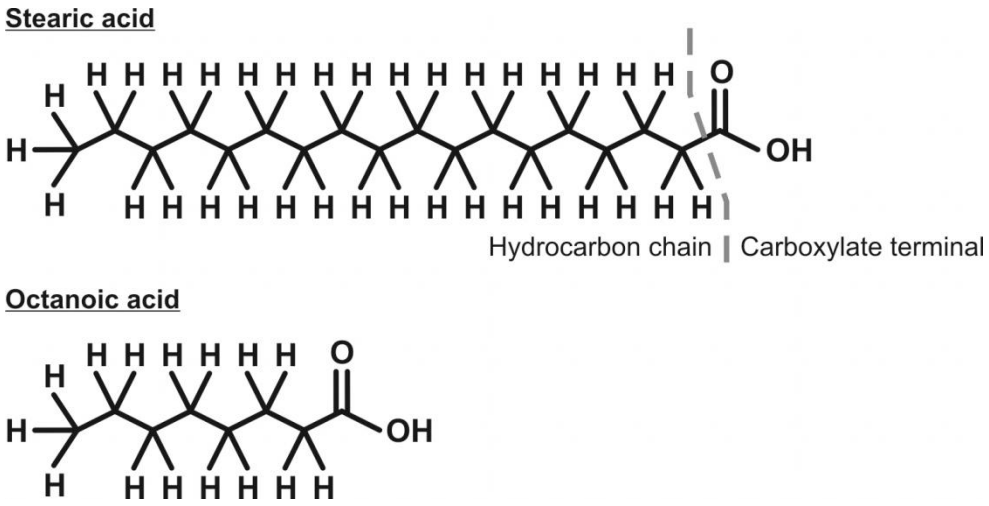

Figure 5.1. Chemical structure of fatty acid is constructed by hydrocarbon chain and carboxylate termina. The given example: octanoic acid (C8) and stearic acid (C18) which were used in the experiments. For deuterated fatty acid, all atom H (H^1) in the hydrocarbon chain are replaced by D (H^2).

5.2.2 Intracellular metabolism of fatty acid

The fatty acids are usually stored in lipid droplets as triacylglicerides (TAG) which are produced by the esterifications of hydroxyl heads in glycerols with different fatty acids (Fig. 5.2). Triacylglicerides or also called as triglycerides (TG) and assumed as neutral fats. TG can highly concentrated store energy because of reduction and anhydration processes [1, 102].

To fulfill the purpose of fatty acids as fuel molecules, fatty acids have to be mobilized, activated, and broken down into acetyl units. Therefore, TAG need to be hydrolyzed to yield the fatty acids. This reaction is catalyzed by hormonally controlled lipase. The degradation of TAG, which is also known as lipolysis, involves two important proteins (perilipin A and epinephrine) that activate lipase enzymes. The fatty acids will be released into blood plasma; however, they are not soluble. A carrier component is needed to enable the accessibility of

other tissues to free fatty acids, so serum albumin serves this need by binding the free fatty acids and acts as carrier. It has been reported that the ratio between free acids and albumin is affected the disposition of lipid in cells. Other report mentioned that albumin may also assist the penetration of extracellular fatty acids into cells' membranes.

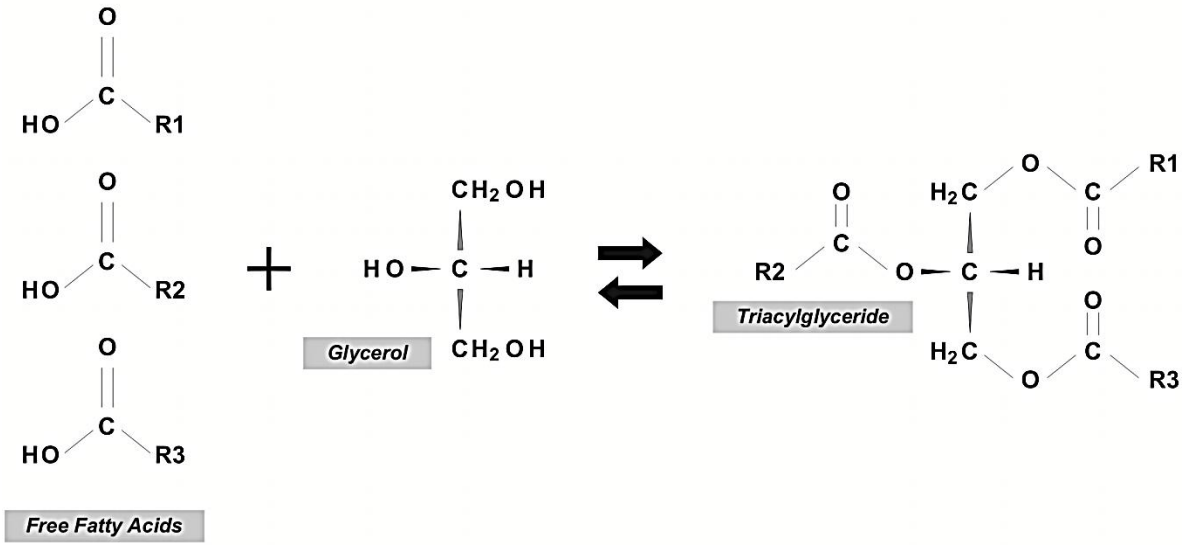

Figure 5.2. Simplified chemical reaction that explain the synthesis of triglycerides from fatty acids for energy storage and the degradation of triglyceride into fatty acid for biofuel functioning. Triglyceride is mainly stored in the lipid droplets. Fatty acid for biofuel functioning should activated, delivered, and then hydrolyzed into acetyl unit at the destination.

5.2.3 Lipid related disease

Cardiac muscle utilizes various substrates to provide energy for heart beating and endogenous myocardial TAG provides largest portion of the energy requirement. The endogenous TAG produces FA for oxidative metabolism; hence, the uptake-release mechanisms of cardiac TAG are crucial for preservation of TAG storage. However, massive accumulation of myocardial TAG is associated with cardiomyopathy and suggested that

excess TAG may be toxic [109]. The mechanism of FA uptake and the TAG synthesis in myocardial cell is in Fig. 5.3.

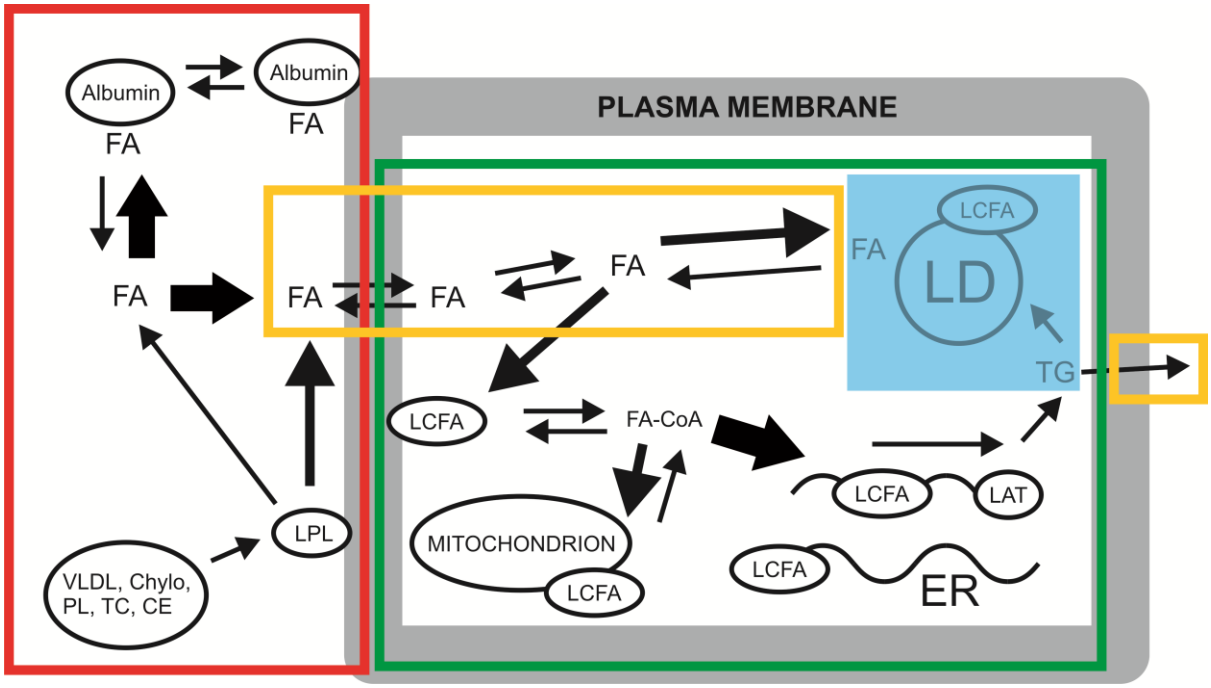

Figure 5.3. Intracellular dynamics of fatty acid. For simplification, the intracellular lipid dynamics is separated into three main metabolic pathways: Red = lipid uptake, Green = intracellular trafficking, Yellow = lipid release (either as TAG or FA), Blue render = storage of TAG and/or FA into lipid droplets.

Neutral lipid storage disorder (NLSD) was characterized by the massive accumulation of triglycerides in cellular cytoplasm [111]. Short chain and medium chain fatty acids were uptake into the LDs of fibroblast indicated with NLSD in slower rate than long chain fatty acids [112]. The degradation evaluation showed that short chain and medium chain fatty acids went through normal rate of degradation while the long chain remained undegraded. The NLSD covers divergent categories due to the systemic accumulation of TAG in cytoplasm. One subcategory of NLSD indicated with the mild myopathy and various sympthoms such as hepatomegaly, ophthalmologic symptoms, hearing loss, and mental retardation is known as NLSD with ichtyosis (NLSDI). It is associated with Chanarin-

Dorfman syndrome (CDS) is attributed to genetic mutation of CGI-58/ABHD5 indicated by the abnormal intracellular accumulation of LDs in many cells and tissues. CGI-58 produces a genetic enzyme that activates the PNPLA2/adipose triglyceride lipase (ATGL) that regulates the cellular TAG metabolism. However, the patients with NLSDI did not show the abnormality in PNPLA2. The other subcategory that shows the presence of mild myopathy, absence of ichtyosis symptom, and mutation of PNPLA2 was known as NLSD with myopathy (NLSDM).

Recently, Hirano *et al.* found a new cardiac disease which can be categorized as NLSD, known as triglyceride deposit cardiomyovasculopathy (TGCV) [113, 114]. It is indicated by the massive deposition of neutral lipid in cardiomyocytes; even though the TG concentration in blood plasma is normal. Due to its function, the heart must beat in high rate and LCFA is needed to produce adenosine triphosphate (ATP) in order to achieve maximum contractility, thus it is difficult to witness LDs containing TG under normal condition. It is also identified that patients suffer from a genetic mutation in ATGL. In comparison with other abnormality like ischemic cardiomyopathy (ICM), the TG content in TGCV tissue was notably increased, and the TG content in atheroschlerotic coronary arteries was much higher. It is important to provide a reliable method for separation of TGCV from other cardiac diseases. The facts that there are separated metabolic and transport events of lipid with slightly different structures (e.g. different length of carbon chain) [112, 115] and the capability of specific kind of lipid for treatment of heart disease or other syndromes [112, 116-118] seem to be useful for the development of therapeutic medicine and medical treatment for the patient in the future.

5.3 Lipid droplets imaging

5.3.1 Sample preparation

Adipocytes

Adipocytes are defined as fat-storing cells that are usually found throughout the vertebrate's body, which can be classified as white adipocytes and brown adipocytes. White adipocytes are more commonly found and mainly store energy. Brown adipocytes commonly found in fetuses, neonates, or hibernating animals, are responsible for producing heat by breaking down the lipid storages. However, later studies showed that the characteristic of adipocytes is more complex than the earlier understanding. Adipocytes are one of important objects in biology study for understanding intracellular processes of the fatty acid uptake and triglyceride storage as well as revealing the metabolism of the lipid by the cells due to the response to different enzymes [107, 108].

I used the 3T3-L1 cells presented as preadipocytes which did not contain any lipid droplets (LDs) in their cytoplasm. After making the subculture in preadipocytes medium (PM, ZenBio PM-1-L1) until they were confluent, I kept the cells in differentiation medium (DM, ZenBio DM-1-L1) for 3-4 days to induce the growth of lipid droplets, then the cells became the adipocytes with LDs and were stored in adipocytes medium (AM, ZenBio AM-1-L1) until they are fully matured. Figure 5.4 presents the bright field images of the adipocytes at different growth stages. Then I performed some treatments by introducing various kinds of fatty acids in corporation with albumin to observe the uptake process of each kind of lipid by the cells.

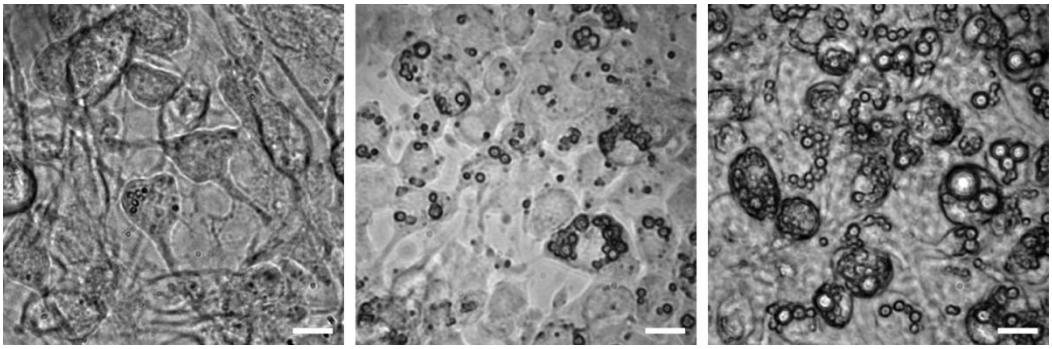

(a) (b) (c)

Figure 5.4. Bright field images of 3T3-L1 adipocytes at different growth stages: (a) preadipocytes (differentiation, DM, day 2); (b) adipocytes (early LDs growth, AM, day 1); (C) adipocytes (early LDs growth, AM, day 4). Scale bar = 20 μm

Fibroblast

Fibroblasts are typical cells that produce extracellular matrices, collagen, structural frameworks for animal tissues, and materials for wound healing. Fibroblasts can be found commonly in the connective tissues of animals. Fibroblasts have heterogeneous morphological profiles with lack of reliable and specific molecular markers to distinguish the variations of their phenotypes. Their variations are only recognized by their cellular locations. The term "blast" in cellular biology is usually used to denote a stem cell or a cell in an activated state of metabolism [119].

TGCV is occurred due to the genetic mutation of specific protein that regularizes the metabolism of the TG in the heart tissue. This kind of genetic disorders can also be detected by observing the presence of lipid droplets in leukocytes and in other tissues, including bone marrow, skin and muscle fibroblasts. I used the skin fibroblasts which were derived from patients indicated with TGCV. The cells are cultured in DMEM with 10% fetal bovine serum and 1% antibiotics, and stored in incubator chamber with 5% CO_2/37°C controlled environment. For the treatment, I introduced various kinds of fatty acids in corporation with albumin to observe the lipids uptake-release responses of the cells due to the different of fatty

acids. Figure 5.5 shows the bright field images of untreated fibroblast and treated one with deuterated stearic acid. One can easily notice that size and number of droplets structures increase. It most probably refers to the uptake of lipid into lipid droplets.

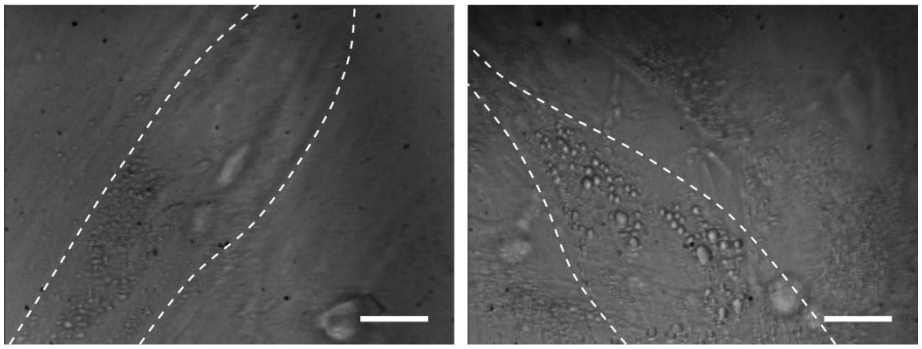

(a) (b)

Figure 5.5. Bright field image of TGCV fibroblast: (a) without any treatment and (b) with lipid treatment (deuterated stearic acid, 500 μM, 3 days). Scale bar = 20 μm. Dash line = cell boundary

Fatty acid

I prepared medium chain fatty acids/MCFA (octanoic acids) and long chain fatty acids/LCFA (stearic acids). These fatty acids were introduced to the cells to distinguish their different intracellular metabolisms. The experiment results from Hilaire *et al.* indicated a significant difference of different fatty acids incorporation to intracellular lipid in treated fibroblast. The results suggested that long chain fatty acids are accumulated much higher than short chain fatty acids or medium chain fatty acids [112]. Guo *et al.* performed similar observation and their results were on agreement with the results from Hilaire *et al* [115]. Each fatty acid was prepared as stock with concentration of 40 mM and the stock was diluted 8 times with albumin before introducing into the cells medium with desired concentration. I chose the concentration of 500 μM for treatments of cells and performed the treatment for 24 hours. To enable the tracking of the uptake, I used the deuterated form of octanoic acids and stearic acids. The deuterated structure provides a distinct detectable Raman band of the

introduced fatty acids in Raman silent region, which is free from overlapping with Raman band of biological compounds.

5.3.2 Imaging of lipid droplets by spectral CARS microscopy system

The developed CARS microscopy system using microlens array shows the capability of providing CARS images at rates faster than video rates (Chapter 3). It will give an advantage for observation of rapid biological process. Though it is still unclear, some analysis and observation tools in biological application have sensitivity of the order of several seconds to minutes [79-83]. Therefore, in term of temporal resolution, the developed system proved that a significantly faster detection can be achieved. To the best of my knowledge, the imaging rate at 100 frames per second I achieved is the fastest imaging for the microscopy system.

The spectral imaging capability is also demonstrated by observing the lipid droplets in 3T3-L1 adipocytes at the Raman shift around 2850 cm^{-1}. The results have been introduced earlier in Chapter 3. In comparison to other results, here I would like to show that for a relatively wide range tuning (from 2663.21 cm^{-1} to 3049.41 cm^{-1} or equal to ~30 nm), I completed the process without any delay for mechanical tuning. I just simply changed the wavelength using electronic control for wavelength tuning provided by AOTF. For demonstration of the ease of switching from one wavelength to another one, I performed the imaging of deuterated and non-deuterated stearic acid mixture by alternately switch the wavelength at 888 nm and 833 nm which were correlated to Raman shift of 2100 cm^{-1} (CD_2 symmetric stretching) and 2850 cm^{-1} (CH_2 symmetric stretching). I observed that the recrystallization location of each fatty acid was confirmed as well as the collocalized location of both fatty acids.

For the application in following the uptake of exogenous lipid, I observed the CARS images of untreated adipocytes and treated adipocytes with two kinds of fatty acid (deuterated octanoic acid and deuterated stearic acid). The CARS images at 2845 cm^{-1} under the different conditions above are presented in Fig. 5.6. Samples from all conditions show significant signals from intracellular lipid droplets which naturally contain fatty acid with CH bonds. However, I easily noticed that there was no lipid droplets appeared in the CARS image at 2100 cm^{-1} from untreated sample, whereas those from treated samples with either deuterated octanoic acid or stearic acid showed some lipid droplets. Naturally, there is no presence of biomolecule (not just lipid) with deuterated structure. Therefore, the CARS images at 2100 cm^{-1} should be associated to the uptaken exogenous deuterated lipid I introduced to the cell medium. However there was an appearance of a few artifacts similar to lipid droplets in CARS images at 2100 cm^{-1} from untreated sample may relate to the contribution of non-resonant background. Furthermore, the CARS images at 2100 cm^{-1} from treated samples suggest that the accumulation of deuterated stearic acid (one of the long-chain fatty acid) seems to be higher than deuterated octanoic acid (one of the medium-chain fatty acid). In particular, the CARS images at 2100 cm^{-1} and 2845 cm^{-1} from treated sample with deuterated stearic acid indicate some lipid droplets that contain only the fatty acid with CD bonds and CH bonds (Fig 5.7). I set the power of pump and Stokes beams before the microscope to the value of 220 mW and 450 mW, respectively.

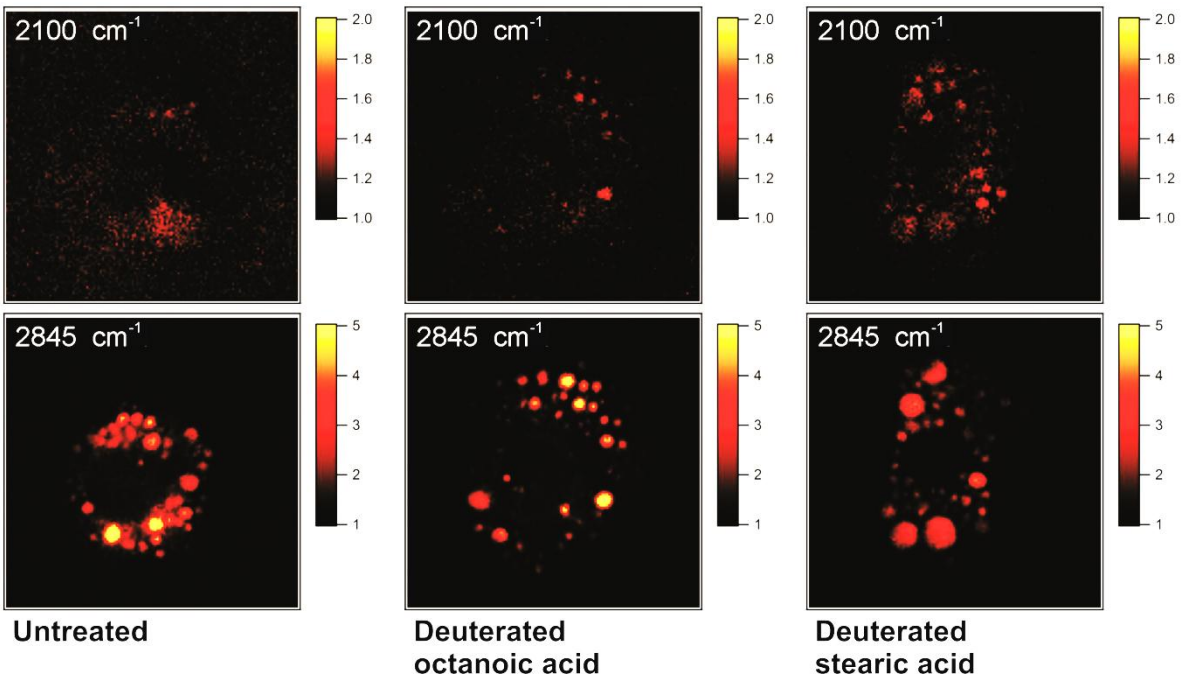

Figure 5.6. CARS images of 3T3-L1 adipocytes: untreated (left column), treated with deuterated octanoic acid (middle column), and treated with deuterated stearic acid (right column). CARS images were acquired at 2100 cm^{-1} and 2845 cm^{-1}, attributed to CD_2 symmetric stretching and CH_2 symmetric stretching vibrations.

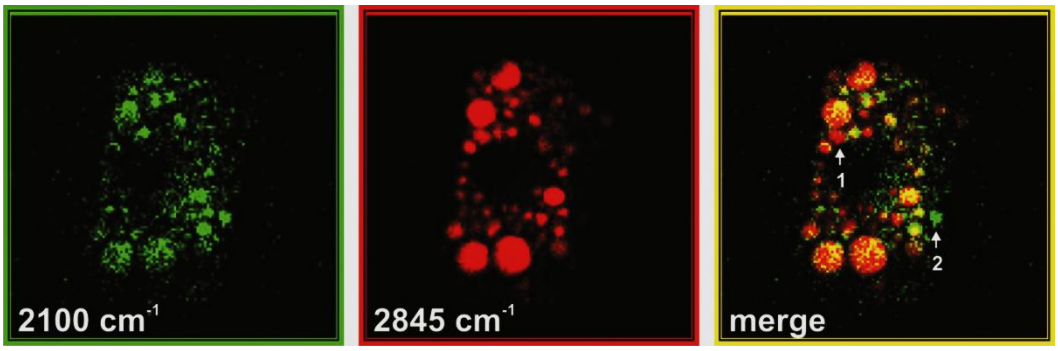

Figure 5.7. CARS images from 3T3-L1 adipocytes treated with deuterated stearic acid shows the presence of lipid droplets that contain only non-deuterated lipid (indicated by no. 1 on the merge image) and deuterated lipid (indicated by no. 2 on the merge image). The appearance of intracellular deuterated lipid can only be induced by the accumulation of exogenous deuterated lipid.

Due to the results of 3T3-L1 adipocytes, I proceeded to observe the TGCV fibroblasts under conditioning and then acquired the CARS images at 2100 cm^{-1} and 2850 cm^{-1} (Fig 5.8). I obtained similar results with the experiment using 3T3-L1 adipocytes. It may indicate that it

is the general behavior of intracellular lipid uptake [109, 110]. The increase of lipid droplets size noticed in the CARS images at 2850 cm^{-1} from the treated samples may imply the disorder of lipid storage occurred in TGCV fibroblasts. However, accumulation of deuterated stearic acid is significantly higher than deuterated octanoic acid may indicate their different metabolic pathways. As some studies found that medium-chain fatty acid seems to be potential for treatment of some lipid-related diseases [112, 116-118], the results here may have relation with these studies. I also set the power of pump and Stokes beams before the microscope to the value of 220 mW and 450 mW, respectively.

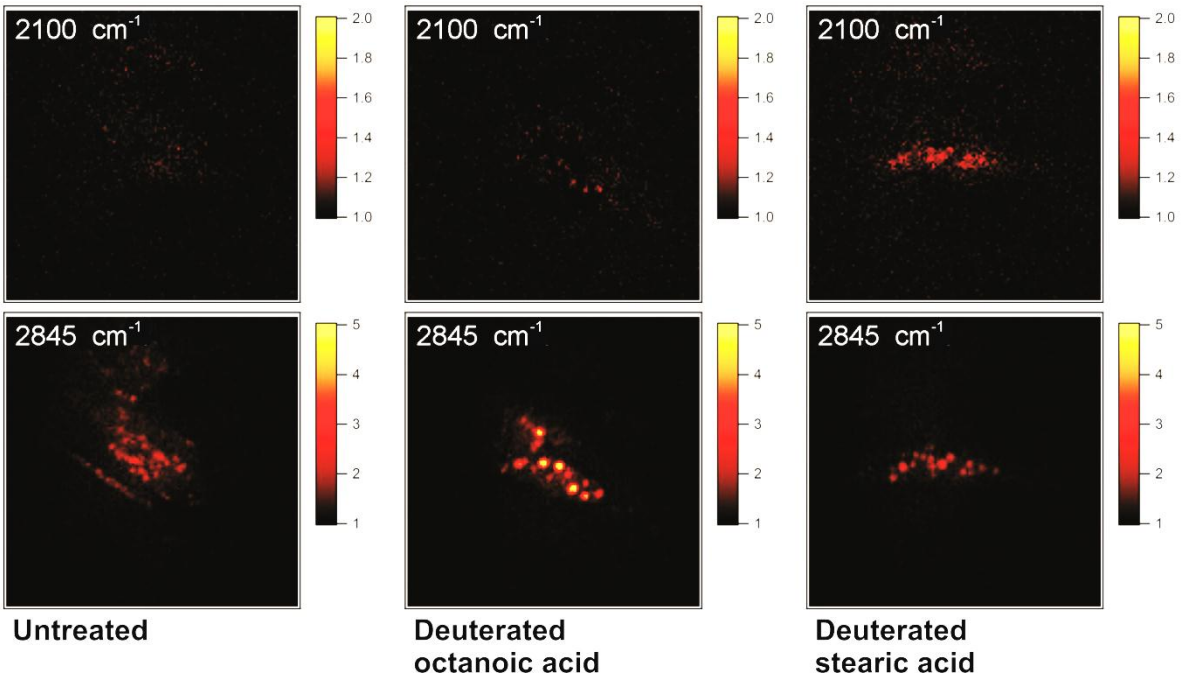

Figure 5.8. CARS images of TGCV fibroblasts: untreated (left column), treated with deuterated octanoic acid (middle column), and treated with deuterated stearic acid (right column). CARS images were acquired at 2100 cm^{-1} and 2845 cm^{-1}, attributed to CD_2 symmetric stretching and CH_2 symmetric stretching vibrations.

5.3.3 Imaging of lipid droplets by spectral SRS microscopy system

The fact that SRS microscopy surpasses CARS microscopy in term of non-resonant background contribution has been demonstrated in Chapter 4. Images shown at the Raman shift of 2300 cm^{-1} which assigned to non-resonant vibration, should be free from any signal from biological sample. However, the CARS images showed distinct structures of lipid droplets and this finding supports the results of CARS experiments explained in the previous subsection which also suggested the contribution of non-resonant background.

The used of AOTF laser in the developed spectral SRS microscopy system enables the coverage over significantly wide region. In Chapter 4 I presented the spectral SRS imaging over Raman shift region between 2650 cm^{-1} and 3050 cm^{-1}. I then achieved a greatly extend of the coverage region for the spectral imaging which stretch from 2100 cm^{-1} and 3200 cm^{-1}. The images shown in Fig. 5.9 were chosen to represent the achievement of large coverage region. The Raman shift of the images shown are assigned to CD_2 stretching (2100 cm^{-1}), off-resonant (2300 cm^{-1} and 2600 cm^{-1}), CH_2 stretching (2850 cm^{-1}), CH_3 stretching (2900 cm^{-1}), and OH (3200 cm^{-1}). These Raman shift are associated with the accumulated deuterated lipid (CD_2 stretching), intracellular lipid (CH_2 stretching and CH_3 stretching), and environment around the cell which is dominated by water (OH). These results show the advantage of AOTF laser as tunable laser source for SRS microscopy and other CRS microscopy. The tuning over this coverage region was performed by simply change the wavelength of AOTF laser electrically under synchronization condition with other picosecond laser.

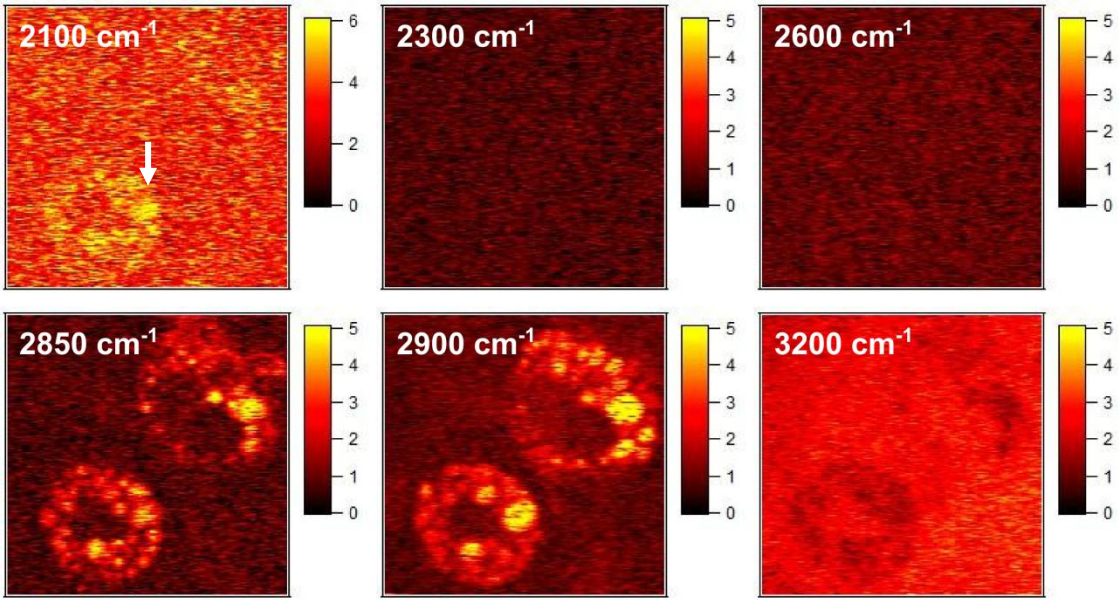

Figure 5.9. Spectral SRS images over wide-range tuning from 2100 cm^{-1} to 3200 cm^{-1}, the displayed SRS images is selected due to their relation to specific molecular vibrations: 2100 cm^{-1} (CD_2 stretching = accumulated deuterated lipid), 2300 cm^{-1} and 2600 cm^{-1} (off-resonant), 2850 cm^{-1} and 2900 cm^{-1} (CH_2 stretching and CH_3 stretching = non-deuterated lipid, intracellular lipid), and 3200 cm^{-1} (OH = water, cell environment). White arrow = weak SRS signal of CD_2 stretching from accumulated deuterated lipid. Sample = 3T3-L1 adipocytes treated with deuterated stearic acid

I also demonstrated the spectral SRS imaging in the finger in the fingerprint region. I observed the lipid droplets in the 3T3-L1 adipocytes around Raman shift of CH_2 stretching at 1440 cm^{-1}. Figure 5.10 a-c show spectral SRS images at 1387.44 cm^{-1}, 1439.62 cm^{-1}, and 1453.46 cm^{-1} and the reconstructed spectral profile is shown in Figure 5.10 d. For lipid study, the observation in the fingerprint region is important for discrimination of lipid subspecies. Even though some peaks of the molecular vibrations may overlap in the fingerprint region, one can overcome this problem by observation of multiple peaks. A biochemical compound may have some signatures in the fingerprint region as they consist of various chemical bonds.

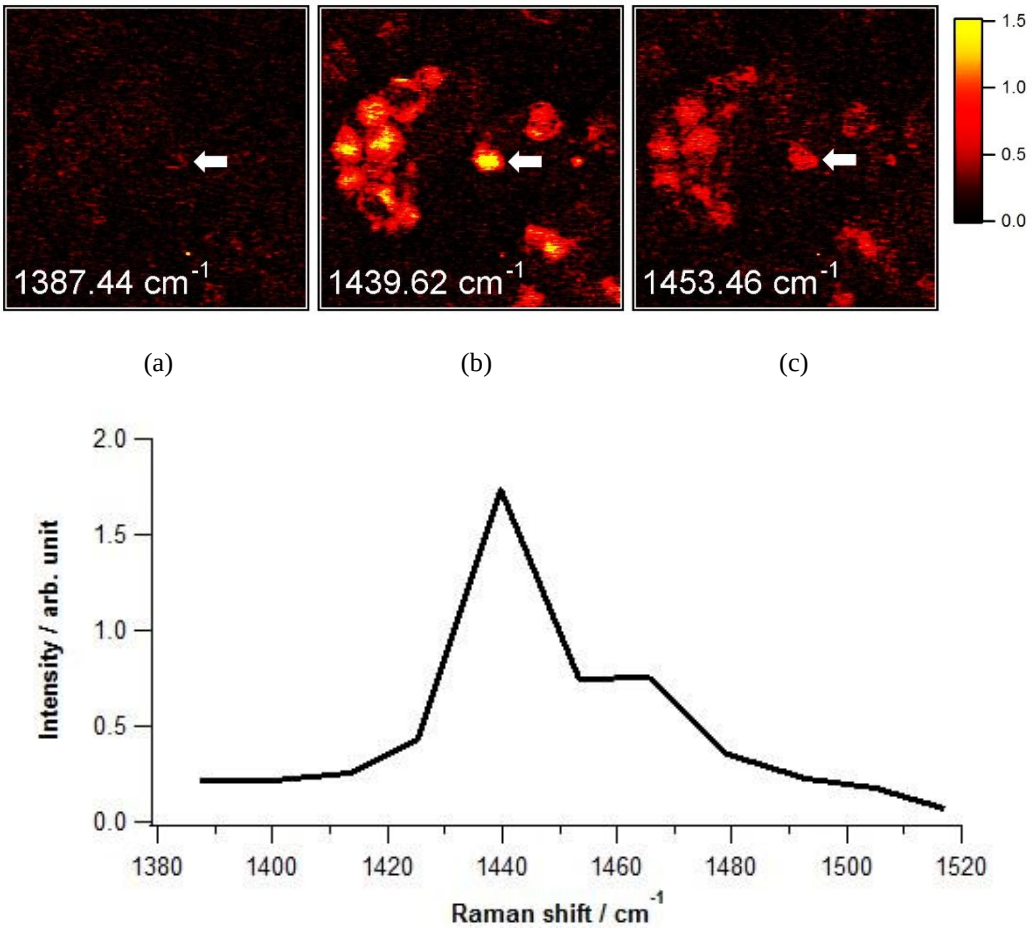

Figure 5.10. Spectral SRS images of adipocytes at (a) 1387.44 cm^{-1}, (b) 1439.62 cm^{-1}, and (c) 1453.46 cm^{-1}, taken with spectral SRS imaging system. The peak around 1440 cm^{-1} is related to asymmetric stretching vibration of CH bond in lipid. Acquisition time = 2.5 s/image. (d) SRS spectral profile reconstructed from area of interest indicated by white arrow in a–c (averaged over 10×10 pixels).

Having a wide-range tunability, the spectral SRS microscopy using AOTF laser is also capable of the ease of switching from one wavelength to another one for imaging of two significantly separated Raman shift. I observed the treated 3T3-L1 adipocytes with deuterated stearic acid (Fig 5.11 a-b) by alternately switch the wavelength at 888 nm and 833 nm which are correlated to Raman shift of 2100 cm^{-1} (CD_2 symmetric stretching vibration from deuterated stearic acid) and 2850 cm^{-1} (CH_2 symmetric stretching vibration from existed intracellular lipid). The acquisition time for SRS images is still relatively long; however, it is

caused by the sensitivity limit of the detector system rather than the slow wavelength tuning. The performance of the AOTF laser to perform fast wavelength tuning under synchronization is still maintained well (Fig. 5.12).

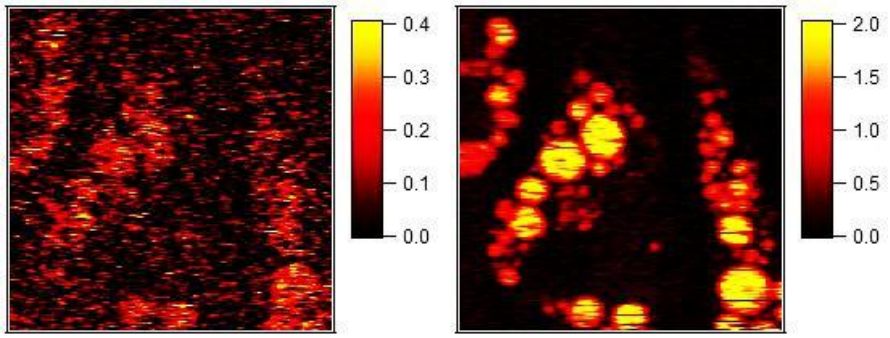

(a) (b)

Figure 5.11. Switching SRS images from 3T3-L1 adipocytes treated with deuterated stearic acid at (a) 2100 cm^{-1} and (b) 2850 cm^{-1}, assigned to CD_2 and CH_2 symmetric stretching vibrations. Imaging time = 2.5 s/image.

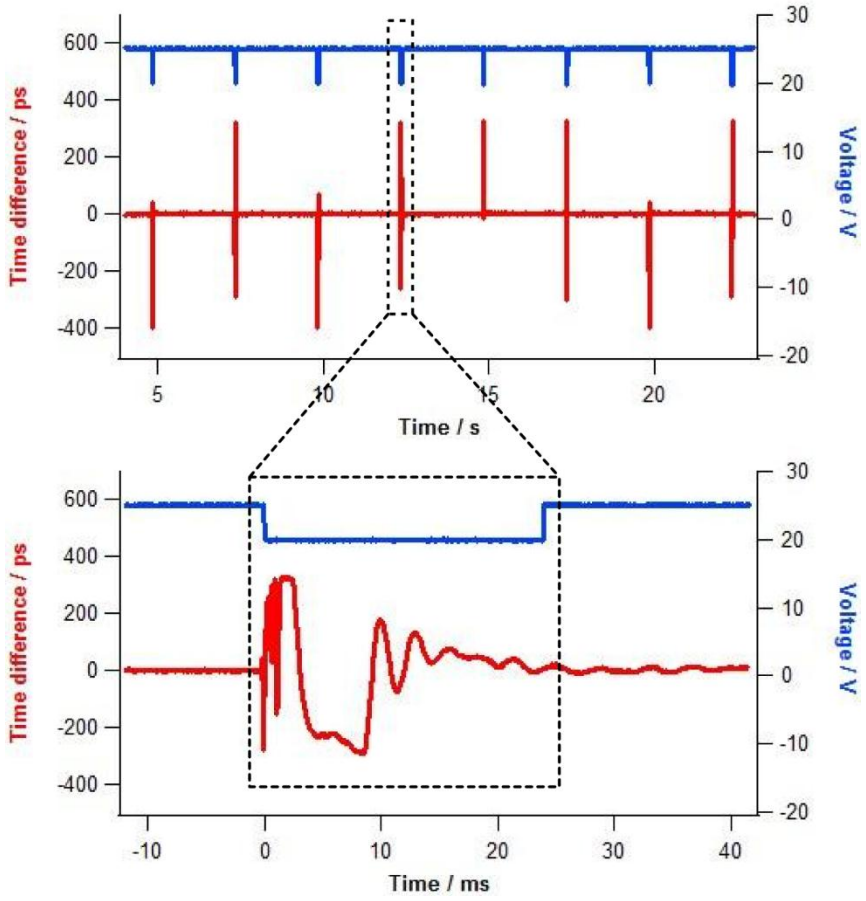

Figure 5.12. The trigger signal (blue) and synchronization signal (red) in the spectral SRS microsopy system during the alternately switched between 833 nm and 888 nm (equal to 2100 cm^{-1} and 2850 cm^{-1}). The AOTF starts the wavelength change when it receives a trigger signal. After change the wavelength, the timing jitter between AOTF laser and the other picosecond laser became notably large; however, feedback control system (it has been explained in Chapter 2) attempts to reduce the timing jitter and the successfully recovers the synchronization within around 20 ms. Upper graph = series of trigger signal and synchronization signal during the alternate switching of CD/CH. Bottom graph = magnification of one event wavelength change.

5.4 Summary

The applications of CRS microscopy (CARS and SRS) for biological imaging, especially for intracellular lipid study, have been shown here. The developed CRS microscopy which is equipped with high-speed tunable laser is feasible for spectral imaging purpose. Fair spectral images and reconstructed spectral profiles are achieved from the

spectral imaging of lipid droplets in the CH vibration region. Additionally, I also acquired a remarkable wide-range tuning over 1000 cm^{-1} and fast switching between two significantly separated Raman shift (in this case, 2100 cm^{-1} assigned to CD_2 symmetric stretching and 2850 cm^{-1} assigned to CH_2 symmetric stretching).

The observation of lipid uptake from two types of lipid reveals the possible existence of their different metabolic pathways. It is also demonstrated the significant accumulation of lipid by the fibroblasts which may relate to the indication of lipid storage disorder. On the other hand, the results also show that certain lipid was less accumulated so that it has a potential for treatment of lipid-related disease.

Conclusion

This dissertation has presented the development of hyperspectral coherent Raman scattering (CRS) microscopy using a high-speed tunable picosecond laser and its application for intracellular lipid imaging. The new laser system that was developed to enable fast spectral imaging using CRS microscopy provided an ease in wavelength tuning over wide range. After every wavelength change, the synchronization was recovered within 20 ms. The fast spectral CARS microscopy system using the high-speed tunable laser successfully obtained movies with acquisition rates of 10 ms/image, faster than video rates. For further development, I constructed spectral SRS microscopy system that was insensitive to the non-resonant background as CARS microscopy was. Wide spectral range of ~400 cm^{-1} was achieved by spectral CARS microscopy which covered the whole area of CH vibration. The spectral SRS microscopy demonstrated a quiet notable range of ~1000 cm^{-1} which included the silent region and the CH vibration region. I applied the fast spectral CARS microscopy and spectral SRS microscopy both with the high-speed tunable laser as one of the sources for observation of lipid uptake by cells.

The CARS images of untreated and treated adipocytes revealed that naturally there is no presence of deuterated structure in the cells. Therefore, any signal generated at Raman shifts 2100 cm^{-1} should correspond to the uptake of exogenous lipid which had deuterated structure. By comparing the CARS images of treated adipocytes by deuterated octanoic acid and deuterated stearic acid suggested that both lipids seemed to follow different metabolic pathways which resulted in the different accumulation in the cells. Further results on the CARS images of treated adipocytes by deuterated stearic acid revealed that the penetration of

deuterated lipid to lipid droplets was different. Under the same treatment conditions, TGCV fibroblasts provided similar results. However, the accumulation of lipid in TGCV cells was induced by the abnormality of lipid storage rather than by lipid storage mechanism.

The capability of fast image acquisition and wide spectral range tunability by the fast spectral CRS microscopy system will be useful for the application of time course imaging in observation of biological process dynamics. In particular, the observation of lipid uptake by the TGCV fibroblasts still remains challenging since the size of lipid droplets in TGCV fibroblasts is relatively small. Recent advanced in other modality, especially the techniques for super resolution imaging, can be the key factor for the enhancement of spectral CRS microscopy. Additionally, considering the challenge for suitable application in biological field or other study may also encourage the improvement of CRS microscopy.

Finally, this dissertation demonstrated the potential of hyperspectral CRS microscopy using high-speed tunable laser for biomolecular imaging. The AOTF laser system which facilitates a rapid tuning capability and synchronization with another laser may be one of the key points for development of spectral imaging, especially for application in molecular dynamics observation in biology and medicine.

Acknowledgement

This study was carried out at Araki Laboratory, Department of Mechanical Science and Bioengineering, Graduate School of Engineering Science, Osaka University. I would like to express my appreciations to all people who helped me in completing this dissertation.

First of all, I would like to express the deepest gratitude to my supervisor Prof. Dr. Tsutomu Araki in Graduate School of Engineering Science, Osaka University, for giving me recommendation to enter this Doctoral Course study, for supervising my three years' worth of studies, for giving me the opportunity to work in the laboratory, for providing outstanding working conditions, and for his academic advices and supports. The experiences in the laboratory are a great treasure for me and I believe they will be a valuable asset for my future.

I also would like to sincerely thank Assoc. Prof. Dr. Mamoru Hashimoto in Graduate School of Engineering Science, Osaka University, for his guidance, comments, and supports throughout the studies and experiments. He always encouraged me in group meetings, enriched me with priceless skills in technical writings, ways of thinking in study, and so on.

I am honoured to have Prof. Dr. Jun Miyake and Prof. Dr. Osamu Oshiro (both in Graduate School of Engineering Science, Osaka University) as the review committee. From fruitful discussions I benefit corrections and improvements during the preparation of this disertation. They also carefully and thoroughly evaluate my disertation with questions, suggestions, criticisms, and advices.

I would like to appreciate Assoc. Prof. Dr. Shuichiro Fukushima in Graduate School of Engineering Science, Osaka University for his comments, suggestions, discussions, and supports on the works with the biological specimens and treatments.

I would like to thank to Dr. Hirohiko Niioka in Graduate School of Engineering Science, Osaka University, for his comments, suggestions, discussions, and encouragements during my studies.

I would like to acknowledge Prof. Dr. Takeshi Yasui and Mr. Yoshiyuki Sakaguchi in Graduate School of Engineering Science, Osaka University for their comments, suggestions, and technical supports in the laboratory. Prof. Dr. Yasui gave me valuable comments and discussions for my study. Mr. Sakaguchi supports me with a lot of technical guidances of mechanical works.

Prof. Dr. Ken-ichi Hirano in Graduate School of Medicine, Osaka University kindly provided me with the fibroblast from TGCV patient for my experiment under the permission from Research Ethics Committee Osaka University.

In the conferences, I have chances to meet great people who are friendly and helpful. I got valuable ideas and suggestions for my study, and improved the quality of my research.

I was a graduate from Bandung Institute of Technology (ITB), Indonesia, back then when I was struggling to get an opportunity for Doctoral Course study. I had a great interest in optics and its application for biomedical. My supervisors in Indonesia, Dr. Andrianto Handojo, Dr. Deddy Kurniadi, and Dr. Endang Juliastuti always gave me encouragement for pursuing to study abroad for enhancement of my experiences and skills.

In 2010, I came to Osaka University as a Doctoral student with lacks of knowledge and experience about advance optical setup. I have to say that three years is a very short time for me to learn many new, interesting things here. Throughout the project, I have been well supported by Araki laboratory members. Their discussions, comments, encouragements, and private supports were very important in the laboratory life, and the work in this dissertation would not happen without their supports. I would like to thank to all the members and ex-members of this laboratory, especially Dr. Takeo Minamikawa, Mr. Junichi Iwatsuka, Mr.

Kouhei Ikeda, and Mr. Naokazu Matsumura who directly worked with me over the project in the laboratory.

In late 2010, I joined The Optical Society of America (OSA) and The Society of Photographic Instrumentation Engineering (SPIE) student chapter of Osaka University. I have many great experiences through the events, meetings, scientific seminars, the Photonics Student Club, and so on. The communications and experiences are invaluable in my Ph.D student life, and many thanks to the OSA/SPIE student chapter members.

I was financially supported by the scholarship from Ministry of Education, Culture, Sports, Science and Technology (MEXT) through all these three years.

I would also like to thank all my friends for their support in my daily life. Especially, the Indonesian Catholic community in Kansai, a place where I can still get a taste of being home. I also get a valuable experience for learning the way of teamwork and management.

Last and most importantly, I would like to send my deepest gratitude and respects to my parents, Tonny and Gatty, who will never give up to encourage and support me to made my studies and every other things in my life possible. Also big thanks to my dearest siblings, Hartini and Hartono, for their kind, valuable encouragements and supports.

As many people said that going abroad is a really precious experience to open our minds and interact with peoples from different backgrounds. The daily life in the laboratory, school environment, and society around were a blend of great taste for life I will never forget in my life time. Acquiring doctoral degree is just a start of new stage in my life. This quite simple yet meaningful quote “With great power, comes great responsibility” will always remind me to continue my contribution to the world.

References

[1] J. M. Berg, J. L. Tymoczko, L. Stryer, *Biochemistry* (W. H. Freeman and Company, USA, 2007).

[2] B. Alberts, *Molecular biology of cell* (Garland Science, USA, 2008).

[3] X. S. Xie, J. Yu, W. Y. Yang, "Living cells as test tubes," *Science* **312**, 228–230 (2006).

[4] X. Cui, M. Lew, C. Yang, "Quantitative differential interference contrast microscopy based on structured-aperture interference," *Appl. Phys. Lett.* **93**, 091113-1–3 (2008).

[5] C. L. Curl, C. J. Bellair, P. J. Harris, B. E. Allman, A. Roberts, K. A. Nugent, L. M. D. Delbridge, "Quantitative phase microscopy – a new tool for investigating the structure and function of unstained live cells," *Proc. Aust. Physiol. Pharmacol. Soc.* **34**, 121–127 (2004).

[6] J. R. McIthosh "Electron microscopy of cells: A new beginning for a new century," *J. Cell Biol.* **153**, F25-F32 (2001).

[7] Y. F. Dufrene, "Towards nanomicrobiology using atomic force microscopy," *Nat. Rev Microbiol* **6**, 674–680 (2008).

[8] X. Nan, J. X. Cheng, X. S. Xie, "Vibrational imaging of lipid droplets in live fibroblast cells with coherent anti-Stokes Raman scattering microscopy," *J. Lipid. Res.* **44.** 2202–2208 (2003).

[9] G. J. Puppels, F. F. M. de Mul, C. Otto, J. Greve, M. Robert-Nicoud, D. J. Arndt-Jovin, T. M. Jovin, "Studying single living cells and chromosomes by confocal Raman microspectroscopy," *Nature*, **347**, 301-303 (1990).

[10] K. Hamada, K. Fujita, N. I. Smith, M. Kobayashi, Y. Inouye, S. Kawata, "Raman microscopy for dynamic molecular imaging of living cells," *J. Biomed. Opt.*, **13**, 044027-1–4 (2008).

[11] R. W. Boyd, *Nonlinear optics* (Academic Press, USA, 2008).

[12] M. D. Levenson, *Introduction to nonlinear laser spectroscopy* (Academic Press, USA, 1982).

[13] M. D. Duncan, J. Reintjes, and T. J. Manuccia, "Scanning coherent anti-Stokes Raman microscope," *Opt. Lett.* **7**, 350–352 (1982).

[14] A. Zumbusch, G. R. Holtom, X. S. Xie, "Three-dimensional vibrational imaging by coherent anti-Stokes Raman scattering," *Phys. Rev. Lett.* **82**, 4142–4145 (1999).

[15] M. Hashimoto, T. Araki, S. Kawata, "Molecular vibration imaging in the fingerprint region by use of coherent anti-Stokes Raman scattering microscopy with collinear configuration," *Opt. Lett.* **25**, 1768–1770 (2000).

[16] W. M. Tolles, J. W. Nibler, J. R. McDonald, A. B. Harvey, "A review of the theory and application of coherent anti-Stokes Raman spectroscopy (CARS)," *Appl. Spectrosc.* **31**, 253–271 (1977).

[17] A. M. Zheltikov, "Coherent anti-Stokes Raman scattering: From proof-of-the-principle experiments to femtosecond CARS and higher order wave-mixing generalizations," *J. Raman Spectrosc.* **31**, 653–667 (2000).

[18] M. Hashimoto, T. Araki, "Three-dimensional transfer function of coherent anti-Stokes Raman scattering microscopy," *J. Opt. Soc. Am. A* **18**, 771–776 (2001).

[19] P. Nandakumar, A. Kovalev, A. Volkmer, "Vibrational imaging based on stimulated Raman scattering microscopy," *New J. Phys.* **11**, 033026-1–9 (2009).

[20] C. W. Freudiger, W. Min, B. G. Saar, S. Lu, G. R. Holtom, C. He, J. C. Tsai, J. X. Kang, X. S. Xie, "Label-free biomedical imaging with high sensitivity by stimulated Raman scattering microscopy," *Science* **322**, 1857–1861 (2008).

[21] Y. Ozeki, W. Umemura, Y. Otsuka, S. Satoh, H. Hashimoto, K. Sumimura, N. Nishizawa, K. Fukui, K. Itoh, "High-speed molecular spectral imaging of tissue with stimulated Raman scattering," *Nat. Photon.* **6**, 845–851 (2012).

[22] C. W. Freudiger, M. B. J. Roeffaers, X. Zhang, B. G. Saar, W. Min, X. S. Xie, "Optical heterodyne-detected Raman-induced Kerr effect (OHD-RIKE) microscopy," *J. Phys. Chem. B* **115**, 5574–5581 (2011).

[23] C. Y. Chung, J. Hsu, S. Mukamel, E. O. Potma, "Controlling stimulated coherent spectroscopy and microscopy by a position-dependent phase," *Phys. Rev. A* **87**, 033833-1–6 (2013).

[24] B. E. A. Saleh, M. C. Teich, *Fundamentals of photonics* (John Wiley & Sons, Inc., SINGAPORE, 2007).

[25] C. L. Evans, E. O. Potma, M. Pouris'haag, D. Coté, C. P. Lin, X. S. Xie, "Chemical imaging of tissue in vivo with video-rate coherent anti-Stokes Raman scattering microscopy," *Proc. Nat. Acad. Sci.USA* **102**, 16807–16812 (2005).

[26] F. Ganikhanov, S. **Carrasco**, X. S. **Xie**, M. **Katz**, W. **Seitz, D. Kopf,** "Broadly tunable dual-wavelength light source for coherent anti-Stokes Raman scattering microscopy," *Opt. Lett.* **31**, 1292–1294 (2006).

[27] C. Y. Lin, J. L. Suhalim, C. L. Nien, M. D. Miljković, M. Diem, J. V. Jester, E. O. Potma, "Picosecond spectral coherent anti-Stokes Raman scattering imaging with

principal component analysis of meibomian glands," *J. Biomed. Opt.* **16**, 021104-1–9 (2011).

[28] Y. Ozeki, F. Dake, S. Kajiyama, K. Fukui, K. Itoh, "Analysis and experimental assessment of the sensitivity of stimulated Raman scattering microscopy," *Opt. Expr.* **17,** 3651–3658 (2009).

[29] L. Kong, M. Ji, G. R. Holtom, D. Fu, C. W. Freudiger, X. Sunney Xie "Multicolor stimulated Raman scattering microscopy with a rapidly tunable optical parametric oscillator," *Opt. Lett.* **38**, 145–147 (2013).

[30] D. Fu, G. R. Holtom, C. W. Freudiger, X. Zhang, X. S. Xie, "Hyperspectral imaging with stimulated Raman scattering by chirped femtosecond lasers," *J. Phys. Chem. B* **117**, 4634−4640 (2013).

[31] J. X. Cheng, A. Volkmer, L. D. Book, X. S. Xie, "Multiplex coherent anti-Stokes Raman scattering microspectroscopy and study of lipid vesicles," *J. Phys. Chem. B* **106**, 8493–8498 (2002).

[32] K. P. Knutsen, J. C. Johnson, A. E. Miller, P. B. Petersen, R. J. Saykally, "High spectral resolution multiplex CARS spectroscopy using chirped pulses," *Proc. of SPIE* **5323**, 230–239 (2010).

[33] C. W. Freudiger, W. Min, G. R. Holtom, B. Xu, M. Dantus, X. S. Xie, "Highly specific label-free molecular imaging with spectrally tailored excitation-stimulated Raman scattering (STE-SRS) microscopy," *Nature Photon* **5**, 103–109 (2011).

[34] M. Okuno, H. Kano, P. Leproux, V. Couderc, H. Hamaguchi, "Ultrabroadband multiplex CARS microspectroscopy and imaging using a subnanosecond supercontinuum light source in the deep near infrared," *Opt. Lett.* **33**, 923–925 (2008).

[35] E. R. Andresen, H. N. Paulsen, V. Birkedal, J. Thøgersen, S. R. Keiding, "Broadband multiplex coherent anti-Stokes Raman scattering microscopy employing photonic-crystal fibers," *J. Opt. Soc. Am. B* **22**, 1934–1938 (2005).

[36] Y. Ozeki, W. Umemura, K. Sumimura, N. Nishizawa, K. Fukui, and K. Itoh, "Stimulated Raman hyperspectral imaging based on spectral filtering of broadband laser pulses," *Opt. Lett.* **37**, 431–433 (2012).

[37] A. Volkmer, J. X. Cheng, X. S. Xie, "Vibrational imaging with high sensitivity via epidetected coherent anti Stokes Raman scattering microscopy," *Phys. Rev. Lett.* **87**, 23901-1–4 (2001).

[38] M. N. Slipchenko, H. Chen, D. R. Ely, Y. Jung, M. T. Carvajal, J. X. Cheng, "Vibrational imaging of tablets by epi-detected stimulated Raman scattering microscopy," *Analyst* **135**, 2613–2619 (2010).

[39] J. X. Cheng, L. D. Book, X. S. Xie, "Polarization coherent anti-Stokes Raman scattering microscopy," *Opt. Lett.* **26**, 1341–1343 (2001).

[40] A. Volkmer, L. D. Book, X. S. Xie, "Time-resolved coherent anti-Stokes Raman scattering microscopy: Imaging based on Raman free induction decay," *Appl. Phys. Lett.* **80**, 1505–1507 (2002).

[41] E. O. Potma, C. L. Evans, X. S. Xie, "Heterodyne coherent anti-Stokes Raman scattering microscopy," *Opt. Lett.* **31**, 241–243 (2006).

[42] Y. X. Fan, R. C. Eckardt, B. L. Byer, C. T. Chen, A. D. Jiang, "Barium borate optical parametric oscillator," *J. Quant. Electr.* **25**, 1196–1198 (1989).

[43] Z. Sun, M. Ghotbi, and M. Ebrahim-Zadeh, "Widely tunable picosecond optical parametric generation and amplification in BiB_3O_6," *Opt. Expr.* **15**, 4139–4148 (2007).

[44] M. Towrie, A. W. Parker, W. Shaikh, P. Matousek, "Tunable picosecond optical parametric generator-amplifier system for time resolved Raman spectroscopy," *Meas. Sci. Tech.* **9**, 816–823 (1998).

[45] A. Shirakawa, T. Kobayashi, "Noncollinearly phase-matched femtosecond optical parametric amplification with 2000 cm^{-1} bandwidth," *Appl. Phys. Lett.* **72**, 147–149 (1998).

[46] P. E. Powers, K. W. Aniolek, T. J. Kulp, B. A. Richman, S. E. Bisson, "Periodically poled lithium niobate optical parametric amplifier seeded with the narrowband filtered output of an optical parametric generator," *Opt. Lett.* **23**, 1886–1888 (1998).

[47] G. Arisholm, O. Nordseth, G. Rustad, "Optical parametric master oscillator and power amplifier for efficient conversion of high-energy pulses with high beam quality," *Opt. Expr.* **12**, 4189–4197 (2004).

[48] M. V. Alampiev, O. F. Butyagin, "Angular and temperature tuning characteristic of an optical parametric oscillator based on $KTiOPO_4$ crystal," *J. Quant. Electr.* **28**, 334–336 (1998).

[49] E. O. Potma, D. J. Jones, J. X. Cheng, X. S. Xie, J. Ye, "High-sensitivity coherent anti-Stokes Raman scattering microscopy with two tightly synchronized picosecond lasers," *Opt. Lett.* **27**, 1168–1170 (2002).

[50] I. Iparraguirre, I. Aramburu, J. Azkargorta, M. A. Illarramendi, "Wavelength tuning of Titanium Sapphire Laser by its own crystal birefringence," *Opt. Expr.* **13**, 1254–1259 (2005).

[51] M. Baumgartl, M. Chemnitz, C. Jauregui, T. Meyer, B. Dietzek, J. Popp, J. Limpert, A. Tünnermann, "All-fiber laser source for CARS microscopy based on fiber optical parametric frequency conversion", *Opt. Exp.*, **20**, 4484–4493 (2012).

[52] T. Hellerer, C. Axäng, C. Brackmann, P. Hillertz, M. Pilon, A. Enejder, "Monitoring of lipid storage in Caenorhabditis elegans using coherent anti-Stokes Raman scattering (CARS) microscopy," *Proc. Nat. Acad. Sci. USA* **104**, 14658–14663 (2007).

[53] T. T. Le, S. Yue, J. X. Cheng, "Shedding new light on lipid biology with coherent anti-Stokes Raman scattering microscopy," *J. Lipid Res.*, **51**, 3091–3102 (2010).

[54] M. Paar, C. Jüngst, N. A. Steiner, C. Magnes, F. Sinner, D. Kolb, A. Lass, R. Zimmermann, A. Zumbusch, S. D. Kohlwein, H. Wolinski, "Remodeling of lipid droplets during lipolysis and growth in adipocytes", *J. Biol. Chem.*, **287**, 11164–11173 (2012).

[55] E. Kang, J. Robinson, K. Park, J. X. Cheng, "Paclitaxel distribution in poly(ethylene glycol)/poly(lactide-co-glycolic acid) blends and its release visualized by coherent anti-Stokes Raman scattering microscopy," *J. Con. Rel.* **122**, 261–268 (2007).

[56] P. Xu, E. Gullotti, L. Tong, C. B. Highley, D. R. Errabelli, T. Hasan, J. X. Cheng, D. S. Kohane, Y. Yeo, "Intracellular drug delivery by poly(lactic-co-glycolic acid) nanoparticles, Revisited," *Mol. Pharm.* **6**, 190–201 (2009).

[57] M. Windbergs, M. Jurna, H. L. Offerhaus, J. L. Herek, P. Kleinebudde, C. J. Strachan, "Chemical imaging of oral solid dosage forms and changes upon dissolution using coherent anti-Stokes Raman scattering microscopy," *Anal. Chem.* **81**, 2085–2091 (2009).

[58] S. Begin, B. Burgoyne, V. Mercier, A. Villeneuve, R. Vallée, D. Côté, "Coherent anti-Stokes Raman scattering hyperspectral tissue imaging with a wavelength-swept system," *Biomed. Opt. Expr.* **2**, 1296–1306 (2011).

[59] W. Dou, D. Zhang, Y. Jung, J. X. Cheng, D. M. Umulis, "Label-free imaging of lipid-droplet intracellular motion in early *Drosophila* embryos using femtosecond-stimulated Raman loss microscopy," *Biophys. J.* **102**, 1666–1675 (2012).

[60] M. N. Slipchenko, T. T. Le, H. Chen, J. X. Cheng, "High-speed vibrational imaging and spectral analysis of lipid bodies by compound Raman microscopy," *J. Phys. Chem. B* **113**, 7681–7686 (2009).

[61] X. Zhang, M. B. J. Roeffaers, S. Basu, J. R. Daniele, D. Fu, C. W. Freudiger, G. R. Holtom, X. S. Xie, "Label-free live-cell imaging of nucleic acids using stimulated Raman scattering microscopy," *Chem. Phys. Chem.* **13**, 1054–1059 (2012).

[62] B. G. Saar, L. R. Contreras-Rojas, X. S. Xie, R. H. Guy, "Imaging Drug Delivery to Skin with Stimulated Raman Scattering Microscopy," *Mol. Pharm.* **8**, 969–975 (2011).

[63] S. Sunder, R. Mendelsohn, H.J. Bernstein, "Raman studies of the C-H and C-D stretching regions in stearic acid and some specifically deuterated derivatives" *Chem. Phys. Lipids* **17**, 456–465 (1976).

[64] B.P. Gaber, P. Yager, W.L. Peticolas, "Deuterated phospholipids as nonpertubating components for Raman studies of biomembranes," *Biophys. J.* **22**, 191–207 (1978).

[65] C. Matthäus, A. Kale, T. Chernenko, V. Torchilin, M. Diem, "New ways of imaging uptake and intracellular fate of liposomal drug carrier systems inside individual cells, based on Raman microscopy" *Mol. Pharm.* **5**, 287–293 (2008).

[66] M. Noestheden, Q. Hu, L.L. Tay, A.M. Tonary, A. Stolow, R. MacKenzie, J. Tanha, J.P. Pezacki, "Synthesis and characterization of CN-modified protein analogues as potential vibrational contrast agents," *Bioorg. Chem.* **35**, 284–293 (2007).

[67] H. Yamakoshi, K. Dodo, M. Okada, J. Ando, A. Palonpon, K. Fujita, S. Kawata, M. Sodeoka, "Imaging of EdU, an alkyne-tagged cell proliferation probe, by Raman microscopy," *JACS* **133**, 6102–6105 (2011).

[68] L. Ujj, Y. Zhou, M. Sheves, M. Ottolenghi, S. Ruhman, G. H. Atkinson, "Vibrational spectrum of a picosecond intermediate in the artificial BR5.12 photoreaction: Picosecond time-resolved CARS of T5.12," *J. Am. Chem. Soc.* **122**, 96–106 (2000).

[69] J. X. Cheng, A. Volkmer, L. D. Book, X. S. Xie, "An epi-detected coherent anti-Stokes Raman scattering (E-CARS) microscope with high spectral resolution and high sensitivity," *J. Phys. Chem. B* **105**, 1277–1280 (2001).

[70] I. C. Chang, "Noncollinear acoustooptic filter with large angular aperture," *Appl. Phys. Lett.* **25**, 370–372 (1974).

[71] I. C. Chang, "Acousto-optic tunable filters," *Opt. Eng.* **20**, 824–829 (1981).

[72] T. Yano, A. Watanabe, "Acoustooptic TeO_2 tunable filter using far-off-axis anisotropic Bragg diffraction," *Appl. Opt.* **15**, 2250–2258 (2076).

[73] S. Wada, K. Akagawa, H. Tashiro, "Electronically tuned Ti:sapphire laser," *Opt. Lett.* **21**, 731–733 (1996).

[74] J. Geng, S. Wada, H. Tashiro, "A widely tunable picosecond Ti:sapphire laser without any mechanical action," *CLEO 2000*, 486–487 (2000).

[75] S. Wada, J. Geng, N. Saito, and H. Tashiro, "Electronically tuned picosecond Ti:sapphire laser," RIKEN Review **49**, 7 (2002).

[76] H. Nagaoka, T. Miura, F. Kannari, K. Takasago, K. Torizuka, M. Washio, "Precisely synchronized two mode-locked lasers with optical phase-locked loop," *ASSL 2001*, 429–434 (2001).

[77] R. K. Shelton, L. S. Ma, H. C. Kapteyn, M. M. Murnane, J. L. Hall, J. Yee, "Active synchronization and carrier phase locking of two separate mode-locked femtosecond lasers," *J. Mod. Opt.* **49**, 401–409 (2002).

[78] T. Minamikawa, N. Tanimoto, M. Hashimoto, T. Araki, M. Kobayashi, K. Fujita, S. Kawata, "Jitter reduction of two synchronized picosecond mode-locked lasers using balanced-cross correlator with two-photon detectors," *Appl. Phys. Lett.* **89**, 191101-1–3 (2006).

[79] Z. Sun, J. Gong, H. Wu, W. Xu, L. Wu, D. Xu, J. Gao, J. W. Wu, H. Yang, M. Yang, P. Li, "Perilipin1 promotes unilocular lipid droplet formation through the activation of Fsp27 in adipocytes," *Nature Comm.* **4**, 1594-1–14 (2013).

[80] R. Somwar, C. T. Roberts, Jr., O. Varlamov, "Live-cell imaging demonstrates rapid cargo exchange between lipid droplets in adipocytes," *FEBS Lett.* **585**, 1946–1950 (2011).

[81] L. Kuerschner, C. Moessinger, C. Thiele, "Imaging of lipid biosynthesis: How a neutral lipid enters lipid droplets," *Traffic* **9**, 338–352 (2008).

[82] C. D. L. Folmes, D. Sowah, A. S. Clanachan, G. D. Lopaschuk, "High rates of residual fatty acid oxidation during mild ischemia decrease cardiac work and efficiency," *J. Mol. Cell. Cardiol.* **47**, 142–148 (2009).

[83] T. R. Koves, J. R. Ussher, R. C. Noland, D. Slentz, M. Mosedale, O. Ilkayeva, J. Bain, R. Stevens, J. R. B. Dyck, C. B. Newgard, G. D. Lopaschuk, D. M. Muoio, "Mitochondrial overload and incomplete fatty acid oxidation contribute to skeletal muscle insulin resistance," *Cell Metab.* **7**, 45–56 (2008).

[84] A. Schönle, S. W. Hell, "Heating by absorption in the focus of an objective lens," *Opt. Lett.* **23**, 325–327 (1998).

[85] K. Konig, T. W. Becker, P. Fisher, I. Riemann, K. J. Halbhuber, "Pulse-length dependence of cellular response to intense near-infrared laser pulses in multiphoton microscopes," *Opt. Lett.* **24**, 113–115 (1999).

[86] Y. Fu, H. Wang, R. Shi, J. X. Cheng, "Characterization of photodamage in coherent anti-Stokes Raman scattering microscopy," *Opt. Expr.* **14**, 3942–3951 (2006).

[87] J. Bewersdorf, R. Pick, and S. W. Hell, "Multifocal multiphoton microscopy," *Opt. Lett.* **23**, 655–657 (1998).

[88] M. Kobayashi, K. Fujita, T. Kaneko, T. Takamatsu, O. Nakamura, and S. Kawata, "Second-harmonic-generation microscope with a microlens array scanner," *Opt. Lett.* **27**, 1324–1326 (2005).

[89] T. Minamikawa, M. Hashimoto, K. Fujita, S. Kawata, T. Araki "Multi-focus excitation coherent anti-Stokes Raman scattering (CARS) microscopy and its applications for realtime imaging," *Opt. Exp.* **17**, 9526–9536 (2009).

[90] M. Okuno, H. Hamaguchi, "Multifocus confocal Raman microspectroscopy for fast multimode vibrational imaging of living cells," *Opt. Lett.* **35**, 4096–4098 (2010).

[91] M. Hashimoto, T. Asada, T. Araki, Y. Inouye, S. Kawata, "Automatic pulse duration control of picosecond laser using two-photon absorption detector," *Jpn. J. Appl. Phys.* **44**, 3958–3961 (2005).

[92] S. W. Chu, T. M. Liu, C. K. Sun, C. Y. Lin, H. J. Tsai, "Real-time second-harmonic-generation microscopy based on a 2-GHz repetition rate Ti:sapphire laser," *Opt. Expr.* **11**, 933–938 (2003).

[93] N. Ji, J. C. Magee, E. Betzig, "High-speed, low-photodamage nonlinear imaging using passive pulse splitters," *Nat. Method* **5**, 197–202 (2008).

[94] E. O. Potma, X. S. Xie, "Direct visualization of lipid phase segregation in single lipid bilayers with coherent anti-Stokes Raman scattering microscopy," *Chem. Phys. Chem.* **6**, 77–79 (2005).

[95] L. Li, H. Wang, J. X. Cheng, "Quantitative coherent anti-Stokes Raman scattering imaging of lipid distribution in coexisting domains," *Biophys. J.* **89**, 3480–3490 (2005).

[96] B. Levine, C. V. Shank, J. P. Heritage, "Surface vibrational spectroscopy using stimulated Raman scattering," *IEEE J. Quantum Electron* **15**, 1418–1432 (1979).

[97] J. Ye, L. S. Ma, J. L. Hall, "Ultrasensitive detections in atomic and molecular physics: Demonstration in molecular overtone spectroscopy," *J. Opt. Soc. Am. B* **15**, 6–15 (1998).

[98] D. Fu, T. Ye, T. E. Matthews, B. J. Chen, G. Yurtsever, W. S. Warren, " High-resolution *in vivo* imaging of blood vessels without labeling," *Opt. Lett.* **32**, 2641–2643 (2007).

[99] G. Marriott, S. Mao, T. Sakata, J. Ran, D. K. Jackson, C. Petchprayoon, T. J. Gomez, E. Warp, O. Tulyathan, H. L. Aaron, E. Y. Isacoff, Y. Yan, "Optical lock-in detection imaging microscopy for contrast-enhanced imaging in living cells," *PNAS* **105**, 17789–17794 (2008).

[100] K. G. Libbrecht, E. D. Black, C. M. Hirata, "A basic lock-in amplifier experiment for the undergraduate laboratory," *Am. J. Phys.* **71**, 1208–1213 (2008).

[101] R. Wolfson, "The lock-in amplifier: A student experiment," *Am. J. Phys.* **59**, 569–572 (1991).

[102] D. Voet, J. G. Voet, C. W. Pratt, *Principles of biochemistry* (J. Wiley & Sons, Inc., SINGAPORE, 2013).

[103] X. S. Xie, J. Yu, W. Y. Yang, "Living cells as test tubes," *Science.* **312.** 228–230 (2006).

[104] N. Krahmer, Y. Guo, R. V. Farese, T. C. Walther, "SnapShots: Lipid droplets," *Cell.* **139.** 1024–1024.e1 (2009).

[105] K. Simons, E. Ikonen, "Functional rafts in cell membranes" *Nature*, **387**, 569 (1997).

[106] N. Abumrad, C. Harmon, A. Ibrahimi, "Membrane transport of long-chain fatty acids: evidence for a facilitated process", *J. Lipid Res.*, **39**, 2309 (1998).

[107] D. J. Murphy, J. Vance, "Mechanism of lipid-body formation," *Trends Biochem. Sci.* 24, 109–115 (1999).

[108] D. J. Murphy, "The biogenesis and functions of lipid bodies in animals, plants, and microorganisms," *Progrs Lipid Res.* **40**, 325–438 (2001).

[109] T. M. Lewin, R. A. Coleman, "Regulation of myocardial triacylglycerol synthesis and metabolism," *BBA* **1634**, 63–75 (2003).

[110] M. J. McArthur, B. P. Atshaves, A. Frolov, W. D. Foxworth, A. B. Kier, F. Schroeder, "Cellular uptake and intracellular trafficking of long chain fatty acids," *J. Lipid Res.* **40**, 1371–1383 (1999).

[111] J. Fischer, C. Lefevre, E. Morava, J. M. Mussini, P. Laforet, A. N. Salvayre, M. Lathrop, R. Salvayre, "The gene encoding adipose triglyceride lipase (PNPLA2) is mutated in neutral lipid storage disease with myopathy," *Nat. Gen.* **39**, 28–30 (2007).

[112] N. Hilaire, R. Salvayre, J. C. Thiers, M. J. Bonnafé, A. N. Salvayre, "The turnover of cytoplasmic triacylglycerols in human fibroblasts involves two separate acyl chain length-dependent degradation pathways," *Biochem. J.* **270**, 27027–27034 (1995).

[113] K. Hirano, "A novel clinical entity：triglyceride deposit cardiomyovasculopathy," *J. Atheroscler. Thromb*. **16**, 702–705 (2009).

[114] K. Hirano, Y. Ikeda, N. Zaime, Y. Sakata, G. Matsumiya, "Triglyceride deposit cardiomyovasculopathy," *N. Engl. J. Med.* **352**, 2396–2398 (2008).

[115] W. Guo, J. K. Choi, J. L. Kirkland, B. E. Corkey, J. A. Hamilton, "Esterification of free fatty acids in adipocytes: a comparison between octanoate and oleate, " *Biochem. J.* **349**, 463–471 (2000).

[116] F. Labarthe, R. Gélinas, C. D. Rosiers, "Medium-chain fatty acids as metabolic therapy in cardiac disease," *Cardiovasc. Drugs Ther.* **22**, 97–106 (2008).

[117] A. A. Papamandjaris, D. E. MacDougall, P. J. H. Jones, "Medium chain fatty acid metabolism and energy expenditure: obesity treatment implications," *Life Sci.* **62**, 1203–1215 (1998).

[118] K. Nagao, T. Yanagita, "Medium-chain fatty acids: functional lipids for the prevention and treatment of the metabolic syndrome," *Pharm. Res.* **61**, 208–212 (2010).

[119] C. A. Souders, S. L. K. Bowers, T. A. Baudino, "Cardiac fibroblast: the renaissance cell", *Circ. Res. JAHA* **105**, 1164–1176 (2009).

List of publications

Original paper:

[1] Harsono Cahyadi, Junichi Iwatsuka, Takeo Minamikawa, Hirohiko Niioka, Tsutomu Araki, Mamoru Hashimoto, "Fast spectral coherent anti-Stokes Raman scattering (CARS) microscopy with high-speed tunable picosecond laser," *Journal of Biomedical Optics*, in press, (accepted on August 7, 2013).

International conference:

[1] Harsono Cahyadi, Hirohiko Niioka, Tsutomu Araki, Mamoru Hashimoto, "Monitoring of CPT-11 in living cells with CARS microscopy and fluorescence microscopy," *6th Photonics Center Symposium*, Japan (2011).

[2] Harsono Cahyadi, Junichi Iwatsuka, Takeo Minamikawa, Hirohiko Niioka, Tsutomu Araki, Mamoru Hashimoto, "Fast spectral imaging CARS microscopy with picosecond high-speed wavelength scanning laser," *Focus on Microscopy 2012*, Singapore (2012).

[3] Harsono Cahyadi, Junichi Iwatsuka, Takeo Minamikawa, Hirohiko Niioka, Tsutomu Araki, Mamoru Hashimoto, "Fast spectral CARS microscopy with high-speed tunable picosecond laser for detection of lipid metabolism," *International Congress of Histochemistry and Cytochemistry 2012*, Japan (2012).

[4] Harsono Cahyadi, Hirohiko Niioka, Ken-ichi Hirano, Chiaki Ikegami-Nomura, Tsutomu Araki, Mamoru Hashimoto, "Detection of Lipid Uptake by Triglyceride Deposit Cardiomyovasculopathy- (TGCV-) Fibroblast Using CARS Microscopy,"

Joint Symposium JSAP-OSA, Annual Autumn Meeting of Japan Society of Applied Physics, Japan (2012).

[5] Harsono Cahyadi, Hirohiko Niioka, Tsutomu Araki, Mamoru Hashimoto, "Detection of intracellular lipid accumulation using fast spectral CARS imaging," *7th Photonics Center Symposium*, Japan (2012).

[6] Harsono Cahyadi, Hirohiko Niioka, Chiaki Ikegami-Nomura, Ken-ichi Hirano, Tsutomu Araki, Mamoru Hashimoto, "Detection of medium- and long-chain fatty acids accumulation by triglyceride deposit cardiomyovasculopathy-indicated fibroblasts using fast spectral coherent anti-Stokes Raman scattering microscopy," *2nd International Symposium on TGCV and NLSD*, Japan (2013).

[7] Harsono Cahyadi, Hirohiko Niioka, Tsutomu Araki, Mamoru Hashimoto, "Spectral Stimulated Raman Scattering Microscopy with High-Speed Wavelength Scanning Laser for Detection of Cellular Lipid Uptake," *7th International Conference on Advanced Vibrational Spectroscopy*, Japan (2013)

Domestic conference:

[1] Harsono Cahyadi, Kouhei Ikeda, Hirohiko Niioka, Tsutomu Araki, Mamoru Hashimoto, "Imaging of CPT-11 in living cells with CARS microscopy and fluorescence microscopy," *Optical and Photonics Japan*, Osaka (2011).

[2] Kouhei Ikeda, Harsono Cahyadi, Hirohiko Niioka, Tsutomu Araki, Mamoru Hashimoto, "Intracellular imaging of anticancer drug using CARS microscopy," *Annual Meeting of Bioengineering Conference of the Japan Society of Mechanical Engineering 2012*, Osaka (2012).

[3] Harsono Cahyadi, Hirohiko Niioka, Ken-ichi Hirano, Chiaki Ikegami-Nomura, Tsutomu Araki, Mamoru Hashimoto, "Fast spectral coherent anti-stokes Raman

scattering microscopy for detection of lipid accumulation in triglyceride deposit cardiomyovasculopathy-indicated fibroblasts," *Annual Meeting of the Spectroscopical Society of Japan 2012*, Matsuyama (2012)

[4] Harsono Cahyadi, Naokazu Matsumura, Hirohiko Niioka, Tsutomu Araki, Mamoru Hashimoto, "Stimulated Raman Scattering Microscopy with High-Speed Wavelength Scanning Laser," *Annual Spring Meeting of Japan Society of Applied Physics 2013*, Kanagawa (2013).

Award:

[1] Best Poster Presentation (September 2012)

Harsono Cahyadi, Hirohiko Niioka, Tsutomu Araki, Mamoru Hashimoto, Detection of intracellular lipid accumulation using fast spectral CARS imaging," *7th Photonics Center Symposium*, Japan (2012).

Photonics Advanced Research Centre (PARC), Osaka University